



**UNIVERSITY OF CAPE TOWN**  
IYUNIVESITHI YASEKAPA • UNIVERSITEIT VAN KAAPSTAD

DEPARTMENT OF CIVIL ENGINEERING  
COMPUTATIONAL CONTINUUM MECHANICS GROUP

---

# **An efficient three-dimensional database driven approach for multi scale homogenization**

---

A DISSERTATION SUBMITTED IN PARTIAL FULFILMENT OF  
THE REQUIREMENTS FOR A MASTER OF SCIENCES DEGREE IN  
THE FIELD OF CIVIL ENGINEERING

**PREPARED FOR: UNIVERSITY OF CAPE TOWN**

*Author:*

Mr Nicholas JARRATT

*Supervisor:*

A/Prof Sebastian SKATULLA

*This research has been supported by the National Research Foundation of South Africa (Grant Numbers 104839 and 105858). Opinions expressed and conclusions arrived at, are those of the author and are not necessarily to be attributed to the NRF.*

October 14, 2019

# Declaration

I, Nicholas Jarratt, declare that this thesis titled, "An efficient three-dimensional database driven approach for multi scale homogenization." and all the work contained herein, save for that which is properly acknowledged, is my own. I confirm that:

- I know that plagiarism is wrong. Plagiarism is to use another's work and to pretend that it is one's own.
- Each significant contribution to and quotation in this document from the work or works of other people has been attributed and has been cited and referenced
- This essay/report/project is my own work.
- I have not allowed and will not allow anyone to copy this work with the intention of passing it as their own.
- This thesis/dissertation has been submitted to the Turnitin module (or equivalent similarity and originality checking software) and I confirm that my supervisor has seen my report and any concerns revealed by such have been resolved with my supervisor.

Name: Nicholas Jarratt

Signature:  \_\_\_\_\_

Student No: JRRNIC001

Date: October 14, 2019

# Abstract

The two-scale homogenization theory, commonly known as the  $FE^2$  method, is a well-established technique used to model structures made of heterogeneous materials. Capable of capturing the microscopic effects at the macro level, the  $FE^2$  method assigns a representative volume element (RVE) of the materials microstructure at points across the macroscopic sample. This process results in the realization of a fully nested boundary value problem, where macroscopic quantities, required to model the structure, are obtained by homogenizing the RVEs response to macroscopic deformations. A limitation of the  $FE^2$  method though is the high computational costs, whereby its reduction has been a topic of much research in recent years.

In this research, a two-scale database (TSD) model is presented to address this limitation. Instead of homogenizing the RVEs response to macroscopic deformations, the macroscopic quantities are now approximated using a database of precomputed RVEs. The homogenized results of an RVE are stored in a macroscopic right *Cauchy-Green* strain space. Discretizing this strain space into a finite set of right *Cauchy-Green* deformation tensors yields a *material database*, where the components of each tensor represent the boundary conditions prescribed to the RVE. A continuous approximation of the macroscopic quantities is attained using the *Moving Least Squares* (MLS) approximation method.

Subsequent attention is paid to the implementation of the  $FE^2$  method and TSD model, for solving structures made of hyperelastic heterogeneous materials. Both approaches are developed in the in-house simulation software SESKA. A qualitative comparison of results from the  $FE^2$  method to those previously published, for a laminated composite beam undergoing material degradation, is presented to verify its implementation. To assess the TSD models performance, an evaluation into the numerical accuracy and computational performance, against the conventional  $FE^2$  method, is undertaken. While a significant improvement on computational times was shown, the accuracies in the TSD model were still left to be desired. Various remedies to improve the accuracy of the TSD model are proposed.

# Acknowledgements

I would first like to thank my supervisor, A/Prof Sebastian Skatulla; for his guidance and support throughout my masters, for his patience and taking the time to assist me with theoretical and programming issues, and for giving me such an interesting topic.

To Dr. Ritesh Rama, for his time, patience, willingness to always help and assistance with some really tricky software issues.

To the research group, particularly Devin and Emmanuel; for your friendship, insightful discussions, banter, and being there in times of need.

Finally to my friends and family, particularly my mother; for all their support and encouragement throughout this masters, I love you all.

This research has been supported by the National Research Foundation of South Africa (Grant Numbers 104839 and 105858). Opinions expressed and conclusions arrived at, are those of the author and are not necessarily to be attributed to the NRF.



# Contents

<b>List of Figures</b>	<b>v</b>
<b>List of Tables</b>	<b>vii</b>
<b>1 Introduction</b>	<b>1</b>
1.1 Background . . . . .	1
1.2 Multi scale homogenization . . . . .	4
1.3 Model reduction techniques associated with multi scale homogenization . . . .	5
1.4 Thesis motivation, aims and objectives . . . . .	6
1.5 Scope and limitations . . . . .	7
1.6 Thesis layout . . . . .	8
<b>2 Micro-macro continuum mechanics</b>	<b>9</b>
2.1 Macro continuum . . . . .	11
2.1.1 Kinematics . . . . .	11
2.1.2 Stress . . . . .	13
2.1.3 Balance of linear momentum . . . . .	14
2.1.4 Variational formulation . . . . .	15
2.2 Micro continuum . . . . .	18
2.2.1 Kinematics, stress and balance equations . . . . .	18
2.2.2 Variational formulation . . . . .	20
2.3 Coupling the macro and micro continuum . . . . .	21
2.3.1 Kinematics . . . . .	21
2.3.2 Stress . . . . .	23
2.3.3 Macro-homogeneity condition . . . . .	25
2.3.4 Tangent operator . . . . .	26
2.4 Representative Volume Element . . . . .	27
<b>3 FE<sup>2</sup> implementation</b>	<b>31</b>
3.1 Microscopic boundary value problem . . . . .	31
3.2 Computation of macroscopic tangent operator . . . . .	33
3.3 Algorithmic treatment . . . . .	35
3.4 Computational Example . . . . .	38
3.4.1 Convergence analysis of undamaged case . . . . .	39
3.4.2 Global damaged case . . . . .	41
3.4.3 Local damaged case . . . . .	41

<b>4</b>	<b>Two-scale database model</b>	<b>44</b>
4.1	Introduction . . . . .	44
4.2	Computational details . . . . .	47
4.3	Macroscopic strain domain and its discretization . . . . .	47
4.4	Approximation of macroscopic variables . . . . .	49
4.4.1	Moving Least Squares Approximation . . . . .	50
4.5	Implementation and algorithmic treatment . . . . .	53
<b>5</b>	<b>Numerical Analysis</b>	<b>56</b>
5.1	Micro model description . . . . .	56
5.2	Microstructural analysis . . . . .	57
5.3	Evaluation of the TSD model . . . . .	60
5.3.1	Material database description and MLS approximation details . . . . .	61
5.3.2	Macroscopic stress . . . . .	62
5.3.3	Macroscopic tangent operator . . . . .	66
5.3.4	Computational time . . . . .	70
<b>6</b>	<b>Computational example</b>	<b>72</b>
6.1	Macroscopic problem description . . . . .	72
6.2	Load Case 1: Tension . . . . .	74
6.3	Load Case 2: Compression . . . . .	76
6.4	Load Case 3: Bending . . . . .	78
<b>7</b>	<b>Summary, concluding remarks and future work</b>	<b>82</b>
7.1	The $FE^2$ method . . . . .	82
7.2	The two-scale database model . . . . .	83
7.3	Future work . . . . .	85
	<b>Appendices</b>	<b>87</b>
<b>A</b>	<b>Prescribing periodic boundary conditions on the microscopic boundary value problem</b>	<b>87</b>
<b>B</b>	<b>Ethics Approval</b>	<b>90</b>

# List of Figures

1.1	Representation of a macroscopic sample with a globally periodic microstructure	2
2.1	Schematic representation of the two-scale homogenization scheme, taken from Schröder [90]	10
2.2	Splitting arrangement of the RVE prior to solving the <i>periodic boundary displacement</i> model (left) and the deformed result after (right).	20
2.3	Proper identification of an RVE, in a periodic material, taken from Gitman et al. [26]	28
2.4	Dependency of the apparent properties of an RVE, with respect to both size and chosen boundary condition (taken from Kouznetsova et al. [48]).	29
3.1	Incrementally-iterative solution scheme for the $FE^2$ method.	37
3.2	Geometry of the beam considered and its microstructure.	38
3.3	Discretized beam and RVE analyzed for the undamaged case	39
3.4	Convergence of the beams reaction force with discretizations at the macro scale	40
3.5	Beams reaction force for the global damage case, showing the results to be in good agreement.	41
3.6	RVEs for the local damage case	42
3.7	Beams reaction force to the percentage of lamina 2 layers damaged	42
3.8	The response from the different RVEs (12.5%, 25%, 50% damage, from left to right) to the same strain showing the highest deformations occurring in the damaged layer.	43
4.1	Illustrations of the two-dimensional strain space, made up of components $\bar{C}_{ij}$ for a two-dimensional problem.	45
4.2	Approximation of $\bar{S}_{11}(\bar{C})$ from the stored values $\bar{S}_{11}^I(\bar{C})$ in the $\bar{C}_{11} - \bar{C}_{22}$ plane.	46
4.3	Evaluation of the approximated 1D polynomial function using the MLS method	52
4.4	Evaluation of the approximated 2D polynomial function using the MLS method	52
4.5	Zone of influence in the subdomain $\Delta_i$ , for the macroscopic strain component $\bar{C}_i$ , showing the set of supporting particles.	54
4.6	Algorithm for the TSD model model	55
5.1	Chosen RVE and its material parameters	57
5.2	Microscopic <i>Green strain</i> contour plots for the macroscopic normal strains, $\bar{C}_{11}$ and $\bar{C}_{22}$ , showing a uniform and non-uniform distribution of $E_{11}$ and $E_{22}$ , respectively.	58
5.3	Simple analogy of the directional stiffness given by the laminated composite.	58

5.4	Contour plots of shear <i>Green strain</i> values, $E_{12}$ (left) and $E_{31}$ (right), for the macroscopic normal strains, $\bar{C}_{12}$ and $\bar{C}_{31}$ , respectively. . . . .	59
5.5	Microscopic second <i>Piola-Kirchhoff</i> stress contour plots for the various $\bar{C}$ strains. . . . .	60
5.6	Comparison of the TSD and $FE^2$ solutions, for variations in $\bar{C}_{ij}$ . . . . .	62
5.7	Absolute difference between the TSD and $FE^2$ solutions, which are denoted as $\hat{S}_{ij}$ and $\bar{S}_{ij}$ , respectively, along with the $FE^2$ solutions shown for variations in $\bar{C}_{ij}$ . . . . .	63
5.8	Relative error distribution of the macroscopic stress components $\bar{S}_{11}$ and $\bar{S}_{22}$ of the TSD model, plotted against the solutions of the $FE^2$ method, for the set of macroscopic strain states, as indicated. . . . .	65
5.9	Relative error distribution of the macroscopic stress components $\bar{S}_{12}$ and $\bar{S}_{31}$ of the TSD model, plotted against the solutions of the $FE^2$ method, for the set of macroscopic strain states, as indicated. . . . .	67
5.10	Relative error distribution of the macroscopic tangent operator components $\bar{H}_{1212}$ and $\bar{H}_{3131}$ of the TSD model, plotted against the solutions of the $FE^2$ method, for the set of macroscopic strain states, as indicated. . . . .	68
5.11	Relative error distribution of the macroscopic tangent operator components $\bar{H}_{1212}$ and $\bar{H}_{3131}$ of the TSD model, plotted against the solutions of the $FE^2$ method, for the set of macroscopic strain states, as indicated. . . . .	69
5.12	Computational times of the TSD model and $FE^2$ method, for the set of 200 macroscopic strain states. . . . .	71
6.1	Macroscopic boundary value problem example . . . . .	73
6.2	Response to tension . . . . .	75
6.3	Convergence results of a typical Newton iteration, for the tensile loading case, with $\log_{10}$ scaling and a cut-off convergence norm of $1 \times 10^{-8}$ . . . . .	75
6.4	Response to compression . . . . .	76
6.5	Contour plot of the normal macroscopic stresses $\bar{S}_{11}$ and $\bar{S}_{22}$ , for the compressive loading case, respectively. . . . .	77
6.6	Convergence results of a typical Newton iteration, for the compressive loading case, with $\log_{10}$ scaling and a cut-off convergence norm of $1 \times 10^{-8}$ . . . . .	78
6.7	Response to bending . . . . .	78
6.8	Evolution of the stress and strain at beam points for the bending loading case, with the values monitored at two points of each beam as shown, respectively. . . . .	80
6.9	Convergence results of a typical Newton iteration, for the bending loading case, with $\log_{10}$ scaling and a cut-off convergence norm of $1 \times 10^{-8}$ . . . . .	81
A.1	3-D schematic representation of the periodic boundary condition . . . . .	87

# List of Tables

2.1	Macroscopic gradient and divergence operators for reference and current configuration. . . . .	11
2.2	Microscopic gradient and divergence operators for reference and current configuration. . . . .	19
3.1	Mechanical properties of the three materials . . . . .	38
3.2	Discretization refinements considered at the macro scale. . . . .	40
3.3	Shear modulus for the stages of material degradation . . . . .	41
5.1	Particles of the discretized macroscopic strain space. . . . .	61
5.2	$L_2$ -norm relative error values of the approximated $\bar{\mathbf{S}}$ components. . . . .	64
5.3	$L_2$ -norm relative error values of the approximated $\bar{\mathbf{H}}$ components. . . . .	66
6.1	Beam loading cases . . . . .	74
6.2	$L_2$ -norm relative error for the tensile loading case . . . . .	74
6.3	$L_2$ -norm relative error for the compressive loading case . . . . .	76
6.4	$L_2$ -norm relative error for the tensile loading case . . . . .	79

# Chapter 1

## Introduction

### 1.1 Background

A composite material is generally taken to be a material consisting of two or more constituents or phases [96]. These heterogeneities can include voids, fibers and stiff or soft inclusions and can vary in size. Any material, human-made or natural, can thus be considered heterogeneous at a particular scale. The ongoing improvement of technology over the past century has led to the rapid development of heterogeneous materials, and the need to understand the interactions between these heterogeneities. In the past, experimental test methods would be conducted on a series of material samples to determine its "effective properties" [41]. This approach has become less appealing in recent times though due to the number of resources required, such as time and money.

Conversely, to accurately model the microstructure at the macroscopic level, each constituent in the heterogeneous structure would need to be modeled explicitly. While a hypothesis on the microstructural behavior at the macro scale is not required in this case, the method is often impractical due to the enormous difference in length scales between the heterogeneities and the macroscopic sample. Moulinec and Suquet [69] used Fast Fourier Transforms, with images of the microstructure, to reduce the size of the meshing, but still required computers with high memory capabilities. The application of *micro modeling* is thus limited to localized phenomena cases, where analysis of the microstructure is required. These include contact problems [27, 112], microstructural damage [73] and micro-cracking [40]. A parameter fitting technique was implemented by Geers [20] and Meuwissen [62] to obtain the effective property of a material's microstructure. By fitting material parameters to experimental data, one can obtain the macroscopic strain-energy function of the material. Though successful, this approach is tedious and, despite being optimized by Gendy and Saleeb [22] and Ogden et al. [72], requires large volumes of experimental data.

An alternative method to obtain the effective properties is *homogenization*. This technique replaces the complex microstructure with one that is statistically homogeneous at the macroscopic level. The replacement of the complex microstructure with one that is homogeneous overcomes the need for complex meshing. Also, depending on the chosen homogenization theory, the mechanical response can be investigated with no prior knowledge of the material, giving a first approximation on the stress distribution at the micro level. These

characteristics surpass the limitations posed by the other methods, making it the preferred choice when modeling composites. There are several different homogenization approaches, of which the most common are briefly discussed below. For a more comprehensive review, we refer the reader to Nemat-Nasser and Hori [71].

The most straightforward homogenization approach is the rule of mixtures. This approach computes the effective property by averaging the property of each constituent, which is weighted by its volume fraction, across the macroscopic sample [29]. Only one microstructural characteristic is captured though, the volume fractions. Another drawback is the constituent properties being limited to linear material properties, such as the elastic modulus and Poisson's ratio.

A more sophisticated approach is the self-consistent estimates, which includes several variations for computing the overall properties of heterogeneous materials. Estimates of the relevant properties, which fall within a particular set of bounds, are computed from solutions to a boundary value problem with a spherical or ellipsoidal particle in a matrix material. The method is based on the works of Hill [35], Budianski [6], Kröner [50] and Hashin and Shtrikman [31] and makes use of the theory first established by Eshelby [16]. This approach was further developed by Willis [114] and Hashin [30] and more recently by Berryman [4]. Apart from being limited to cases involving linear elastic responses, the approach fails to describe the behavior of clustered and complex microstructures [47]. Additionally, issues in accuracy and computational costs were also reported for linear viscoelastic problems in Tran et al. [109].

Asymptotic homogenization is a more rigorous mathematical approach based on perturbation theory. Proposed and developed by Bensoussan et al. [3] and Sanchez-Palencia [87], the method is formulated in terms of asymptotic expansion theory and makes use of the separation of scales principle. The effective properties are calculated by solving partial differential equations defined on a unit cell. This unit cell is a characteristic volume, isolated from the macrostructure and repeated throughout the bulk of the material. Schematically represented in Figure 1.1, the assumption that the macroscopic sample consists of spatially repeated unit cells is referred to as *global periodicity* [46]. For a more comprehensive review of the various asymptotic homogenization procedures, we refer to Kalamkarov et al. [43].

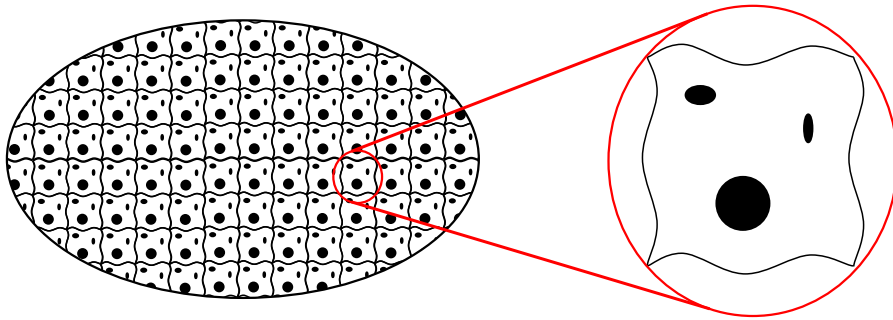


Figure 1.1: Representation of a macroscopic sample with a globally periodic microstructure: the unit cell, shown on the right, is the characteristic volume containing enough information to determine the effective properties at the macro scale [46].

One advantage of asymptotic homogenization is that it allows the local stress and strain

distributions to be determined with high accuracy. Cai et al. [7] recently showed the approach to be useful in solving plate and shell structures. Lee and Yu [55], on the other hand, reported this application to be difficult to implement numerically. Assumptions, having to be made on the properties of the composite as a whole, means that the approach is limited to very simple micro geometries and simple material models at small strains [47]. Furthermore, these assumptions can cause difficulty when modeling damage and cracking [43]. In cases where the actual periodicity of the microstructure is lost, a strong accuracy reduction could also be expected. This can be addressed through statistical asymptotic homogenization methods, proposed by Zhao et al. [119], which assigns randomness to the spatial distribution of particles in unit cells, but is still limited to acquiring effective elastic properties at the macro scale. Finally, this method is also shown to have difficulties when dealing with boundary regions, which then requires special attention [43].

Another homogenization approach is one that devises constitutive equations for models at the macro level. Similar to asymptotic homogenization, these unit cell methods exploit the periodicity concept, where a characteristic volume can be isolated from the composite material and repeated across the macrostructure. This characteristic volume is referred to as a *Representative Volume Element* (RVE) and can statistically represent any point in the composite. Originally introduced by Hill [34], the RVE is different to a unit cell in that it is not limited to simple micro geometries or material models. The ability to account for complex microstructural morphologies allows for the analysis of different geometrical features at the micro level and their effects at the macro level. The assumption that the RVE can represent any macroscopic point, which Hashin [30] refers to as *statistical homogeneity*, allows a closed form macroscopic phenomenological equation to be developed through either analytical or numerical means.

We refer to the works of Castañeda [8], Găărăjeu [19] and Nemat-Nasser and Hori [71] in the case of deriving constitutive equations from analytical means. For numerical means, which follows the work of Vosbeek [113], we refer to Van der Sluis et al. [93], Smit et al. [94], and Van der Sluis et al. [111]. De Botten et al. [13] more recently used this approach to compute the strain-energy density function for a transversely isotropic neo-Hookean composite. Unit cell methods are only successful for small deformations though, as large deformations tend to lead to inadequate results [47]. Another drawback is one similar to asymptotic homogenization, in that the assignment of one RVE to every macroscopic point restricts this approach to materials having a periodic microstructure. This inherently limits the scope of the model as certain assumptions, simplifying the behavior of the microstructure, have to be made to derive expressions for the overall behavior. Van der Sluis et al. [110] made improvements in this respect, but still left accuracies from the model to be desired.

An alternative method is one that makes use of the RVE, but instead of producing a constitutive relation, describing the bulk of the material, an estimate for the stress-strain relationship is computed for each macroscopic point. This stress-strain relationship is estimated by analyzing the solution of a boundary value problem at the micro scale, using finite element methods. The method is referred to as *multi scale homogenization*, or the *FE<sup>2</sup> method*, and is a fully nested scheme that solves two boundary value problems at different scales.



## 1.2 Multi scale homogenization

The fully nested framework incorporates two boundary value problems, one at the micro scale and the other at the macro scale. The foundation for the approach was introduced by Suquet [98] and presented by Guedes and Kikuchi [28], Terada and Kikuchi [105] and Gosh et al. [23, 24]. The approach was then further developed, into what is referred to as multi scale homogenization or the  $FE^2$  method, by Smit et al. [95], Michel et al. [63], Miehe et al. [67, 66], Feyel and Chaboche [17], Terada and Kikuchi [106]; Ghosh et al. [25]; Kouznetsova et al. [47]; Miehe and Koch [65]. A volume element, representing the microstructure of the heterogeneous material, is attached to points across the macroscopic sample. This RVE is used to create a boundary value problem at the micro scale, which is solved using finite element methods. Once solved the results are analyzed, and an estimate for the stress-strain relationship at the macroscopic point generated. This procedure is then repeated for all points across the macrostructure. These estimates, associated with their respective macroscopic points, creates the boundary value problem at the macro scale, which is also solved using finite element methods. To bridge the gap between the micro and macro scales, these multi scale methods utilize the ideas of asymptotic homogenization theory, in which we refer to Terada and Kikuchi [105] and Gosh [23], or volume averaging [36, 97].

The volume averaging approach, which conceptually follows the work of Hill [36] and is elaborated in Smit et al. [95], is considered more straightforward, but still accounts for the geometric non-linearities at the macro scale and the material non-linearities at the micro scale. Each integration point in the macroscopic mesh is assigned an RVE. The deformation tensor, associated with the macroscopic integration point, is then used to define suitable boundary conditions to be imposed on the RVE. Following the solution to the micro boundary value problem, the stress field is averaged across the volume of the RVE to give an approximation for the stress tensor at the macro scale. Furthermore, the macroscopic tangent operator can be realized by averaging the microstructural response of the RVE to the imposed macroscopic deformation.

The solving of boundary value problems at two different scales has numerous benefits:

1. large deformations and rotations can be accounted for at both scales;
2. the discretization type (finite elements and meshless, for example) for each scale can differ;
3. physical non-linearities and time-dependent effects can be used in microscopic simulations; while
4. changes to the microstructure can be analyzed at the macro level.

For the type of material behaviors analyzed, we refer to Miehe et al. [67], who determines the overall moduli of polycrystalline materials for non-linear elasto-plastic behavior at large strains, and Féyél and Chaboche [17], who describes the elasto-viscoplasticity of fiber-reinforced composites. An analysis of different RVE configurations for porous materials was conducted by Kouznetsova et al. [47] and illustrates its influence at the macro scale. The  $FE^2$  method has also proven to be valuable in modeling biomaterials, with Breuls et al. [5] predicting local cell deformations in engineered tissue constructs. In more recent works, Okada et al. [74] performed a large-scale human heart simulation, with the cardiomyocytes

and heart being the microstructure and macrostructure respectively.

The assumptions and principles associated with the  $FE^2$  method have also allowed for its extension to problems beyond pure mechanical loading. Özdemir et al. [78] extended the multi scale framework to heat conduction problems. This was later coupled with mechanical loading, allowing for the analysis of thermal-mechanical problems [77]. Schröder [89] similarly derived an approach for electro-mechanically coupled problems, which was later implemented by Schröder and Keip [91]. Other cases where the method has been extended is in the analysis of damage, cracking and debonding at the micro level, see Geers et al. [21]. Extensions in this field by Sanchez et al. [86] has led to the development of a *Failure-Oriented Multiscale Formulation* (FOMF) model, which has been further developed by Toro et al. [108] into a more generalized approach.

Despite its popularity, the approach has a high computational demand, as reported by Miranda Guedes [68], Terada and Kikuchi [105] and Lee and Ghosh [56]. This inherently comes as a result of solving boundary value problems at different scales. Furthermore, the computation of a macroscopic tangent operator, which is consistent with the evolution of the stress at a macroscopic point, requires large amounts of memory allocation [102]. These shortcomings can be further amplified when one considers the size and complexity of the RVE as well as the number of discretizations required at both scales to yield an accurate solution. Improvements in computational power over the past two decades has made the approach more accessible; however, the computational cost regarding time still represents a major challenge [76].

### 1.3 Model reduction techniques associated with multi scale homogenization

A vast number of approaches have been undertaken to reduce the computational demand in multi scale homogenization, ranging from reduced order methods and machine learning to response surface models and data-mining. In some cases, these methods have been used on supercomputers, with parallel computing abilities, to improve the computational performance further. A comprehensive list of these methods is reviewed in Matouš et al. [61], with some of these approaches discussed below.

The use of parallel computing for multi scale homogenization problems was first introduced by Feyel and Chaboche [17]. This approach was further used by Okada et al. [74], who used block LU factorization to approximate the Schur-Complement of the microscopic stiffness matrix and improve the computational efficiency for large scale problems. To reduce the number of simulations at the micro scale, Rohan [82] conducted a sensitivity analysis of the coefficients of the homogenized moduli for microscopic displacements and pressures. Other approaches aimed to reduce the computational time at the micro level.

Guedes and Kikuchi [28] introduced an adaptive finite element method to optimize the mesh size on the microdomain and improve the approximation of the homogenized quantities with minimal effort. In cases where the complexities of the RVE are high, the use of statistically similar representative volume elements (SSRVEs) can be adopted to solve these complex micro boundary value problems faster [1]. Reis and Andrade Pires [80] modified and extended the

use of the *Line Search* method and *Arc-Length* procedure to improve the solving of non-linear problems at the micro scale. This adaptive sub-incremental strategy was shown to not only improve the stability of non-linear problems at the micro scale but also reduced the overall computational time. A popular technique for solving problems at the micro level is reduced order models (ROM), which both reduce computing time and memory allocation. Among these are Proper Generalised Decomposition (PGD) [15], Proper Orthogonal Decomposition (POD) [116, 33] and Transformation Field Analysis (TFA), which follows the works of Dvorak [14] and have become popular in recent years [59, 10]. These ROMs, however, are only applicable to specific non-linear applications and have the potential to drift from the correct homogenized result, as is the case for POD and TFA models, respectively [61].

An alternative to reducing the computational time at the micro scale is to decouple the microscopic boundary value problem from the macroscopic one, in an offline step. Referred to by Matouš et al. [61] as *Response Surface Models*, these models look to substitute the solution to the microscopic boundary value problem with an analytical function at the macro scale. Approximations to the macroscopic quantities are then constructed using digital databases, or *discrete material maps*, and interpolation techniques.

Takano et al. [99] characterized a database with non-linear material properties, computed for a series of material strength tests. This approach was later used for knitted fabric composites, where the bi-axial loading increments were taken to be the parameters of the database [100]. Terada and Kikuchi [105] stored the homogenized stress and tangent operator of microstructures exhibiting macroscopic isotropy in a principle strain domain. Similarly, Temizer and Zohdi [104] computed and stored functions of the invariant set of macroscopic strains for a range of tri-axial stretches. These invariant sets were then used with macroscopic strain energy functions for isotropic homogeneous materials and were later extended by Temizer and Wriggers [101, 103] to materials having macroscopic orthotropy. These approaches, however, restrict the analysis to a specific class of materials.

To overcome this restriction, Yvonnet et al. [117] used the components of the right Cauchy-Green strain as the database parameters, in a method referred to as numerically explicit potentials. This technique, which stores the effective strain energy response of the RVE, has since been extended to visco-elastic materials [109] as well as non-linear stochastic homogenization [9]. Yvonnet et al. [118] recently used the method to approximate the effective strain energy for macroscopic strains falling outside of the bounds of the database domain.

More recently Klusemann and Ortiz [45] developed a phase-space simplicial interpolation method to interpolate variables stored in a highly dimensional phase space efficiently.

## 1.4 Thesis motivation, aims and objectives

Various homogenization methods have been proposed over the years to tackle the need for accurately capturing the microstructural effects of composite materials at the macro scale. The  $FE^2$  method has shown to be a popular method and has allowed highly complex materials to be analyzed. Despite its effectiveness, the method has a high computational demand and is considered one of its main drawbacks. Much focus has been placed on reducing the

computational demand associated with the method. Model reduction techniques, such as reduced order models, have proven to reduce the computational demand at the micro scale, but still entails the solution of a microscopic boundary value problem. The use of databases to approximate the macroscopic quantities and circumvent simulations at the micro scale have shown to be more promising in this regard.

The aim of this research is the implementation and assessment of a database driven multi scale model in a three-dimensional setting. A database comprised of homogenized stress and tangent operator values are stored in a macroscopic right *Cauchy-Green* strain space. These values are generated in an off-line step by running conventional FEM simulations on a stand alone RVE. Macroscopic right *Cauchy-Green deformation* tensors are used to prescribe the boundary conditions and are obtained via discretization of the macroscopic strain space. Once the RVE solution is obtained, the results are homogenized and the macroscopic stress and tangent operator values stored. A continuous approximation of these stored values is then attained using suitable interpolation techniques. We shall refer to this approach as the *two-scale Database* (TSD) model and investigate its efficiency by comparing results, from the TSD model, to those from the conventional  $FE^2$  method. The  $FE^2$  method discussed in this research follows the workings of Miehe et al. [66] and Kouznetsova et al. [47]. We implement both, the TSD and  $FE^2$  model, in the in-house simulation software SESKA, a C++ code supporting FEM. To ensure the correct implementation of the  $FE^2$  method, a three-dimensional problem given by Otero et al. [76] is solved. Our objectives in this research are thus as follows:

1. Implementation of the  $FE^2$  framework in SESKA and benchmarking it against an existing example;
2. Implementation of the two-scale Database model in SESKA; and
3. Application of the TSD model via a numerical example and evaluating it against the  $FE^2$  method.

To approximate the stored variables, we use the well-established interpolation technique known as the Moving Least Squares method (MLS), which has been implemented in the in-house software Orion (see Rama et al. [79]). This technique was chosen due to its effectiveness in interpolating quantities in a multi-dimensional setting [52].

## 1.5 Scope and limitations

The scope of this research is the development of the  $FE^2$  framework and TSD model, which are to serve as foundations for future work. Its applications are thus limited to non-linear elasticity and quasi-static problems. The classical *finite element* (FE) discretisation is chosen for both scales, as Liu and Reina [57] recently proved the averaging relations, as well as the macro-homogeneity condition, to be exact under this discretisation. The purpose of this research is to analyse the efficiency between the proposed database model and the  $FE^2$  method. Thus the chosen RVE in this research is assumed to satisfy the requirements about its correct identification and should not be critically analyzed. The importance of correctly identifying a suitable RVE is discussed though. For the sake of simplicity, bifurcations/instabilities at both the micro and macro scale are not considered, with the focus being on problems where no loss of ellipticity occurs.

## 1.6 Thesis layout

The thesis is split into seven chapters.

Chapter 1 gives an overview of multi scale homogenization and the efforts made to reduce its computational demand. Based on the literature presented, a hypothesis is formulated, where the aims and objectives are drawn and the scope and limitations defined.

Chapter 2 delves into the continuum mechanics governing the  $FE^2$  method. Both the macro and micro scales are considered, as well as the coupling of quantities between the two scales. In this coupling, the *Hill-Mandel Principle of Macro-Homogeneity* and the theory of averages are used and are discussed. The chapter is then concluded with a review of the RVE and its existence.

Chapter 3 describes the implementation and algorithmic treatment of the  $FE^2$  method, as well as the computation of the algorithmically consistent tangent operator, which is introduced in Chapter 2. A benchmark problem, involving material degradation at the micro level, is presented to verify its implementation and highlight the computational demands associated with the method.

Chapter 4 introduces the TSD model and expands on its computational details and *material database* characterization. This is followed by a description of the *Moving Least Squares* approximation method, which is used to compute the macroscopic quantities for a given macroscopic strain. The implementation of the TSD model, detailing its *material database* construction and interpolation procedure, is then presented, along with its algorithm.

Chapter 5 evaluates the TSD models efficiency by investigating its numerical accuracy and computational performance, for a series of macroscopic strains prescribed to a hyperelastic laminated RVE. To investigate the numerical accuracy, the results from the implemented  $FE^2$  method are treated as the reference solution. Computational times of both techniques are compared to evaluate the TSD models computational performance.

Chapter 6 continues this evaluation through the analysis of a macroscopic cantilever beam, subjected to different loading types. The RVE considered here is the same as that described in Chapter 5. A comparison of the  $FE^2$  method and TSD models rate of convergence, for each load type, is also undertaken.

Chapter 7 summarizes the results and findings, from both the  $FE^2$  method and TSD model, in which conclusions are then drawn. Improvements to the TSD model are proposed and future works for both models discussed.

# Chapter 2

## Micro-macro continuum mechanics

We define two different scales in the analysis of microheterogeneous materials, the macro and micro. The macro scale is the characteristic length  $L$  of the material sample. The micro scale, which has a characteristic length  $l$ , is much larger than the heterogeneities of the material, but much smaller than the macroscopic characteristic length. In this case, the microscopic length scale being much larger than the molecular dimensions justifies a continuum approach for each constituent. The differences between the scales are illustrated in Figure 2.1 and can be expressed by

$$l \ll L. \tag{2.1}$$

This *separation of scales* allows one to attach a microstructure to point on the macro scale, the repetition of which generates a material that can be assumed to be macroscopically homogeneous. Deciding on the correct length scale for the microstructure is a difficult task. It needs to be large enough to capture the effects of the various constituents contained in the microstructure, but also small enough to enable the macroscopic quantities at a point to be associated with the microstructure. For examples of how the length scales can vary, we refer to Nemat-Nasser and Hori [71]. In cases where the size of the constituents are of the same order as the macroscopic length, meaning that the scale separation theory is no longer valid, a multigrid solution procedure can be adopted [64].

The association of a microstructure to a macroscopic point assumes that the macroscopic quantities are constant across the microstructure [54]. This assumption is essential as it permits the transition of variables between the two scales. Based on finite element discretizations at both scales, we compute a macroscopic boundary value problem by considering a boundary value problem on the microstructure, at integration points across the macrostructure.

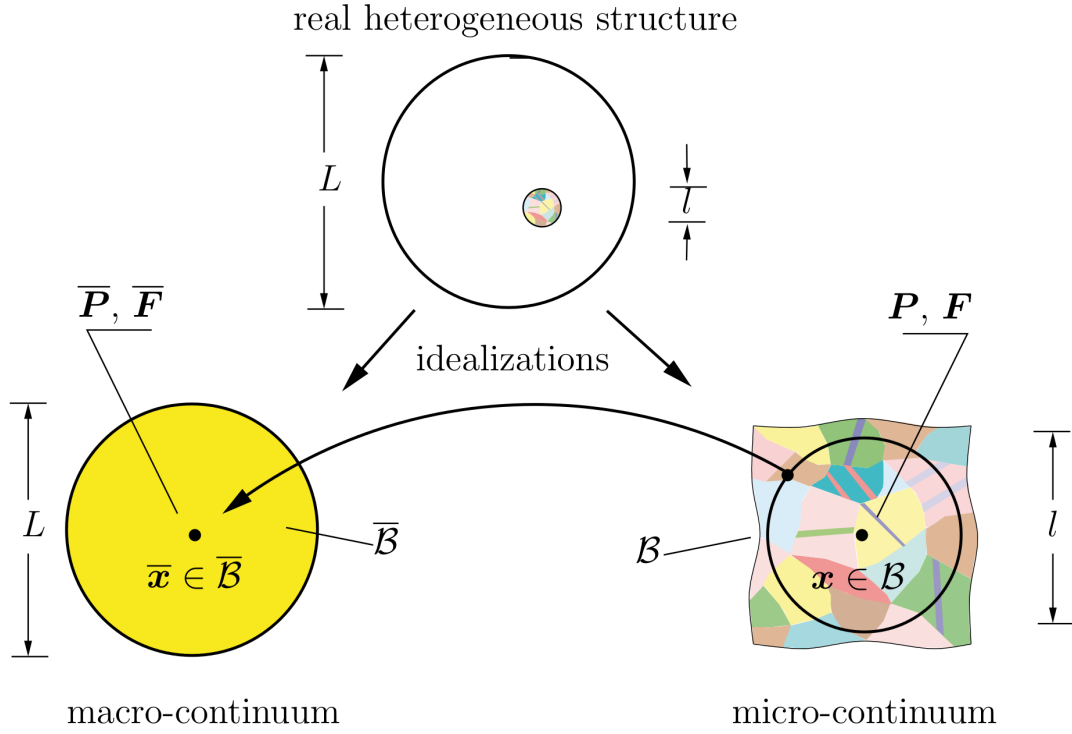


Figure 2.1: Schematic representation of the two-scale homogenization scheme, taken from Schröder [90]: the heterogeneous material is idealized as a homogeneous material at the macro scale (left), with the heterogeneities of the material fully captured in the microstructure (right). We denote here the macroscopic first *Piola-Kirchhoff* stress tensor  $\bar{\mathbf{P}}$  and *deformation gradient*  $\bar{\mathbf{F}}$  at the macroscopic point and their microscopic counterparts  $\mathbf{P}$  and  $\mathbf{F}$ , which vary across the microstructure.

In the case of mechanical problems, the two-scale homogenization procedure requires the following:

- Identification of an RVE, which represents the microstructure and contains enough information to characterize a modulus that is independent of surface tractions and displacements and statistically represents the material, homogeneously, at the macro level.
- Assignment of suitable boundary conditions to the RVE, which sets up the boundary value problem at the micro scale. These boundary conditions satisfy the *macro-homogeneity condition*, otherwise known as the *Hill* or *Hill-Mandel condition*, which equates the virtual power between the two scales and is the fundamental assumption for the micro-macro transition of quantities.
- Discretization of the macro and microscopic boundary value problem.

In this work, we describe the  $\text{FE}^2$  method in a *deformation driven* approach. In other words, the macroscopic problem is formulated as: given a macroscopic deformation, determine the macroscopic stress and tangent operator, based on the response of the microstructure.

The behaviour at the macro and micro scales are described using continuum mechanics. Continuum mechanics is a method used to describe physical phenomena by studying the



kinematics and stress in a continuum using balance principles that are governed by the fundamental laws of physics. An underlying assumption here is the treatment of the material as a continuous medium, whose molecular structure is generalised by the overlying material properties. A stress and strain relation can thus characterize each point in the body. The macroscopic stress-strain relationship is determined via suitable averaging methods over the RVE, while constitutive models are set up for the stress-strain relationship at the micro scale.

The next three sections discuss the basic principles of continuum mechanics at each scale, respectively, and the coupling of quantities between them. For further detailed descriptions and derivations, the reader may refer to Holzapfel [38], Mase et al. [60], Lai et al. [51] and Schröder [90]. In describing the continuum mechanics at the micro level, we define the microscopic body as a Representative Volume Element (RVE). Details into its definition and identification are discussed in Section 2.4. For ease of reference, we shall denote quantities at the macro scale using the notation  $(\overline{\bullet})$ .

## 2.1 Macro continuum

### 2.1.1 Kinematics

Consider a macroscopic body  $\overline{\mathcal{B}}$  in a three-dimensional Euclidean space, having a macroscopic particle  $\overline{\mathcal{P}} \in \overline{\mathcal{B}}$ , at a given instance of time  $t$ . At the initial time state  $t = 0$ , we introduce the reference, material or undeformed configuration and parametrise the macroscopic particle  $\overline{\mathcal{P}} \in \overline{\mathcal{B}}_0$  with Cartesian coordinates  $\overline{X}_1$ ,  $\overline{X}_2$  and  $\overline{X}_3$ , where the associated basis vectors are denoted by  $e_1$ ,  $e_2$  and  $e_3$ . After the body is subjected to boundary conditions for a time  $t > 0$ , the body is now taken to be in a deformed state  $\overline{\mathcal{B}}_t$ . We refer to this as the current, spatial or deformed configuration and now parametrise the macroscopic particle  $\overline{\mathcal{P}} \in \overline{\mathcal{B}}_t$  with  $\overline{x}_1$ ,  $\overline{x}_2$  and  $\overline{x}_3$ . The motion of the body  $\overline{\mathcal{B}}$  can be represented by a non-linear macroscopic deformation mapping  $\overline{\gamma} : \overline{\mathcal{B}}_0 \rightarrow \overline{\mathcal{B}}_t$ . This enables us to define the relation of the macroscopic particle between the reference configuration  $\overline{\mathbf{X}} \in \overline{\mathcal{B}}_0$  and the current configuration  $\overline{\mathbf{x}} \in \overline{\mathcal{B}}_t$ :

$$\overline{\mathbf{x}} = \overline{\gamma}(\overline{\mathbf{X}}, t). \quad (2.2)$$

The following macroscopic operators considered here are defined in Table 2.1 for the reference and current configuration, respectively.

Table 2.1: Macroscopic gradient and divergence operators for reference and current configuration.

Operator	Configuration	
	Reference	Current
Gradient	$\text{Grad}_{\overline{\mathbf{X}}}(\bullet) = \nabla_{\overline{\mathbf{X}}}(\bullet) = \frac{\partial}{\partial \overline{\mathbf{X}}}(\bullet)$	$\text{grad}_{\overline{\mathbf{x}}}(\bullet) = \nabla_{\overline{\mathbf{x}}}(\bullet) = \frac{\partial}{\partial \overline{\mathbf{x}}}(\bullet)$
Divergence	$\text{Div}_{\overline{\mathbf{X}}}(\bullet) = \nabla_{\overline{\mathbf{X}}} \cdot (\bullet) = \frac{\partial}{\partial \overline{X}_i}(\bullet) \cdot e_i$	$\text{div}_{\overline{\mathbf{x}}}(\bullet) = \nabla_{\overline{\mathbf{x}}} \cdot (\bullet) = \frac{\partial}{\partial \overline{x}_i}(\bullet) \cdot e_i$



Taking the gradient of the deformation map in Equation (2.2), with respect to the reference configuration, we obtain the invertible linear deformation map termed the *macroscopic deformation gradient*:

$$\bar{\mathbf{F}} = \text{Grad}_{\bar{\mathbf{X}}} \bar{\gamma} = \frac{\partial \bar{\gamma}(\bar{\mathbf{X}}, t)}{\partial \bar{\mathbf{X}}} = \frac{\partial \bar{\mathbf{x}}}{\partial \bar{\mathbf{X}}}. \quad (2.3)$$

This deformation gradient can be rewritten using the relation for the macroscopic displacement field,  $\bar{\mathbf{u}}(\bar{\mathbf{X}}, t) = \bar{\mathbf{x}}(\bar{\mathbf{X}}, t) - \bar{\mathbf{X}}$ , as

$$\bar{\mathbf{F}} = \mathbf{I} + \nabla_{\bar{\mathbf{X}}} \bar{\mathbf{u}}. \quad (2.4)$$

To perform the change in volume from  $\bar{\mathcal{B}}_0$  to  $\bar{\mathcal{B}}_t$ , we compute the *Jacobian* at the macro scale

$$\bar{J} = \det \bar{\mathbf{F}} > 0. \quad (2.5)$$

In cases where no deformation takes place, the volume remains unchanged, i.e.  $\bar{\mathcal{B}}_0 = \bar{\mathcal{B}}_t$ , and thus  $\bar{\mathbf{F}} = \mathbf{I}$  and  $\bar{J} = 1$ . In cases where the macroscopic volume does change, a relation between the volume in the reference configuration  $d\bar{V}$  and its counterpart in the current configuration  $d\bar{v}$  can be defined

$$d\bar{v} = \det(\bar{\mathbf{F}}) d\bar{V} = \bar{J} d\bar{V}. \quad (2.6)$$

Similarly, a surface element in the current configuration  $d\bar{a}$  can be expressed in terms of the reference configuration  $d\bar{A}$ :

$$\bar{\nu} d\bar{a} = \det(\bar{\mathbf{F}}) \bar{\mathbf{F}}^{-T} \bar{\mathbf{n}} d\bar{A}, \quad (2.7)$$

where  $\bar{\nu}$  and  $\bar{\mathbf{n}}$  are the unit normal vectors on the surface elements, in the current and reference configuration, respectively. For quantities that can vary with time, we compute the material time derivative  $\frac{D(\bullet)}{Dt}$ . The Jacobian, which is the volume ratio between the configurations, is one such quantity that can vary with time:

$$\frac{D\bar{J}}{Dt} = \dot{\bar{J}} = \bar{J} \text{div}_{\bar{\mathbf{x}}} \dot{\bar{\mathbf{x}}}. \quad (2.8)$$

A suitable deformation measure in this work is the macroscopic right *Cauchy-Green deformation tensor*, defined using the macroscopic deformation gradient,

$$\bar{\mathbf{C}} = \bar{\mathbf{F}}^T \bar{\mathbf{F}}. \quad (2.9)$$

A further strain measure, referred to as the *Green Lagrange* strain tensor and is symmetric in nature, can be defined as a function of the right *Cauchy-Green deformation tensor*:

$$\bar{\mathbf{E}} = \frac{1}{2} (\bar{\mathbf{C}} - \mathbf{I}) = \frac{1}{2} (\bar{\mathbf{F}}^T \bar{\mathbf{F}} - \mathbf{I}). \quad (2.10)$$

The macroscopic deformation gradient can be decomposed into an orthogonal rotation tensor  $\bar{\mathbf{R}}$  and a symmetric positive-definite stretch tensor  $\bar{\mathbf{U}}$  using polar decomposition,

$$\bar{\mathbf{F}} = \bar{\mathbf{R}}\bar{\mathbf{U}}. \quad (2.11)$$

An alternative form of the right *Cauchy-Green deformation tensor* can then be defined using Equation (2.9)

$$\bar{\mathbf{C}} = \bar{\mathbf{U}}^2. \quad (2.12)$$

Having the same eigenvectors, we express the stretch tensor in terms of the right *Cauchy-Green deformation tensor*, using spectral decomposition:

$$\bar{\mathbf{U}} = \sum_{i=1,2,3}^i \sqrt{\lambda_i^{\bar{\mathbf{C}}}} \hat{\mathbf{n}}_i^{\bar{\mathbf{C}}} \otimes \hat{\mathbf{n}}_i^{\bar{\mathbf{C}}}, \quad (2.13)$$

where  $\lambda_i^{\bar{\mathbf{C}}}$  and  $\hat{\mathbf{n}}_i^{\bar{\mathbf{C}}}$  are the eigenvalues and eigenvectors of the macroscopic right *Cauchy-Green deformation tensor*  $\bar{\mathbf{C}}$ .

### 2.1.2 Stress

In continuum mechanics, the distribution of internal forces on a deformed macroscopic body  $\bar{\mathcal{B}}_t$  is expressed using stress measures. These stress measures are internal reactions to externally applied forces, which can be either macroscopic body forces  $\bar{\mathbf{b}}$ , surface tractions  $\bar{\mathbf{t}}^{(\bar{\nu})}$  or both. Surface tractions  $\bar{\mathbf{t}}^{(\bar{\nu})}$  are referred to as *traction vectors*, which act on the body's surface with a unit normal vector  $\bar{\nu}$ .

Using the *Cauchy stress principle*, the infinitesimal resultant force  $d\bar{\mathbf{f}}$  acting on an infinitesimal surface element  $d\bar{a}$ , inside the body  $\bar{\mathcal{B}}_t$ , yields:

$$\frac{d\bar{\mathbf{f}}}{d\bar{a}} = \bar{\mathbf{t}}^{(\bar{\nu})}. \quad (2.14)$$

The stress state at each point  $\bar{\mathbf{x}} \in \bar{\mathcal{B}}_t$  can thus be given by the *Cauchy stress lemma*:

$$\bar{\mathbf{t}}^{(\bar{\nu})}(\bar{\mathbf{x}}, t) = \bar{\boldsymbol{\sigma}}^T(\bar{\mathbf{x}}, t) \bar{\boldsymbol{\nu}}(\bar{\mathbf{x}}, t), \quad (2.15)$$

where  $\bar{\boldsymbol{\sigma}}$  denotes the symmetric *Cauchy* stress tensor, in the current configuration, at the current macroscopic point  $\bar{\mathbf{x}}$ . To represent the stress in the current configuration, which acts on the reference surface element  $d\bar{A}$  with a unit normal  $\bar{\mathbf{n}}$ , we reformulate Equation (2.15) into the following:

$$\bar{\mathbf{t}}^{(\bar{\mathbf{n}})}(\bar{\mathbf{X}}, t) = \bar{\mathbf{P}}(\bar{\mathbf{X}}, t) \bar{\mathbf{n}}(\bar{\mathbf{X}}, t), \quad (2.16)$$

with  $\bar{\mathbf{P}}$  representing the stress in the current configuration, at the macroscopic reference point  $\bar{\mathbf{X}}$ . The macroscopic stress  $\bar{\mathbf{P}}$  is known as the first *Piola-Kirchhoff* stress tensor and can also be computed using the macroscopic deformation gradient and the second *Piola-Kirchhoff* stress tensor,  $\bar{\mathbf{S}}$ :

$$\bar{\mathbf{P}} = \bar{\mathbf{F}} \bar{\mathbf{S}} \quad (2.17)$$

We note here that, similar to  $\bar{\mathbf{F}}$ , the first *Piola-Kirchhoff* stress tensor  $\bar{\mathbf{P}}$  is not symmetric, unlike the *Cauchy* stress tensor  $\bar{\boldsymbol{\sigma}}$  and second *Piola-Kirchhoff* stress tensor  $\bar{\mathbf{S}}$ .

### 2.1.3 Balance of linear momentum

We consider the macroscopic body  $\bar{\mathcal{B}}$  that is subjected to a body force  $\bar{\mathbf{b}}$  and a surface traction  $\bar{\mathbf{t}}^{(\bar{\nu})}$ , which is applied to a surface boundary  $\partial\bar{\mathcal{B}}$ . In this context, we define the law of linear momentum conservation at the macro scale to be the rate of change of linear momentum that is equal to the total resultant force acting on the macroscopic body:

$$\frac{d}{dt} \int_{\bar{\mathcal{B}}_t} \rho(\bar{\mathbf{x}}, t) \bar{\mathbf{x}} d\bar{v} = \int_{\partial\bar{\mathcal{B}}_t} \bar{\mathbf{t}}^{(\bar{\nu})}(\bar{\mathbf{x}}, t) d\bar{a} + \int_{\bar{\mathcal{B}}_t} \bar{\mathbf{b}}(\bar{\mathbf{x}}, t) d\bar{v}, \quad (2.18)$$

where  $\rho(\bar{\mathbf{x}}, t)$  is the current density of the macroscopic body at time  $t$ . The global equation of motion in its spatial form can be obtained from this balance equation using the *Cauchy stress lemma* (Equation (2.15)) and Gauss divergence theorem,

$$\int_{\bar{\mathcal{B}}_t} \{ \rho(\bar{\mathbf{x}}, t) \ddot{\bar{\mathbf{x}}} - \text{div}_{\bar{\mathbf{x}}} \bar{\boldsymbol{\sigma}}^T - \bar{\mathbf{b}}(\bar{\mathbf{x}}, t) \} d\bar{v} = 0, \quad (2.19)$$

which can be reduced to its local form, as the integral over the macroscopic body  $\bar{\mathcal{B}}_t$  is arbitrary,

$$\rho(\bar{\mathbf{x}}, t) \ddot{\bar{\mathbf{x}}} - \text{div}_{\bar{\mathbf{x}}} \bar{\boldsymbol{\sigma}}^T - \bar{\mathbf{b}}(\bar{\mathbf{x}}, t) = \mathbf{0}. \quad (2.20)$$

If we neglect the acceleration field  $\ddot{\bar{\mathbf{x}}}$ , this equation of motion can be further reduced to the following equilibrium equation:

$$\text{div}_{\bar{\mathbf{x}}} \bar{\boldsymbol{\sigma}}^T + \bar{\mathbf{b}}(\bar{\mathbf{x}}, t) = \mathbf{0}. \quad (2.21)$$

The equilibrium equation above can be expressed in its material form when converting the quantities in Equation (2.18) from the current to the reference configuration. In this case, we define the balance of linear momentum as:

$$\frac{d}{dt} \int_{\bar{\mathcal{B}}_0} \rho(\bar{\mathbf{X}}, t) \dot{\bar{\mathbf{x}}} d\bar{V} = \int_{\partial \bar{\mathcal{B}}_0} \bar{\mathbf{t}}^{(\bar{n})}(\bar{\mathbf{X}}, t) d\bar{A} + \int_{\bar{\mathcal{B}}_0} \bar{\mathbf{b}}(\bar{\mathbf{X}}, t) d\bar{V}. \quad (2.22)$$

Using the *Cauchy stress lemma*, which is expressed in the mixed configuration in Equation (2.16), and Gauss divergence theorem, the global equation of motion is given

$$\int_{\bar{\mathcal{B}}_0} \{ \rho(\bar{\mathbf{X}}, t) \ddot{\bar{\mathbf{x}}} - \text{Div}_{\bar{\mathbf{X}}} \bar{\mathbf{P}} - \bar{\mathbf{b}}(\bar{\mathbf{X}}, t) \} d\bar{V} = \mathbf{0}. \quad (2.23)$$

We again take the integral over the macroscopic body  $\bar{\mathcal{B}}$  to be arbitrary, giving the local form

$$\rho(\bar{\mathbf{x}}, t) \ddot{\bar{\mathbf{x}}} - \text{Div}_{\bar{\mathbf{X}}} \bar{\mathbf{P}} - \bar{\mathbf{b}}(\bar{\mathbf{X}}, t) = \mathbf{0}, \quad (2.24)$$

which is referred to as the *Lagrangian equation of motion*. If the acceleration field  $\ddot{\bar{\mathbf{x}}}$  is zero, then the equilibrium equation can be expressed, in its material form, as

$$\text{Div}_{\bar{\mathbf{X}}} \bar{\mathbf{P}} + \bar{\mathbf{b}}(\bar{\mathbf{X}}, t) = \mathbf{0} \quad (2.25)$$

and is termed the *Lagrangian equilibrium equation*.

## 2.1.4 Variational formulation

The Lagrangian equilibrium equation, which has been defined using the law of conservation of linear momentum, is now used to construct the macroscopic boundary value problem. This differential equation, in which the macroscopic displacement field  $\bar{\mathbf{u}}$  is the unknown, is solved using the standard Finite Element Method (FEM). To cater for the external forces, two types of boundary conditions are specified on the surface region of the macroscopic body  $\bar{\mathcal{B}}$ . The first type is Dirichlet boundary conditions, applied on  $\partial \bar{\mathcal{B}}_D$ , which are prescribed displacements and resemble the support reactions, for example. The second condition is von Neumann boundary conditions, applied on  $\partial \bar{\mathcal{B}}_N$ , and are typically considered to be imposed traction forces. These boundary conditions are prescribed such that  $\partial \bar{\mathcal{B}}_D \subset \partial \bar{\mathcal{B}}$  and  $\partial \bar{\mathcal{B}}_N \subset \partial \bar{\mathcal{B}}$  and that:

$$\partial\bar{\mathcal{B}}_D \cup \partial\bar{\mathcal{B}}_N = \partial\bar{\mathcal{B}}_0 \quad \text{and} \quad \partial\bar{\mathcal{B}}_D \cap \partial\bar{\mathcal{B}}_N = \emptyset. \quad (2.26)$$

Using the boundary conditions, the *strong form* of the macroscopic boundary value problem is given:

$$\text{Div}_{\bar{\mathbf{X}}} \bar{\mathbf{F}} \bar{\mathbf{S}} - \bar{\mathbf{b}}_{\bar{\mathcal{B}}} = \mathbf{0} \quad \text{in} \quad \bar{\mathcal{B}} \quad (2.27)$$

$$\bar{\mathbf{u}} = \check{\bar{\mathbf{u}}} \quad \text{on} \quad \partial\bar{\mathcal{B}}_D, \quad (2.28)$$

$$\check{\bar{\mathbf{t}}}^{(\bar{\mathbf{n}})} \quad \text{on} \quad \partial\bar{\mathcal{B}}_N \quad (2.29)$$

where  $\check{\bar{\mathbf{u}}}$  and  $\check{\bar{\mathbf{t}}}$  are the prescribed displacements and tractions on the surface boundaries, respectively. A weak form of the above can be obtained when multiplying Equation (2.27) by an arbitrary function  $\delta\bar{\mathbf{u}}$ , integrating over the macroscopic body  $\bar{\mathcal{B}}$  and applying the Gauss divergence theorem (all of which we collectively refer to as the weighted residual method),

$$\int_{\bar{\mathcal{B}}_0} \bar{\mathbf{S}} : \delta\bar{\mathbf{E}} \, d\bar{V} = \int_{\bar{\mathcal{B}}_0} \bar{\mathbf{b}} \cdot \delta\bar{\mathbf{u}} \, d\bar{V} + \int_{\partial\bar{\mathcal{B}}_0} \check{\bar{\mathbf{t}}}^{(\bar{\mathbf{n}})} \cdot \delta\bar{\mathbf{u}} \, d\bar{A}. \quad (2.30)$$

In continuum mechanics, the variational formulation is primarily associated to the principle of virtual work. This principle distinguishes between the virtual external work  $\mathcal{W}_{ext}$  and the associated virtual internal potential  $\mathcal{W}_{int}$ . The virtual external work is that done by the body and traction forces, in this case

$$\bar{\mathcal{W}}_{ext} = \int_{\bar{\mathcal{B}}_0} \bar{\mathbf{b}} \cdot \delta\bar{\mathbf{u}} \, d\bar{V} + \int_{\partial\bar{\mathcal{B}}_0} \check{\bar{\mathbf{t}}}^{(\bar{\mathbf{n}})} \cdot \delta\bar{\mathbf{u}} \, d\bar{A}, \quad (2.31)$$

while the internal potential is that generated by the material, in response to the loads applied

$$\bar{\mathcal{W}}_{int} = \int_{\bar{\mathcal{B}}_0} \bar{\mathbf{S}} : \delta\bar{\mathbf{E}} \, d\bar{V}. \quad (2.32)$$

The virtual *Green* strain tensor  $\delta\bar{\mathbf{E}}$  above can be further expanded, in index notation, using Equations (2.4) and (2.9),

$$\delta\bar{E}_{ij} = \frac{1}{2} \delta(\bar{F}_{ri} \bar{F}_{rj}) = \frac{1}{2} (\delta\bar{u}_{r,i} \bar{F}_{rj} + \bar{F}_{ri} \delta\bar{u}_{r,j}). \quad (2.33)$$

For index notation, we denote the gradient operator in the reference configuration, in Table 2.1, as  $\frac{\partial(\bullet)}{\partial\bar{x}_i} = (\bar{\bullet})_{,i}$ . The principle of virtual work requires the virtual internal potential to be equal to the virtual external work,

$$\bar{\mathcal{W}}_{int} = \bar{\mathcal{W}}_{ext}. \quad (2.34)$$

Equilibrium is thus attained when the following relation is satisfied:

$$\overline{\mathcal{F}} = \overline{\mathcal{W}}_{int} - \overline{\mathcal{W}}_{ext} = 0. \quad (2.35)$$

To obtain this equilibrium, and the unknown displacement field, a *Newton-Raphson* iteration scheme is employed. This solving scheme requires the linearization of Equation (2.35), using a first-order Taylor expansion near the known displacement field,  $\overline{\mathbf{u}}^{i-1}$ . The general linearized expression, for the current iteration step,  $i$ , of the incremental loading step,  $n$ , can be expressed as

$$\overline{\mathcal{F}}(\overline{\mathbf{u}}_n^i) = \overline{\mathcal{F}}(\overline{\mathbf{u}}_n^{i-1} + \Delta\overline{\mathbf{u}}) = \overline{\mathcal{F}}(\overline{\mathbf{u}}_n^{i-1}) + \left. \frac{\partial \overline{\mathcal{F}}}{\partial \overline{\mathbf{u}}} \right|_{\overline{\mathbf{u}}_n^{i-1}} \Delta\overline{\mathbf{u}} \approx 0, \quad (2.36)$$

with  $\Delta\overline{\mathbf{u}}$  being the incremental displacement field. By solving the incremental displacement field, the unknown displacement field in the current iteration step can be computed

$$\overline{\mathbf{u}}_i^n = \overline{\mathbf{u}}_{i-1}^n + \Delta\overline{\mathbf{u}}. \quad (2.37)$$

The linearization of Equation (2.35) requires the right *Green Lagrange* strain tensor, its virtual counterpart and the Second *Piola-Kirchhoff* stress tensor to be linearized. For the sake of simplicity then, we introduce the following expression

$$\Delta(\bullet) := \frac{\partial(\bullet)}{\partial \overline{\mathbf{u}}} \Delta\overline{\mathbf{u}} \quad (2.38)$$

and derive these respective linearized quantities, in index notation, as:

$$\Delta \overline{E}_{ij} = \frac{1}{2} \Delta(\overline{F}_{ri} \overline{F}_{rj}) = \frac{1}{2} (\Delta \overline{u}_{r,i} \overline{F}_{rj} + \overline{F}_{ri} \Delta \overline{u}_{r,j}), \quad (2.39)$$

$$\Delta \delta \overline{E}_{ij} = \frac{1}{2} (\Delta \overline{u}_{r,i} \delta \overline{u}_{r,j} + \delta \overline{u}_{r,i} \Delta \overline{u}_{r,j}), \quad (2.40)$$

$$\Delta \overline{S}_{ij} = \frac{\partial \overline{S}_{ij}}{\partial \overline{E}_{kl}} \Delta \overline{E}_{kl} = \mathbb{H}_{ijkl} (\overline{F}_{rk} \Delta \overline{u}_{r,l}). \quad (2.41)$$

In the linearized Second *Piola-Kirchhoff* stress tensor derivation, we have the macroscopic tangent operator,

$$\overline{\mathbb{H}} = \frac{\partial \overline{\mathbf{S}}}{\partial \overline{\mathbf{E}}} = 2 \frac{\partial \overline{\mathbf{S}}}{\partial \overline{\mathbf{C}}}. \quad (2.42)$$

We now derive the linearized form of the principle of virtual work by expanding on Equation (2.36), with Equation (2.30), using the chain rule and the linearized quantities above,

Equations (2.39) to (2.41). By exploiting the symmetries of both,  $\bar{\mathbf{S}}$  and  $\bar{\mathbf{E}}$ , the derivation is expressed, in index notation, as:

$$\begin{aligned}
\bar{\mathcal{F}} &= \int_{\bar{\mathcal{B}}_0} \bar{S}_{ij} \delta \bar{E}_{ij} d\bar{V} - \int_{\bar{\mathcal{B}}_0} \bar{b}_i \delta \bar{u}_i d\bar{V} - \int_{\partial \bar{\mathcal{B}}_0} \bar{t}_i^{(\bar{\mathbf{n}})} \delta \bar{u}_i d\bar{A} \\
&\quad + \int_{\bar{\mathcal{B}}_0} \Delta \bar{S}_{ij} \delta \bar{E}_{ij} + \bar{S}_{ij} \Delta \delta \bar{E}_{ij} d\bar{V} \\
&= \int_{\bar{\mathcal{B}}_0} \bar{S}_{ij} \bar{F}_{ri} \delta \bar{u}_{r,j} d\bar{V} - \int_{\bar{\mathcal{B}}_0} \bar{b}_i \delta \bar{u}_i d\bar{V} - \int_{\partial \bar{\mathcal{B}}_0} \bar{t}_i^{(\bar{\mathbf{n}})} \delta \bar{u}_i d\bar{A} \\
&\quad + \int_{\bar{\mathcal{B}}_0} \bar{\mathbb{H}}_{ijkl} \bar{F}_{rk} \Delta \bar{u}_{r,l} \bar{F}_{si} \delta \bar{u}_{s,j} + \bar{S}_{ij} \Delta \bar{u}_{r,i} \delta \bar{u}_{r,j} d\bar{V} = 0.
\end{aligned} \tag{2.43}$$

Traditionally, the macroscopic stress  $\bar{\mathbf{S}}$  and tangent operator  $\bar{\mathbb{H}}$  values are obtained via stored strain energy functions, describing the material in question. In this case, however, these macroscopic quantities are obtained by homogenizing the results of the RVE, at the micro scale.

## 2.2 Micro continuum

In describing the continuum at the micro scale, we consider the microscopic body  $\mathcal{B}$  to be a *Representative Volume Element*, RVE. As previously mentioned, the RVE is a characteristic volume containing sufficient information to characterize the composite at the macro scale. The RVE is thus a heterogeneous material, with each constituent having its phenomenological description. Further details into the identification of the RVE are discussed in Section 2.4. The derivation of the variational formulation at the micro scale makes two key assumptions:

1. the effects of inertia are ignored; and
2. no external forces exist at the micro-level.

These assumptions are based on the macro-homogeneity condition and the kinematic constraint placed on the RVE. The principles governing the micro continuum are similar to the macro continuum. We thus refer to the kinematic and stress measures, defined in Sections 2.1.1 and 2.1.2, and summarize the necessary quantities below.

### 2.2.1 Kinematics, stress and balance equations

Similar to the macro scale, we parametrize the microscopic particle  $\mathcal{P} \in \mathcal{B}_0$  in the reference configuration with Cartesian coordinates  $\mathbf{X}$  at  $t = 0$ . The transformation of the point  $\mathbf{X}$  to the current configuration, for the deformed microscopic body  $\mathcal{B}_t$ , is achieved using the non-linear microscopic deformation map  $\gamma(\mathbf{X}, t)$ ,

$$\mathbf{x} = \gamma(\mathbf{X}, t). \tag{2.44}$$

Definitions for the operators at the micro scale are provided in Table 2.2, for both the reference and current configurations.

Table 2.2: Microscopic gradient and divergence operators for reference and current configuration.

Operator	Configuration	
	Reference	Current
Gradient	$\text{Grad}_{\mathbf{X}}(\bullet) = \nabla_{\mathbf{X}}(\bullet) = \frac{\partial}{\partial \mathbf{X}}(\bullet)$	$\text{grad}_{\mathbf{x}}(\bullet) = \nabla_{\mathbf{x}}(\bullet) = \frac{\partial}{\partial \mathbf{x}}(\bullet)$
Divergence	$\text{Div}_{\mathbf{X}}(\bullet) = \nabla_{\mathbf{X}} \cdot (\bullet) = \frac{\partial}{\partial X_i}(\bullet) \cdot e_i$	$\text{div}_{\mathbf{x}}(\bullet) = \nabla_{\mathbf{x}} \cdot (\bullet) = \frac{\partial}{\partial x_i}(\bullet) \cdot e_i$

We express the microscopic deformation gradient as,

$$\mathbf{F} = \mathbf{I} + \nabla_{\mathbf{X}} \mathbf{u}, \quad (2.45)$$

with the microscopic displacement field,  $\mathbf{u}(\mathbf{X}, t) = \mathbf{x}(\mathbf{X}, t) - \mathbf{X}$ . The microscopic right *Cauchy-Green* deformation tensor is thus defined,

$$\mathbf{C} = \mathbf{F}^T \mathbf{F}, \quad (2.46)$$

along with the *Green Lagrange* strain tensor,

$$\mathbf{E} = \frac{1}{2} (\mathbf{C} - \mathbf{I}) = \frac{1}{2} (\mathbf{F}^T \mathbf{F} - \mathbf{I}). \quad (2.47)$$

For stress measures we use the *Cauchy stress principle* and *Cauchy stress lemma* to express the microscopic first *Piola-Kirchhoff* stress tensor, acting at a point  $\mathbf{X} \in \mathcal{B}$  on the microscopic surface  $dA$ , with a unit normal vector  $\mathbf{n}$ ,

$$\mathbf{t}^{(n)}(\mathbf{X}, t) = \mathbf{P}(\mathbf{X}, t) \mathbf{n}(\mathbf{X}, t). \quad (2.48)$$

The balance of linear momentum is derived at the micro scale using the same principles as that discussed in Section 2.1.3. However, in this case body forces are neglected. Following the same procedure at the macro scale then, we express the *Lagrangian equilibrium equation* at the micro scale as:

$$\text{Div}_{\mathbf{X}} \mathbf{P} = \mathbf{0}. \quad (2.49)$$



## 2.2.2 Variational formulation

As mentioned before, the principle of virtual work on the RVE assumes the external tractions and body forces to be zero. This exclusion comes as a result of the macro-homogeneity condition, which only holds if the RVE is kinematically constrained, forcing the virtual work of these microscopic forces to vanish, see de Souza Neto and Feijóo [11]. Without a kinematical constraint then, the microscopic boundary value problem is ill-posed. Various models, which kinematically constrain the RVE, are discussed in Section 2.3.3. In this work, we use the *periodic boundary displacement* model, which stems from the periodicity assumption and employs periodic boundary conditions on the RVE (see Kouznetsova et al. [48]). This condition does not constrain nor free the boundaries of the RVE, but instead geometrically enforces them. Boundaries of the RVE are split into two parts,  $\partial\mathcal{B}_0^+$  and  $\partial\mathcal{B}_0^-$ , such that:

$$\partial\mathcal{B}_0^+ \cup \partial\mathcal{B}_0^- = \partial\mathcal{B}_0. \quad \text{and} \quad \partial\mathcal{B}_0^+ \cap \partial\mathcal{B}_0^- = \emptyset. \quad (2.50)$$

The two parts are defined such that,

$$\mathbf{n}^- = -\mathbf{n}^+ \quad \forall \mathbf{X}^- \in \partial\mathcal{B}_0^- \quad \text{and} \quad \forall \mathbf{X}^+ \in \partial\mathcal{B}_0^+, \quad (2.51)$$

as illustrated in Figure 2.2. The periodic boundary condition can then be represented, in its general form, as:

$$\mathbf{x}^+ - \mathbf{x}^- = \overline{\mathbf{F}}(\mathbf{X}^+ - \mathbf{X}^-) \quad \text{and} \quad (2.52)$$

$$\mathbf{t}_0^{(n^+)} = -\mathbf{t}_0^{(n^-)} \quad (2.53)$$

where Equations (2.52) and (2.53) are the periodic deformations and anti-periodic tractions, on the associated boundaries, respectively.

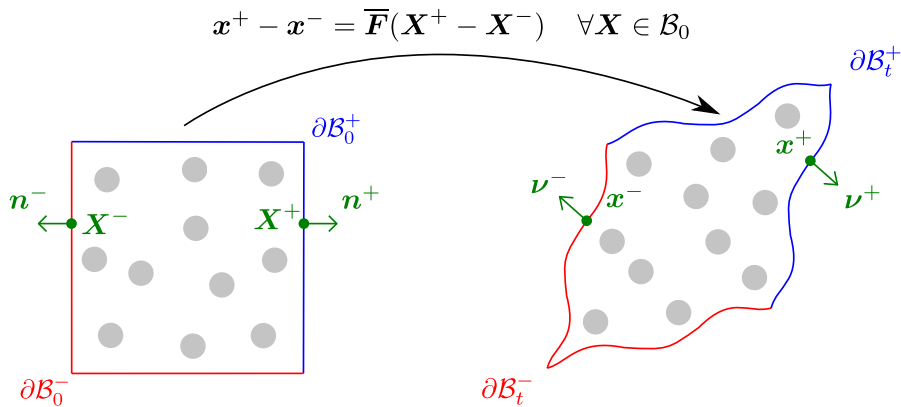


Figure 2.2: Splitting arrangement of the RVE prior to solving the *periodic boundary displacement* model (left) and the deformed result after (right).

As per the macro scale, the standard FE framework is used to solve the microscopic displacement field  $\mathbf{u}$ . Using the *Lagrangian equilibrium equation* (2.49), in the absence of body forces and external tractions, the principle of virtual work defines the RVE to be in equilibrium if,

$$\mathcal{F} = \int_{\mathcal{B}_0} \mathbf{P} : \delta \mathbf{F} dV = 0. \quad (2.54)$$

As per the macro scale, a *Newton-Raphson* iteration scheme is used to attain equilibrium. The microstructural characteristics of each constituent, contained in the heterogeneous RVE, are described by their respective constitutive laws.

## 2.3 Coupling the macro and micro continuum

The coupling of quantities between the two scales follows the *Hill-Mandel Principle of Macro-Homogeneity*, introduced by Hill [34, 36] and Mandel [58]. More commonly known as the *macro-homogeneity condition*, the condition follows from the separation of scales theory and preserves the energy between the scales. This preservation allows the macro-to-micro transition, which provides the kinematic constraint and sets up the boundary value problem on the RVE. The micro-to-macro transition utilizes the averaging theorems, developed by Hill [36, 37] and Nemat-Nasser [70], and expresses the macroscopic quantities as volume averages of their microscopic counterparts.

We first introduce the micro-to-macro transition of the kinematic and stress measures, respectively. In this context, we assume the RVE to have no holes or voids; however, these techniques can easily be extended to accommodate this, in which we refer to Schröder [90]. The macro-homogeneity condition is then elaborated on and the various micro models, which kinematically constrain the RVE, highlighted. Finally, we discuss the computation of the macroscopic tangent operator. In defining these coupled relations, we follow the workings of Schröder [90] and Kouznetsova et al. [48]. The averaging relations and macro-homogeneity condition, discussed in this work, have recently been proven by Liu and Reina [57] to be exact for finite element discretizations.

### 2.3.1 Kinematics

One of the main assumptions in this coupling approach is that made on the macroscopic deformation gradient, which inherently places a kinematic constraint on the RVE. The macroscopic deformation gradient,  $\bar{\mathbf{F}}$ , at a point  $\bar{\mathbf{x}}$  on the macro continuum is assumed to be equal to the volume average of the microscopic deformation gradient, defined over the microscopic body,  $\mathcal{B}_0$ ,

$$\bar{\mathbf{F}}(t) = \frac{1}{V} \int_{\mathcal{B}_0} \mathbf{F}(\mathbf{x}, t) dV, \quad (2.55)$$

where  $V$  is the reference volume of the RVE. This definition can also be expressed as a surface integral using the divergence theorem:

$$\frac{1}{V} \int_{\mathcal{B}_0} \mathbf{F}(\mathbf{x}, t) dV = \frac{1}{V} \int_{\partial \mathcal{B}_0} \mathbf{x}(t) \otimes \mathbf{n} dA, \quad (2.56)$$

with the outward normal,  $\mathbf{n}$ , acting on the surface of the RVE, in the reference configuration. Using this analogy, we extend the above to the material time derivative case:

$$\dot{\bar{\mathbf{F}}} = \frac{1}{V} \int_{\mathcal{B}_0} \dot{\mathbf{F}} dV = \frac{1}{V} \int_{\partial \mathcal{B}_0} \dot{\mathbf{x}} \otimes \mathbf{n} dA, \quad (2.57)$$

The macroscopic Jacobian,  $\bar{J}$ , can be related to its microscopic counterpart by the volume average in a similar manner:

$$\bar{J} = \frac{1}{V} \int_{\mathcal{B}_0} J dV = \frac{1}{V} \int_{\mathcal{B}_t} dv = \frac{v}{V}, \quad (2.58)$$

where  $v$  is the current RVE volume. We now split the microscopic deformation gradient into two parts, a constant and a fluctuation part,

$$\mathbf{F} = \bar{\mathbf{F}} + \tilde{\mathbf{F}}. \quad (2.59)$$

The constant part is taken to be the macroscopic deformation gradient,  $\bar{\mathbf{F}}$ , which is valid due to the assumption that the macroscopic quantities are constant across the RVE [54]. The fluctuation part,  $\tilde{\mathbf{F}}$ , is inhomogeneous and computed at the micro-level,

$$\tilde{\mathbf{F}} = \text{Grad}_{\mathbf{x}} \tilde{\mathbf{w}}, \quad (2.60)$$

where  $\tilde{\mathbf{w}}$  represents the fluctuations at the micro scale. These fluctuations are the inhomogeneous component of the deformed position vector,  $\mathbf{x}$ , which implies the decomposition:

$$\mathbf{x} = \bar{\mathbf{x}} + \tilde{\mathbf{w}} = \bar{\mathbf{F}} \mathbf{X} + \tilde{\mathbf{w}}, \quad (2.61)$$

where  $\bar{\mathbf{x}} = \bar{\mathbf{F}} \mathbf{X}$  is the homogeneous position vector, linearly mapped by the macroscopic deformation gradient. Substituting the additive decomposition of the microscopic deformation gradient into Equation (2.55) shows:

$$\bar{\mathbf{F}} = \frac{1}{V} \int_{\mathcal{B}_0} \bar{\mathbf{F}} + \tilde{\mathbf{F}} dV = \bar{\mathbf{F}} + \frac{1}{V} \int_{\mathcal{B}_0} \tilde{\mathbf{F}} dV. \quad (2.62)$$

Thus, for Equation (2.59) to be valid, the volume integral of the fluctuation part must vanish,

$$\frac{1}{V} \int_{\mathcal{B}_0} \tilde{\mathbf{F}} dV = \mathbf{0}. \quad (2.63)$$

Consequently then, the following relationship must also hold:

$$\frac{1}{V} \int_{\partial \mathcal{B}_0} \tilde{\mathbf{w}} \otimes \mathbf{n} dA = \mathbf{0}. \quad (2.64)$$

It is important to note here that, in the case of large strains and rotations, not all macroscopic quantities can be obtained by volume averaging their microscopic counterparts. To illustrate this we reference Schröder [90] and consider the macroscopic right *Cauchy-Green* deformation tensor, and its definition in Equation (2.9),

$$\overline{\mathbf{C}} = \overline{\mathbf{F}}^T \overline{\mathbf{F}} = \left( \frac{1}{V} \int_{\mathcal{B}_0} \mathbf{F} dV \right)^T \left( \frac{1}{V} \int_{\mathcal{B}_0} \mathbf{F} dV \right). \quad (2.65)$$

We now consider its volume average counterpart at the micro scale and the decomposition in Equation (2.59),

$$\frac{1}{V} \int_{\mathcal{B}_0} \mathbf{C} dV = \frac{1}{V} \int_{\mathcal{B}_0} \mathbf{F}^T \mathbf{F} dV = \frac{1}{V} \int_{\mathcal{B}_0} (\overline{\mathbf{F}} + \tilde{\mathbf{F}})^T (\overline{\mathbf{F}} + \tilde{\mathbf{F}}) dV. \quad (2.66)$$

Manipulating the above leads to the expression,

$$\frac{1}{V} \int_{\mathcal{B}_0} \mathbf{C} dV = \overline{\mathbf{F}}^T \overline{\mathbf{F}} + \frac{1}{V} \int_{\mathcal{B}_0} \tilde{\mathbf{F}}^T \tilde{\mathbf{F}} dV, \quad (2.67)$$

which differs to that shown in Equation (2.65). Another microscopic quantity in this case is the *Green Lagrange* strain tensor, in Equation (2.46), which is shown to be a function of the right *Cauchy-Green* tensor and was also highlighted by Temizer and Zohdi [104].

### 2.3.2 Stress

Analogous to the macroscopic deformation gradient, we establish the macroscopic first *Piola-Kirchhoff* stress tensor as its volume average counterpart at the micro scale, when at a state of equilibrium,

$$\overline{\mathbf{P}} = \frac{1}{V} \int_{\mathcal{B}_0} \mathbf{P} dV. \quad (2.68)$$

This volume integral can also be expressed as a surface integral, using the divergence theorem,

$$\frac{1}{V} \int_{\mathcal{B}_0} \mathbf{P} dV = \frac{1}{V} \int_{\partial \mathcal{B}_0} \mathbf{t}^{(n)} \otimes \mathbf{X} dA. \quad (2.69)$$

Like the microscopic deformation gradient, the microscopic first *Piola-Kirchhoff* stress tensor can be split into a constant and fluctuation part,

$$\mathbf{P} = \overline{\mathbf{P}} + \tilde{\mathbf{P}}. \quad (2.70)$$

Evaluating this additive decomposition as a volume integral over the RVE,

$$\frac{1}{V} \int_{\mathcal{B}_0} \mathbf{P} dV = \frac{1}{V} \int_{\mathcal{B}_0} \overline{\mathbf{P}} + \tilde{\mathbf{P}} dV = \overline{\mathbf{P}} + \frac{1}{V} \int_{\mathcal{B}_0} \tilde{\mathbf{P}} dV, \quad (2.71)$$

we see that for Equation (2.68) to be valid,

$$\frac{1}{V} \int_{\mathcal{B}_0} \tilde{\mathbf{P}} dV = \mathbf{0}. \quad (2.72)$$

Using the *Cauchy* stress principle, Equation (2.48), we can also use this additive split for the traction vector,

$$\mathbf{t}^{(n)} = (\overline{\mathbf{P}} + \tilde{\mathbf{P}})\mathbf{n} = \overline{\mathbf{P}}\mathbf{n} + \tilde{\mathbf{P}}\mathbf{n}, \quad (2.73)$$

which allows for the two parts above,  $\overline{\mathbf{P}}\mathbf{n}$  and  $\tilde{\mathbf{P}}\mathbf{n}$ , to be abbreviated,

$$\mathbf{t}^{(n)} = \bar{\mathbf{t}}^{(n)} + \tilde{\mathbf{t}}^{(n)}. \quad (2.74)$$

The macroscopic first *Piola-Kirchhoff* stress tensor has previously been shown to also be a surface integral at the micro-level. By inserting the traction decomposition into Equation (2.69), the following is realized:

$$\overline{\mathbf{P}} = \frac{1}{V} \int_{\partial \mathcal{B}_0} \bar{\mathbf{t}}^{(n)} \otimes \mathbf{X} dA, \quad (2.75)$$

which inherently means that

$$\frac{1}{V} \int_{\partial \mathcal{B}_0} \tilde{\mathbf{t}}^{(n)} \otimes \mathbf{X} dA = \mathbf{0} \quad (2.76)$$

As per the kinematic measures, the equivalence between a stress measure and its volume average counterpart at the micro scale is generally not valid for all stress measures. In cases where these

equivalences have been valid, the measures were only shown to hold for specific boundary conditions [12]. The measures here are thus expressed using standard continuum mechanics and the macroscopic deformation and stress tensors above. We thus define the second *Piola-Kirchhoff* stress tensor as:

$$\bar{\mathbf{S}} = \left( \frac{1}{V} \int_{\mathcal{B}_0} \mathbf{F} dV \right)^{-1} \left( \frac{1}{V} \int_{\mathcal{B}_0} \mathbf{P} dV \right). \quad (2.77)$$

### 2.3.3 Macro-homogeneity condition

The macro-homogeneity condition requires the macroscopic stress power at a point to be equal to the volume average of the stress power at the micro level. For any kinematically admissible motion of the RVE then, the following relation must hold:

$$\bar{\mathbf{P}} \dot{\bar{\mathbf{F}}} = \frac{1}{V} \int_{\mathcal{B}_0} \mathbf{P} \dot{\mathbf{F}} dV. \quad (2.78)$$

This equality ensures the conservation of energy, enabling the scale transition of quantities, and defines the kinematic constraints at the micro-level. One of the simplest kinematic constraints is the *Voigt* or *Taylor* model, which assigns a uniform strain across the RVE,

$$\mathbf{x} = \bar{\mathbf{F}} \mathbf{X} \quad \forall \mathbf{X} \in \mathcal{B}_0. \quad (2.79)$$

The model does not require any solving as the constituents are all assumed to undergo the same deformation. Thus, the macroscopic quantities are computed directly. The *Reuss* or *Sachs* model adopts a similar approach, but instead assigns a constant stress across the RVE,

$$\mathbf{P} = \bar{\mathbf{P}} \quad \forall \mathbf{X} \in \mathcal{B}_0. \quad (2.80)$$

Additional, simplistic, procedures are required here but again does not require any detailed modeling of the microstructure. The lack of micro-structural modeling results in crude estimates of the materials overall stiffness. These approximations are overestimated for the *Voigt* model and underestimated for the *Reuss* model [41]. Although hardly suitable for modeling non-linear problems, the models are useful in quickly obtaining first estimates of the composites overall stiffness.

Other model types employ boundary conditions on the surfaces of the RVE. The most common are the *linear boundary displacement* (LBD), *uniform boundary traction* (UBT) and *periodic boundary displacement* (PBD) models. Derived from the macro-homogeneity condition, see Schröder [90], these models kinematically constrain the RVE and allow for detailed modeling of the microstructure. As a result, better estimates of the overall stiffness are attained. The *linear boundary displacement* model linearly maps the boundaries of the RVE using the macroscopic deformation gradient  $\bar{\mathbf{F}}$ ,

$$\mathbf{x} = \overline{\mathbf{F}}\mathbf{X} \quad \forall \mathbf{X} \in \partial\mathcal{B}_0. \quad (2.81)$$

By assuming the fluctuations to vanish on these surface boundaries, the boundary displacements remain homogeneous throughout the microscopic boundary value problem. In the case of the *uniform boundary traction* model, the macroscopic first *Piola-Kirchhoff* stress tensor is used to prescribe a uniform traction vector on the boundaries of the RVE,

$$\mathbf{t}_0^{(n)} = \overline{\mathbf{P}}\mathbf{n} \quad \forall \mathbf{X} \in \partial\mathcal{B}_0. \quad (2.82)$$

The model is derived such that the kinematic constraint placed on the RVE is minimal. It should be noted here that the tractions in Equation (2.82) do not complete the microscopic boundary value problem and still requires additional procedures. Like the *Voigt* and *Reuss* models, the *linear boundary displacement* and *uniform boundary traction* models yield an upper and lower bound estimate. The bounds themselves fall within the *Voigt* and *Reuss* envelope, which effectively is the upper and lower bound limits, see Kanit et al. [44]. Disparities between these limits are insignificant when considering linear elasticity, but become more apparent for problems such as plasticity [97]. The *periodic boundary displacement* model, introduced in Section 2.2.2, falls within the bounds of the *linear boundary displacement* and *uniform boundary traction* models and is the most popular.

Well suited for periodic and non-periodic microstructures [21], the *periodic boundary displacement* model provides the best estimate on the effective stiffness [107], which has shown to be exact for unit cells in periodic media [64]. It is, however, limiting when it comes to experimental tests, and that the *linear boundary displacement* model is more suited to the task [75]. Summarising the estimates of the overall stiffness, for the various constraints discussed, it follows that

$$\overline{\mathbb{A}}_{\text{Reuss}} < \overline{\mathbb{A}}_{\text{UBT}} < \overline{\mathbb{A}}_{\text{PBD}} < \overline{\mathbb{A}}_{\text{LBD}} < \overline{\mathbb{A}}_{\text{Voigt}}.$$

An alternative model to those listed above is the mixed boundary model, introduced by Hazanov and Huet [32]. Although not as effective in periodic microstructures, this model yields numerically similar estimates to the *periodic boundary displacement* model [111].

### 2.3.4 Tangent operator

As discussed at the end of Section 2.1.4, the solution to the variational formulation at the macro scale necessitates the need for a macroscopic tangent operator. This cannot be solely computed using the volume averaging methods above though, unlike the macroscopic stress tensor  $\overline{\mathbf{P}}$ , and must be calculated from the RVEs response. An expression for the tangent operator has been derived using various methods [102, 47, 17, 101, 66, 74]. In this work, we express the macroscopic tangent operator, which is derived in Schröder [90], as an additive composition of a Voigt-type bound term and a softening term,

$$\overline{\mathbb{A}} = \frac{\partial \overline{\mathbf{P}}}{\partial \overline{\mathbf{F}}} = \frac{1}{V} \int_{\mathcal{B}_0} \mathbb{A} dV - \frac{1}{V} \mathbf{L}^T \mathbf{K}^{-1} \mathbf{L}. \quad (2.83)$$

The first term in Equation (2.83) is a Voigt-type upper bound term, which is a direct volume average of the tangent operator at the micro scale. The second term is constituted as a softening part and is a consequence of the microstructural response to the prescribed macroscopic deformation. Derived from the stiffness matrix at the micro scale, the softening part is determined by condensing out the deformations associated with the discretized fluctuations. As a result, its accuracy is highly dependent on the discretization and modeling of the RVE [66] [97]. A relation between the tangent operator in the mixed,  $\bar{\mathbb{A}}$ , and reference configuration,  $\bar{\mathbb{H}}$  in Equation (2.42), can be attained using Equation (2.10) and the product and chain rule,

$$\begin{aligned}
\bar{A}_{ijkl} &= \frac{\partial \bar{P}_{ij}}{\partial \bar{F}_{kl}} = \frac{\partial (\bar{F}_{im} \bar{S}_{mj})}{\partial \bar{F}_{kl}} \\
&= \frac{\partial \bar{F}_{im}}{\partial \bar{F}_{kl}} \bar{S}_{mj} + \bar{F}_{im} \frac{\partial \bar{S}_{mj}}{\partial \bar{F}_{kl}} \\
&= \delta_{ik} \delta_{lm} \bar{S}_{mj} + \bar{F}_{im} \frac{\partial \bar{S}_{mj}}{\partial \bar{E}_{no}} \frac{\partial \bar{E}_{no}}{\partial \bar{F}_{kl}} \\
&= \delta_{ik} \bar{S}_{lj} + \bar{F}_{im} \frac{\partial \bar{S}_{mj}}{\partial \bar{E}_{no}} \frac{1}{2} (\delta_{nl} \bar{F}_{ko} + \bar{F}_{kn} \delta_{ol}) \\
&= \delta_{ik} \bar{S}_{lj} + \bar{F}_{im} \bar{H}_{mjnl} \bar{F}_{kn},
\end{aligned} \tag{2.84}$$

where  $\bar{\mathbf{F}}$  and  $\bar{\mathbf{S}}$  are computed using Equations (2.55) and (2.77). The correct computation of macroscopic tangent is a crucial step in the efficiency of the FE<sup>2</sup> method. It is important then to note the following:

- The tangent must be algorithmically consistent with the evolution of the macroscopic stress at the point on the macrostructure;
- The boundary conditions employed in computing the tangent must match those used in the computation of the stress [102];
- The tangent strongly depends on the type of boundary conditions employed [32];
- Regardless of the geometries of the microscopic boundary, the tangent must fall between the upper *Voigt* and the lower *Reuss* limits [34]; and
- Its accuracy is reliant on the mesh size, as well as the uniformity, at the micro-level [28, 104].

Details into its implementation, with respect to the chosen boundary condition, are discussed in Chapter 3.

## 2.4 Representative Volume Element

In the context of multi scale homogenization methods, an RVE is a volume element whose microstructure contains enough information to characterize the material behavior, which is



independent of surface tractions and displacements, and statistically represents the material homogeneously, at the macro level. Its proper identification is a crucial part of the homogenization process [44].

As discussed earlier, the homogenization theory makes use of the periodicity assumption. The repetition of a unit cell on a microscopic level allows one to identify an RVE that is periodic for this region. Thus the RVE can be identified as a unit cell or a group of unit cells, whose arrangement is periodic. The grouping of unit cells has been shown to be a useful approach in addressing geometric instabilities on the micro level, see Saiki et al. [85]. To satisfy the periodicity requirements when identifying an RVE, any inclusion that penetrates the boundary of the RVE must reappear on its opposite side, as shown in Figure 2.3. Gitman et al. [26] refers to this as no *wall-effects* as the RVE is thought to belong to a larger sample, which does not exist on the edge of the material. In cases where the material consists of voids, while it is possible to achieve, it is generally preferred that no voids intersect the boundaries as this makes the application of boundary conditions easier [28].

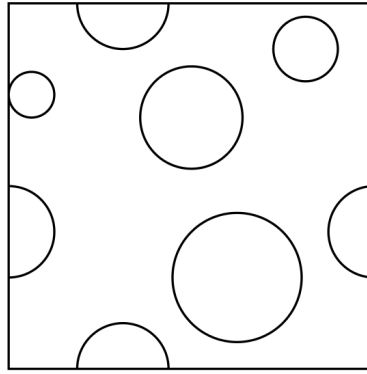


Figure 2.3: Proper identification of an RVE, in a periodic material, taken from Gitman et al. [26]: which shows any inclusion, penetrating the RVE surface, reappearing on its opposite side.

An alternative to the above is to identify the RVE as a volume element containing a sufficiently large amount of inclusions, yielding ergodic properties [75]. This approach is typically adopted when the microstructure is random, and no structural periodicity exists. Selecting a suitable scale for the RVE is a delicate task, as the scale must be sufficiently large in respect to the inclusions considered to ensure ergodicity. Conversely, the scale must be sufficiently smaller than the macrostructure to satisfy the separation of scales and justify a continuum approach on the RVE at the macro scale, discussed above. A scale dependency also exists for the RVE, as illustrated in Figure 2.4, whereby the smaller the RVE, the more dependent the overall properties are on the specified boundary conditions [42]. While the increase in RVE size leads to a convergence in the effective properties, for the respective boundary conditions, the computational resources required increases [44].

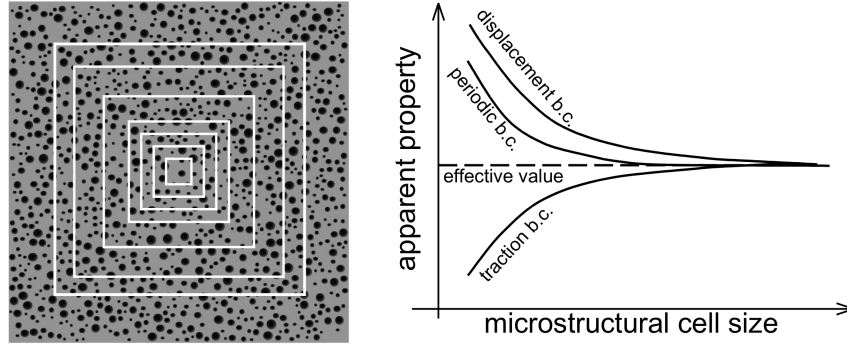


Figure 2.4: Dependency of the apparent properties of an RVE, with respect to both size and chosen boundary condition (taken from Kouznetsova et al. [48]).

The RVE size is thus dependent on the material considered and the size of its constituents, see Gitman et al. [26] for examples of different RVE sizes. Determining an appropriate scale can be done using experimental or analytical methods. In the experimental case, Romero and Masad [83] determined the scale for asphalt concrete, using image analysis, and verified the result via mechanical testing. For analytical methods, we refer to Gitman et al. [26], who developed a procedure based on the Chi-square criterion, Temizer and Zohdi [104], who used an "ensemble averaging" method, and Kanit et al. [44]. The general approach of these methods entails creating different realizations of the RVE at a fixed scale, which respectively increases until the apparent properties of the RVE remain unchanged. Although appealing, this can lead to high computational costs when dealing with complex RVEs, as a "large" scale would lead to the RVE having a high number of discretizations. In such cases, statistically similar RVEs (SSRVE) can be employed to simplify the RVEs complexity and reduce the number of discretizations. For further readings into SSRVEs, we refer to Schröder et al. [92], Balzani et al. [1], Scheunemann et al. [88]. For a more recent in-depth review in the generation of RVEs, we refer to Bargmann et al. [2].

Another requirement when identifying the RVE is that its response must be independent of the boundary condition type [84]. The scale of the RVE plays a fundamental role in this regard, as illustrated in Figure 2.4, but so does the degree of heterogeneity, such as the phase contrast or volume fraction, which can influence the magnitude in error in the macroscopic result [18]. In such cases, the size of the RVE must then be increased [75]. A practical example of this is the testing of concrete cubes for concrete structures, where the cube could be considered the RVE (with the stone, sand and cement being the inclusions) and the concrete structure being the macroscopic sample.

The result of boundary conditions, as well as the modelling of constituents, can lead to the RVE undergoing hardening or softening. These regimes of material behavior can impact the determination of an RVE. Gitman et al. [26] noted that an RVE can still be determined in the hardening regime, but its size would be significantly larger than that for linear-elasticity. Furthermore, when considering the softening regime, the localized behavior at the micro-level causes the material to lose its "representative" properties, meaning that an RVE does not exist. In cases where the sample does not qualify as an RVE, the homogenized stress does not equate to its macroscopic counterpart [101].

In this chapter, the  $FE^2$  homogenization theory and the continuum mechanics, for both the macro and micro scales, has been presented. The conservation of energy between the scales, allowed for by the macro-homogeneity condition, enables the transition of quantities between the micro and macro-scales. In the case of strain measures, the transition from the macro to the micro level is achieved using boundary conditions. These boundary conditions place the required kinematic constraint on the microscopic body, yielding a deformation driven boundary value problem. Following equilibrium at the micro scale, the microscopic quantities are then averaged across the microscopic body and transitioned to the macro scale. This volume averaging technique is done in the mixed configuration to ensure the conservation of energy between the scales. The microscopic body here is taken to be a representative volume element (RVE), and its proper identification is a crucial part of the homogenization theory. Its identification can be realised in several ways, but it must statistically represent the material homogeneously at the macro level. In the next chapter, the implementation of the  $FE^2$  model is discussed.

# Chapter 3

## FE<sup>2</sup> implementation

In the previous chapter the micro-macro continuum mechanics, which forms the basis of the FE<sup>2</sup> method, was presented. We now discuss its implementation and algorithmic treatment. The theory is implemented in the in-house C++ code SESKA, which supports finite element approximations and utilizes external libraries such as BLAS, LAPACK, ParMETIS and PETSc. A finite element framework is used to solve the boundary value problem at both scales. As previously discussed, the boundary value problem at the macro-scale is solved using a *Newton-Raphson* iteration scheme, which requires a macroscopic stress and tangent operator. The implementation of this, in a finite element framework, is straightforward and is thus not discussed. Instead, we will focus on the boundary value problem at the micro-scale and the computation of the algorithmically consistent tangent operator.

The chapter is laid out as follows. The first section discusses the boundary value problem at the micro-scale. This section is then followed by the computation of the macroscopic tangent operator. Section 3.3 describes the algorithmic treatment of the implemented FE<sup>2</sup> model, which is then evaluated in Section 3.4.

### 3.1 Microscopic boundary value problem

We consider the variational formulation in Equation (2.54), and the additive decomposition of the microscopic deformation gradient in Equation (2.59), which contains a constant and a fluctuation part. Noting this characteristic, and the relation of the fluctuation part in Equation (2.60), we rewrite the variational formulation, in index notation, as

$$\mathcal{F} = \delta \tilde{F}_{ij} \int_{\mathcal{B}_0} P_{ij} dV = \delta \tilde{w}_{i,j} \int_{\mathcal{B}_0} P_{ij} dV = 0, \quad (3.1)$$

with  $\delta \tilde{F}_{ij} = \delta \tilde{w}_{i,j}$  being the virtual counterpart to the fluctuation part  $\tilde{F}_{ij}$ . A linearized form of the above can be attained with the general linearized expression in Equation (2.36). Once again, we decompose  $\mathbf{F}$  into its respective parts and note the macroscopic part  $\bar{\mathbf{F}}$  to be given and constant. Recalling the definition introduced in Equation (2.38) then, we derive the linearized variational formulation,

$$\begin{aligned}
\mathcal{F} &= \delta \tilde{w}_{i,j} \int_{\mathcal{B}_0} P_{ij} + \delta \tilde{w}_{i,j} \frac{\partial P_{ij}}{\partial F_{kl}} \Delta F_{kl} dV \\
&= \delta \tilde{w}_{i,j} \int_{\mathcal{B}_0} P_{ij} + \delta \tilde{w}_{i,j} \frac{\partial P_{ij}}{\partial F_{kl}} (\Delta \bar{F}_{kl} + \Delta \tilde{F}_{kl}) dV \\
&= \delta \tilde{w}_{i,j} \int_{\mathcal{B}_0} P_{ij} + \delta \tilde{w}_{i,j} \frac{\partial P_{ij}}{\partial F_{kl}} \Delta \tilde{w}_{k,l} dV = 0.
\end{aligned} \tag{3.2}$$

As mentioned before, the microscopic boundary value problem is solved using standard finite element methods. We thus discretize the fluctuation field,  $\tilde{w}$ , and its gradient,  $\nabla_{\mathbf{x}} \tilde{w}$ , on a local element domain  $\mathcal{B}^e \in \mathcal{B}$  of the microstructure using the following ansatz,

$$\tilde{w}^h(\mathbf{x}) = \mathbf{N}(\mathbf{x}) \tilde{\mathbf{d}}^e \quad \rightarrow \quad \nabla_{\mathbf{x}} \tilde{w}^h(\mathbf{x}) = \mathbf{B}(\mathbf{x}) \tilde{\mathbf{d}}^e. \tag{3.3}$$

The superscript  $h$ , in the above ansatz, are approximations of the fluctuation field at the discrete nodes. The matrix  $\mathbf{N}$  is denoted as the shape functions of the nodal fluctuations,  $\tilde{\mathbf{d}}^e$ , of the finite element, while  $\mathbf{B}$  is denoted as the gradient of these shape functions. Inserting Equation (3.3) into Equation (3.2), yields the following linear equation system,

$$\mathbf{K} \Delta \tilde{\mathbf{d}} = -\mathbf{r}, \tag{3.4}$$

which is expressed as a microscopic stiffness matrix and residual vector,

$$\mathbf{K} = \mathbf{A}_{e=1}^n \int_{\mathcal{B}_0^e} \mathbf{B}^T \frac{\partial \mathbf{P}}{\partial \mathbf{F}} \mathbf{B} dV \quad \text{and} \quad \mathbf{r} = \mathbf{A}_{e=1}^n \int_{\mathcal{B}_0^e} \mathbf{B}^T \mathbf{P}, \tag{3.5}$$

respectively.  $\mathbf{A}_{e=1}^n$  denotes the standard finite element assembling operator of the microstructure, discretized by  $n$  finite elements. Solving Equation (3.4), we obtain an incremental update on the fluctuation field:

$$\tilde{\mathbf{d}}_i = \tilde{\mathbf{d}}_{i-1} + \Delta \tilde{\mathbf{d}} = \tilde{\mathbf{d}}_i - \mathbf{K}^{-1} \mathbf{r}, \tag{3.6}$$

where  $i$  is the current iteration number in the *Newton-Raphson* scheme. These iteration steps continue until the residual vector falls below the given tolerance, i.e.  $|\mathbf{r}| < \text{tol}$ , representing equilibrium at the micro level.

To implement the boundary conditions for a deformation driven boundary value problem, we recall the *Voigt*, *linear boundary displacement* and *periodic boundary displacement* models discussed in Section 2.3.3. The discrete fluctuations are prescribed using the respective boundary condition and the decomposition of the microscopic displacement vector, in Equation (2.61),

$$\begin{aligned}
(i) \quad & \text{Voigt:} \quad \tilde{\mathbf{d}} = \mathbf{0} \quad \text{in} \quad \mathcal{B}^h \\
(ii) \quad & \text{LBD:} \quad \tilde{\mathbf{d}} = \mathbf{0} \quad \text{on} \quad \partial\mathcal{B}^h; \\
(iii) \quad & \text{PBD:} \quad \tilde{\mathbf{d}}^+ = \tilde{\mathbf{d}}^- \quad \text{on} \quad \partial\mathcal{B}^h.
\end{aligned} \tag{3.7}$$

The implementation of the Voigt and Dirichlet conditions, Equation (3.7)<sub>1</sub> and Equation (3.7)<sub>2</sub>, are trivial. In this work, the periodicity constraint in Equation (3.7)<sub>3</sub> is implemented using a *strong* coupled approach. This approach couples the discrete nodes, which are directly opposite each other, enabling a dependency of one nodes fluctuation to the other. The result is a new reduced form of Equation (3.4), which is transformed using a dependency matrix. Details into its implementation, which follows that given in Kouznetsova et al. [48], have been included in Appendix A.

The approach is straightforward, but is limiting as the surfaces of the RVE must be discretized in a way that the discrete nodes are directly opposite. This provision inherently requires the number of discretizations on opposite surfaces to be exact. In cases where non-conforming meshes exist at the micro-level, the periodicity constraint can still be applied using *weakly* coupled methods. For details into these type of methods, we refer to Larsson et al. [53] and Reis and Andrade Pires [81]. For cases where enforcement of the boundary conditions are via the penalty approach, we refer to Temizer and Wriggers [102] and Gitman et al. [26].

It is important to note here that we are only solving for the fluctuation field, as, when considering Equation (2.61), the homogeneous position vector  $\bar{\mathbf{x}}$  remains unchanged throughout the boundary value problem.

## 3.2 Computation of macroscopic tangent operator

To compute the tangent operator at the macro scale, we first expand on its expression using the volume average relationship for the macroscopic first Piola-Kirchhoff stress tensor, in Equation (2.68),

$$\begin{aligned}
\bar{\mathbb{A}} &= \frac{\partial \bar{\mathbf{P}}}{\partial \bar{\mathbf{F}}} = \frac{\partial \frac{1}{V} \int_{\mathcal{B}_0} \mathbf{P}(\mathbf{F}) dV}{\partial \bar{\mathbf{F}}} \\
&= \frac{1}{V} \int_{\mathcal{B}_0} \frac{\partial \mathbf{P}(\mathbf{F})}{\partial \bar{\mathbf{F}}} dV.
\end{aligned} \tag{3.8}$$

Continuing with index notation, an expression of the derivative of the volume averaged stress tensor, with respect to the microscopic deformation gradient, is obtained using the chain rule,

$$\begin{aligned}
\bar{A}_{ijkl} &= \frac{1}{V} \int_{\mathcal{B}_0} \frac{\partial P_{ij}}{\partial \bar{F}_{kl}} dV \\
&= \frac{1}{V} \int_{\mathcal{B}_0} \frac{\partial P_{ij}}{\partial F_{rs}} \frac{\partial F_{rs}}{\partial \bar{F}_{kl}} dV.
\end{aligned} \tag{3.9}$$

The introduction of the microscopic deformation gradient,  $\mathbf{F}$ , allows for the exploitation of its additive decomposition, which includes the constant part  $\bar{\mathbf{F}}$  and yields

$$\begin{aligned}\bar{A}_{ijkl} &= \frac{1}{V} \int_{\mathcal{B}_0} \frac{\partial P_{ij}}{\partial F_{rs}} \frac{\partial(\bar{F}_{rs} + \tilde{F}_{rs})}{\partial \bar{F}_{kl}} dV \\ &= \frac{1}{V} \int_{\mathcal{B}_0} A_{ijkl} dV + \frac{1}{V} \int_{\mathcal{B}_0} A_{ijkl} \frac{\partial \tilde{F}_{rs}}{\partial \bar{F}_{kl}} dV.\end{aligned}\quad (3.10)$$

$A_{ijkl}$  is the tangent operator at the micro level, which is volume averaged in the first part of Equation (3.10) to form the so-called Voigt-type upper bound term. The second term is the crucial part and computed using the linear increment of the linearized microscopic boundary value problem, in Equation (3.2). When the microscopic boundary value problem is at a state of equilibrium,

$$\int_{\mathcal{B}_0} \delta \tilde{w}_{i,j} \frac{\partial P_{ij}}{\partial F_{kl}} \Delta F_{kl} dV = 0. \quad (3.11)$$

As per the case in Section 3.1, we substitute the additive split in Equation (2.55) into Equation (3.11),

$$\int_{\mathcal{B}_0} \delta \tilde{w}_{i,j} \frac{\partial P_{ij}}{\partial F_{kl}} \Delta \bar{F}_{kl} dV + \int_{\mathcal{B}_0} \delta \tilde{w}_{i,j} \frac{\partial P_{ij}}{\partial F_{kl}} \Delta \tilde{F}_{kl} dV = 0. \quad (3.12)$$

Discretizing the microstructure, using the same ansatz as Equation (3.3), while noting  $\Delta \bar{\mathbf{F}}$  to be given and constant at the micro level, yields

$$\mathbf{L} \Delta \bar{\mathbf{F}}^h + \mathbf{K} \Delta \tilde{\mathbf{d}} = \mathbf{0}. \quad (3.13)$$

Converse to the microscopic linear equation system, in Equation (3.4), the linear algebraic system above is expressed as two stiffness matrices,

$$\mathbf{L} = \mathbf{A} \int_{\mathcal{B}_0^e} \mathbf{B}^T \frac{\partial \mathbf{P}}{\partial \mathbf{F}} dV, \quad \text{and} \quad \mathbf{K} = \mathbf{A} \int_{\mathcal{B}_0^e} \mathbf{B}^T \frac{\partial \mathbf{P}}{\partial \mathbf{F}} \mathbf{B} dV, \quad (3.14)$$

which are assembled using the standard FEM assembling operator,  $\mathbf{A}_{e=1}^n$ . Solving for the discrete incremental fluctuation, as per the methods in Section 3.1, yields

$$\Delta \tilde{\mathbf{d}} = -\mathbf{K}^{-1} \mathbf{L} \Delta \bar{\mathbf{F}}^h. \quad (3.15)$$

Referring back to the expression of the macroscopic tangent operator, in Equation (3.10), we now discretize the equation using the same ansatz, as previously used, and the standard FEM assembling operator,

$$\bar{\mathbb{A}} = \frac{1}{V} \sum_{e=1}^n \int_{\mathcal{B}_0^e} \mathbb{A}^h dV + \frac{1}{V} \mathbf{A} \int_{\mathcal{B}_0^e} \mathbb{A}^h \mathbf{B} \frac{\partial \Delta \tilde{\mathbf{d}}}{\partial \bar{\mathbf{F}}^h} dV. \quad (3.16)$$

The first part of the equation, the Voigt upper bound term, is denoted  $\mathbb{A}^{\text{Voigt}}$ . If the microscopic tangent operator displays major symmetries, i.e.  $\mathbb{A}_{ijkl} = \mathbb{A}_{klij}$ , the stiffness matrix portion in the second part of the equation can be expressed in terms of the stiffness matrix, in Equation (3.14)<sub>1</sub>, as  $\mathbf{L}^T$ . The discrete fluctuations are now replaced with those solved in Equation (3.15),

$$\bar{\mathbb{A}} = \mathbb{A}^{\text{Voigt}} + \frac{1}{V} \mathbf{L}^T \frac{\partial \Delta \tilde{\mathbf{d}}}{\partial \bar{\mathbf{F}}^h} = \mathbb{A}^{\text{Voigt}} + \frac{1}{V} \mathbf{L}^T \frac{\partial (-\mathbf{K}^{-1} \mathbf{L} \Delta \bar{\mathbf{F}}^h)}{\partial \bar{\mathbf{F}}^h}. \quad (3.17)$$

We note here that the linear increment of the macroscopic deformation gradient is,

$$\Delta \bar{\mathbf{F}}^h = \bar{\mathbf{F}}_{i+1}^h - \bar{\mathbf{F}}_i^h, \quad (3.18)$$

giving the closed form expression of the macroscopic tangent operator:

$$\bar{\mathbb{A}} = \mathbb{A}^{\text{Voigt}} - \frac{1}{V} \mathbf{L}^T \mathbf{K}^{-1} \mathbf{L}. \quad (3.19)$$

The inversion of the microscopic stiffness matrix, in the second part, can entail substantial computational costs. This effort can be avoided, however, by identifying

$$\mathbf{L}^T \mathbf{K}^{-1} \mathbf{L} = \mathbf{L}^T \mathbb{X}, \quad \text{where} \quad \mathbb{X} = \mathbf{K}^{-1} \mathbf{L}. \quad (3.20)$$

The variable,  $\mathbb{X}$ , is a system of equations, which can be attained using LU factorization of the linear equation system,

$$\mathbf{K} \mathbb{X} = \mathbf{L}. \quad (3.21)$$

### 3.3 Algorithmic treatment

The algorithm of the FE<sup>2</sup> method, which has been implemented in this work, is now presented. Figure 3.1 gives a visual summary of this incrementally-iterative scheme. The algorithm runs as follows: First, the macroscopic boundary value problem is set up, with the selected macroscopic sample being prescribed appropriate boundary conditions and discretized accordingly. The macroscopic loads in this algorithm are applied incrementally. Each integration point in the macroscopic sample is assigned a discretized RVE, whose structure mimics that of the material at the micro level.



The local macroscopic deformation gradient,  $\bar{\mathbf{F}}$ , is computed for each integration point via the macroscopic nodal displacements. This macroscopic deformation gradient is used to prescribe the boundary conditions on the corresponding RVE. In this work, we use the periodic boundary conditions. At the initialization step, prior to the macroscopic loading, the macroscopic deformation is zero, i.e.  $\bar{\mathbf{F}} = \mathbf{I}$ . A zero deformation thus occurs across the RVE, meaning that only the computation of the macroscopic tangent operator is required.

Following the assignment of boundary conditions, the RVE boundary value problem is solved in a finite element framework, yielding a stress and strain distribution across the microstructural sample. The first *Piola-Kirchhoff* stress tensor  $\mathbf{P}$  is then averaged across the RVE and transitioned to the macro scale as a local macroscopic stress  $\bar{\mathbf{P}}$ , using Equation (2.68). From the global stiffness of the RVE, the local macroscopic tangent operator,  $\bar{\mathbb{A}}$ , is computed using Equation (3.19). The macroscopic variational formulation in this work requires the stress and tangent operator in its material form. These locally computed quantities are thus transformed using Equations (2.77) and (2.84), respectively.

This process is continued for all the macroscopic integration points, allowing for the computation of the macroscopic internal forces and stiffness matrix. Following the solution to the macroscopic equation system, incremental updates of the macroscopic nodal displacements occur, and the system checked for convergence. Should a non-converged solution be obtained, we repeat the procedure for the newly updated macroscopic nodal displacements. If the solution has reached a converged state, the next loading step is applied and the process repeated. The solution scheme is complete once all the loading steps are applied.

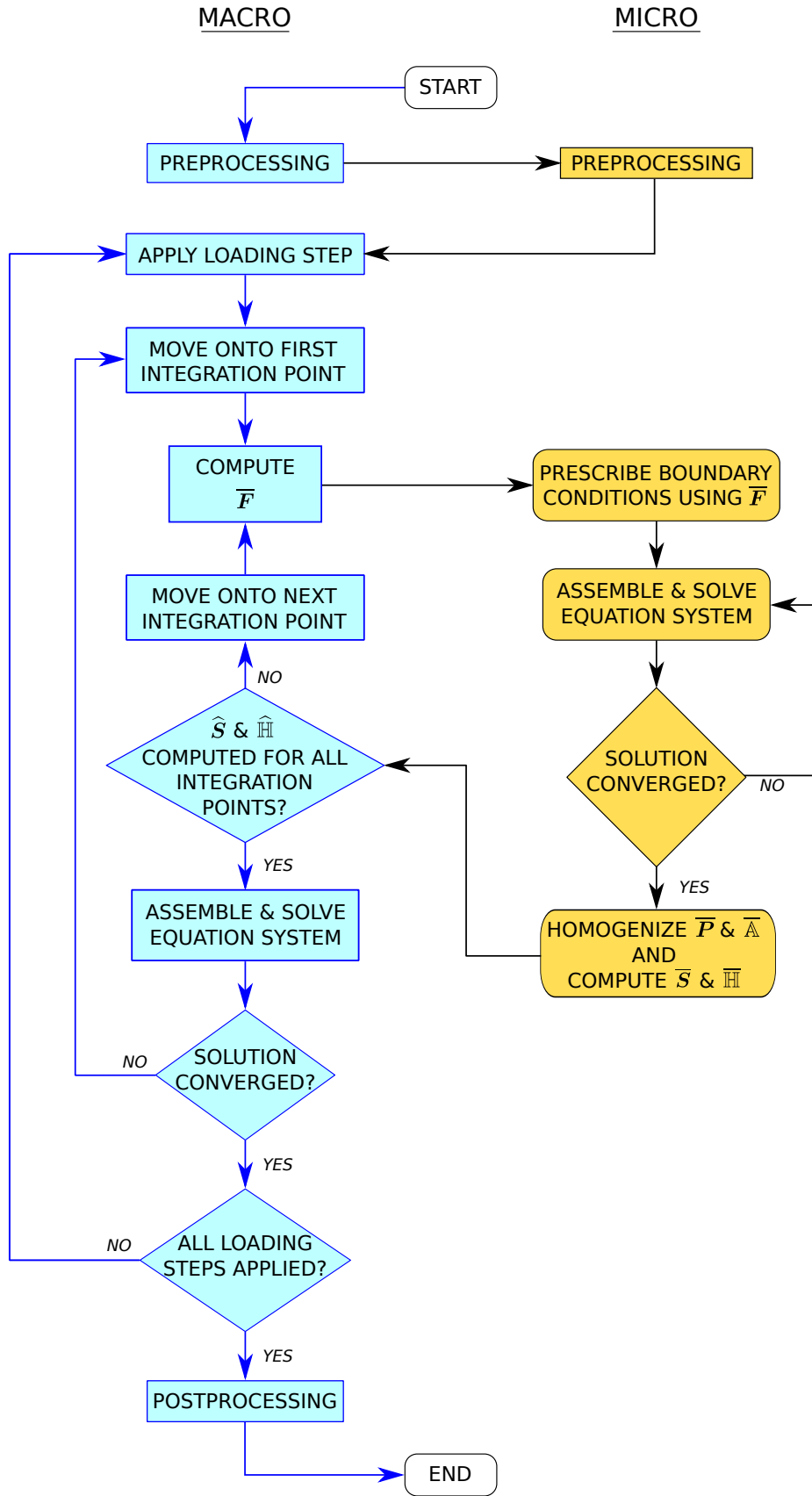


Figure 3.1: Incrementally-iterative solution scheme for the  $FE^2$  method.

### 3.4 Computational Example

In order to evaluate the presented two-scale homogenization approach, a qualitative analysis of a three-dimensional problem, presented by Otero et al. [76], is conducted and compared. The macroscopic problem entails a fixed beam with a vertically displaced loading prescribed at the mid-span. Figure 3.2 shows the geometry of the beam, with the supports and loading. Due to the beams symmetry at the mid-span, in the  $y - z$  plane, we consider only one side of the beam in our analysis and prescribe a zero displacement, in the  $x$  direction, across the entire cross-sectional face of the beam, at this point. The loading is prescribed as a line load, with a fixed displacement of  $-0.1\text{mm}$  in the  $z$  direction, along the top cross-sectional surface of the beam. The fixed support of the beam, located at the other end, is represented by prescribing a zero displacement, in all three directions.

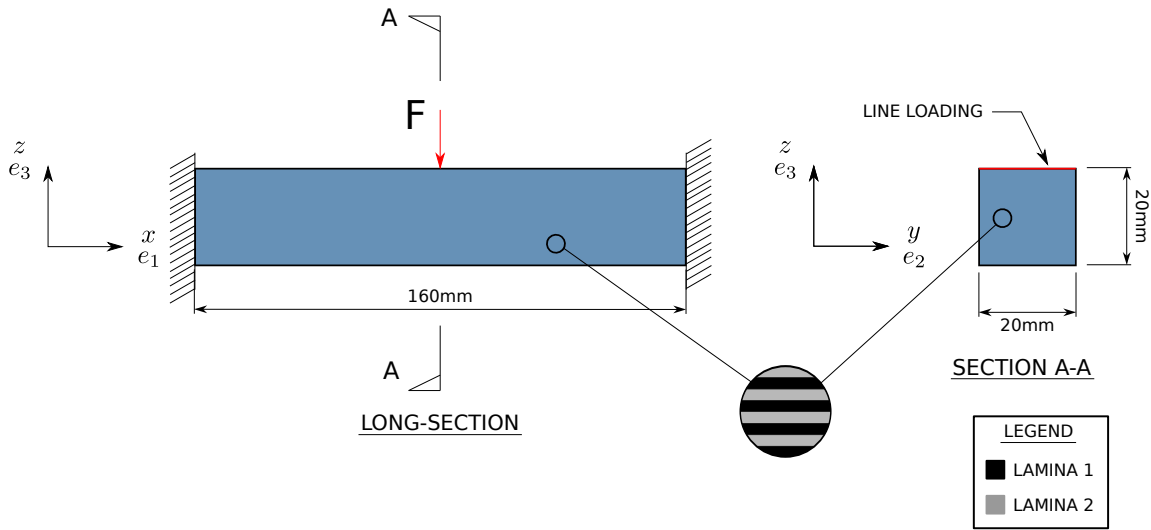


Figure 3.2: Geometry of the beam considered and its microstructure.

The beam is made of a laminated composite and consists of several layers of two materials, lamina 1 and lamina 2, which are isotropic linear elastic. The paper investigates the macroscopic effects of material degradation at the micro scale. This form of damage is analyzed by introducing a third material, lamina 3, which is a degraded form of lamina 2. Table 3.1 shows the mechanical properties of these isotropic linear elastic materials. In this table,  $E$  and  $G$  are the elastic and shear moduli, respectively, while  $\nu$  is the Poissons Ratio. The damaged material, lamina 3, shows only a reduction in the shear modulus, when compared to lamina 2, by a factor of 10.

Table 3.1: Mechanical properties of the three materials

Material	Colour	$E$ (GPa)	$G$ (GPa)	$\nu$
Lamina 1	Black	210	80.76	0.3
Lamina 2	Grey	3.5	1.46	0.2
Lamina 3	Red	3.5	0.146	0.2

The problem is solved at both scales using finite element methods, with the finite element being a first order hexahedra element. We split the problem into three parts. As previously discussed, the number of RVEs assigned at the macro scale is dependent on the number of macroscopic integration points. We thus first conduct a convergence analysis at the macro scale and the number of RVEs assigned, which for now contain material layers that are undamaged. Following this convergence analysis, we then present two cases from the paper, where the material layers are damaged. We assign periodic boundary conditions to the boundaries of the RVE, and discuss its structure in each case below. Analysis of the beams macroscopic response is carried out by computing the reaction force at the fixed support, in the  $z$  direction, using Equation (2.16),

$$\bar{\mathbf{t}}^R = \int_{\Gamma^R} \bar{\mathbf{P}} \bar{\mathbf{N}} d\Gamma = \int_{\Gamma^R} \bar{\mathbf{F}} \bar{\mathbf{S}} \bar{\mathbf{N}} d\Gamma, \quad (3.22)$$

where  $\Gamma^R$  is the surface boundary at the fixed support. The results to the two cases involving damage are qualitatively compared to those presented in the cited paper.

### 3.4.1 Convergence analysis of undamaged case

The RVE used in this example includes the materials lamina 1 and lamina 2, which are undamaged and have a 50% volume fraction respectively. We refer to the mechanical properties in Table 3.1 and present the RVE in Figure 3.3b. Due to the simplicity of the chosen material law, we discretize the RVE into eight elements.

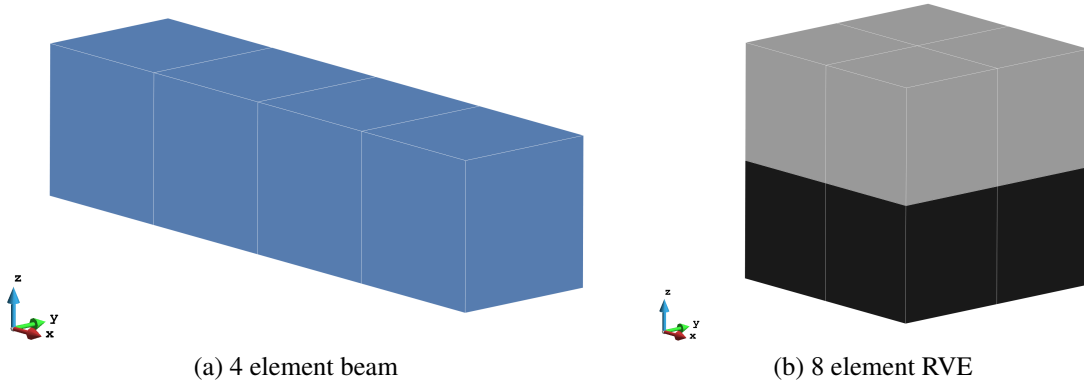


Figure 3.3: Discretized beam and RVE analyzed for the undamaged case: with the right facing cross-section of the beam assigned the displacement loading.

The convergence analysis starts with the beam discretized into four macroscopic elements, shown in Figure 3.3a. With the elements being first order, we choose second-order Gaussian quadrature to solve the macroscopic problem. This choice yields eight Gauss points per element, thus assigning 32 RVEs to the four element beam. Table 3.2 gives a breakdown of the number of discretizations considered and the number of RVEs assigned. The steep increase in RVEs with the refinement of the macroscopic mesh already indicates the high computational

demand associated with the method. As a result, we limit the number of macroscopic elements to 2048 due to computational time constraints.

Table 3.2: Discretization refinements considered at the macro scale.

Elements	Nodes	Number of RVEs assigned
4	20	32
32	81	256
256	425	2048
512	765	4096
1024	1485	8192
2048	2673	16384

Figure 3.4 shows the number of RVEs assigned and the beams reaction force in the  $z$  direction,  $\bar{t}_z^R$  in Equation (3.22), for the different mesh configurations. The results suggest that the reaction force converges to a value of approximately 800N, with a 3.5% difference between 1024 and 2048 macroscopic elements.

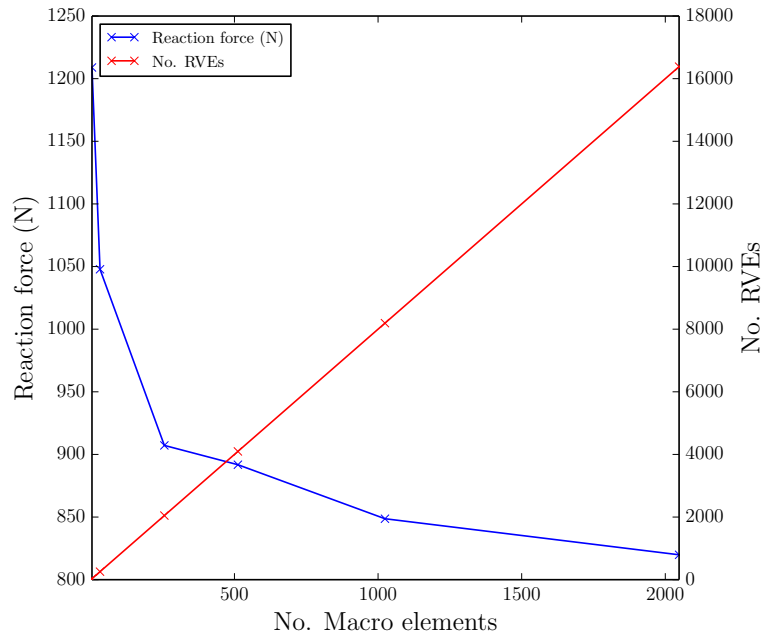


Figure 3.4: Convergence of the beams reaction force with discretizations at the macro scale: showing that while accuracy of the reaction force is increased, the number of RVEs increases, thus increasing the computational demand.

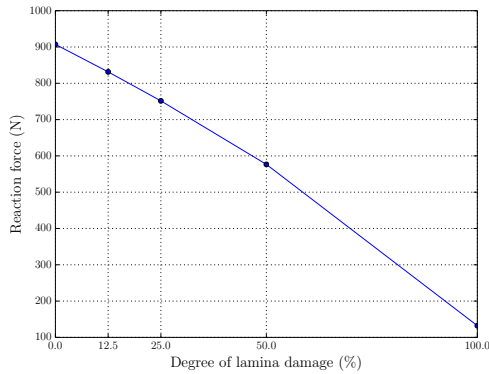
### 3.4.2 Global damaged case

To compare the results from the  $FE^2$  method to those given in the cited paper, we now consider material degradation at the micro scale. This degradation is simulated by incrementally reducing the shear modulus in the lamina 2 layers to the same value as lamina 3, over five different simulations. The shear modulus, in each simulation, is set as a percentage of the total reduction of the shear modulus between lamina 2 and lamina 3. Table 3.3 presents these values, with 0% being the undamaged case and 100% being the fully damaged case. As before, an eight element RVE is used for each simulation, with the lamina 2 material now being the degraded material. A macroscopic mesh size of 512 elements was considered due to time restraints.

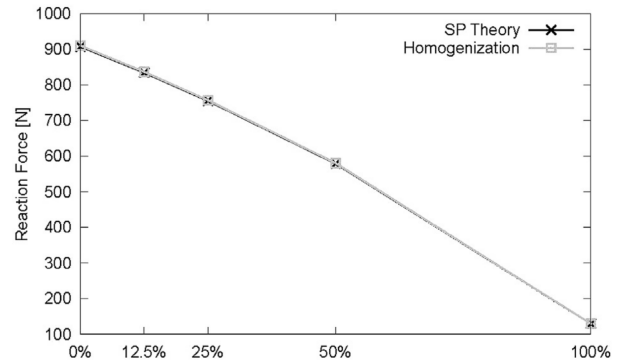
Table 3.3: Shear modulus for the stages of material degradation

Property	0%	12.5%	25%	50%	100%
$G$ (GPa)	1.46	1.295	1.131	8.03	0.146

The results in Figure 3.5a show the reaction force at the supports of the beam decreasing non-linearly as the degradation increases. These results appear to be in good agreement with those from Otero et al. [76], Figure 3.5b, who refers to this phenomena as delamination failure, in which the reduction in the shear stiffness of one material reduces the global stiffness of the structure.



(a) Implemented  $FE^2$  method



(b) Otero et al. [76]

Figure 3.5: Beams reaction force for the global damage case, showing the results to be in good agreement.

### 3.4.3 Local damaged case

The next case introduces degradation in only some of the lamina 2 layers. Similar to the previous case, the mechanical properties of these fully damaged layers match those of the lamina 3 material; however, in this case, only full material degradation is considered. Five different RVEs are used, each having a percentage of its lamina 2 layer damaged. Figure 3.6 shows four of these RVEs, with their respective percentages shown. The fifth RVE is the

undamaged case. In this example, we reduce the macroscopic mesh size to four elements. This size was chosen due to the RVE with 12% damage having 4096 microelements, which not only increases the computational time significantly but also the memory required. Considering a macroscopic mesh size higher than that specified then would lead to the computational times far exceeding that allowed.

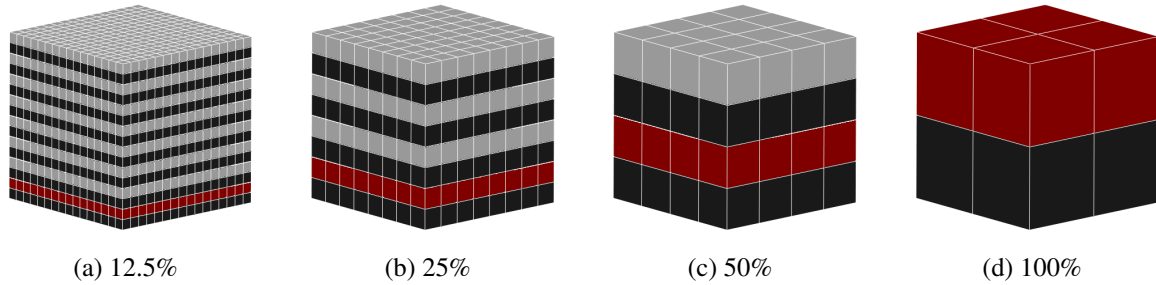
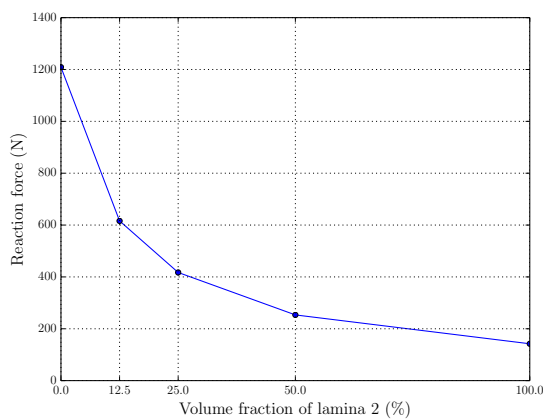
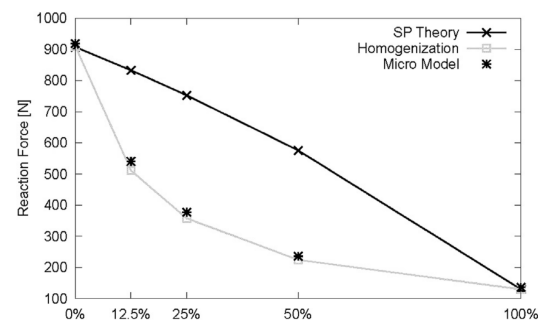


Figure 3.6: RVEs for the local damage case: where the percentage represents the portion of lamina 2 layers damaged and the number of microscopic elements being 4096, 512, 64 and 8, from left to right.

The results in Figure 3.7 indicate the stiffness of the beam to decrease more rapidly when full damage occurs in some lamina 2 layers, as opposed to the damage occurring gradually in all lamina 2 layers. Despite the size of the macroscopic mesh, which results in the higher reaction values, the implement  $FE^2$  method captures the same behavior obtained by Otero et al. [76]. The paper attributes this behavior to dislocations occurring at the micro level, which is reflected when considering the responses of the different RVEs, for the same strain state, in Figure 3.8. As shown for each RVE, the highest degrees of deformation occurs in the damaged lamina layer. This localized deformation inherently reduces the stiffness at the macro scale, resulting in the rapid decline in the reaction force observed.



(a) Implemented  $FE^2$  method



(b) Otero et al. [76]

Figure 3.7: Beams reaction force to the percentage of lamina 2 layers damaged: which shows to be in good agreement to that given by Otero et al. [76]

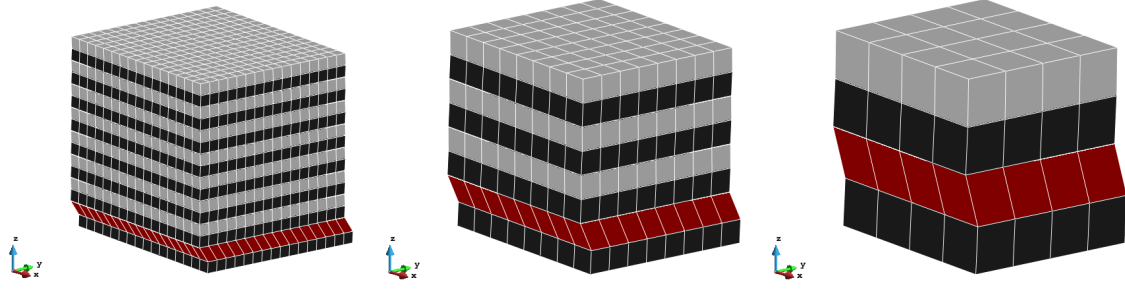


Figure 3.8: The response from the different RVEs (12.5%, 25%, 50% damage, from left to right) to the same strain showing the highest deformations occurring in the damaged layer.

A more detailed investigation into the effects of degradation, occurring locally at the macro scale, could be undertaken by assigning damaged RVEs to specified integration points. This type of analysis falls outside of the scope of this research though but could be a topic for further investigation.

In this chapter, the implementation of the  $FE^2$  method and its algorithmic treatment was discussed. It was highlighted here that only the fluctuation field is solved for at the micro scale, and that the homogeneous position vector,  $\bar{x}$  in Equation (2.61), remains unchanged. The prescription of periodic boundary conditions to the microscopic body is employed here utilizing strongly coupled means. In computing the macroscopic tangent operator, we reduce the computational effort associated with the inversion of the microscopic stiffness matrix by introducing a new variable, using LU factorization. A computational example was then presented to evaluate the  $FE^2$  model. Comparing the results to those presented in Otero et al. [76], the model was able to qualitatively replicate the effects of material degradation at the micro scale, verifying its implementation.



# Chapter 4

## Two-scale database model

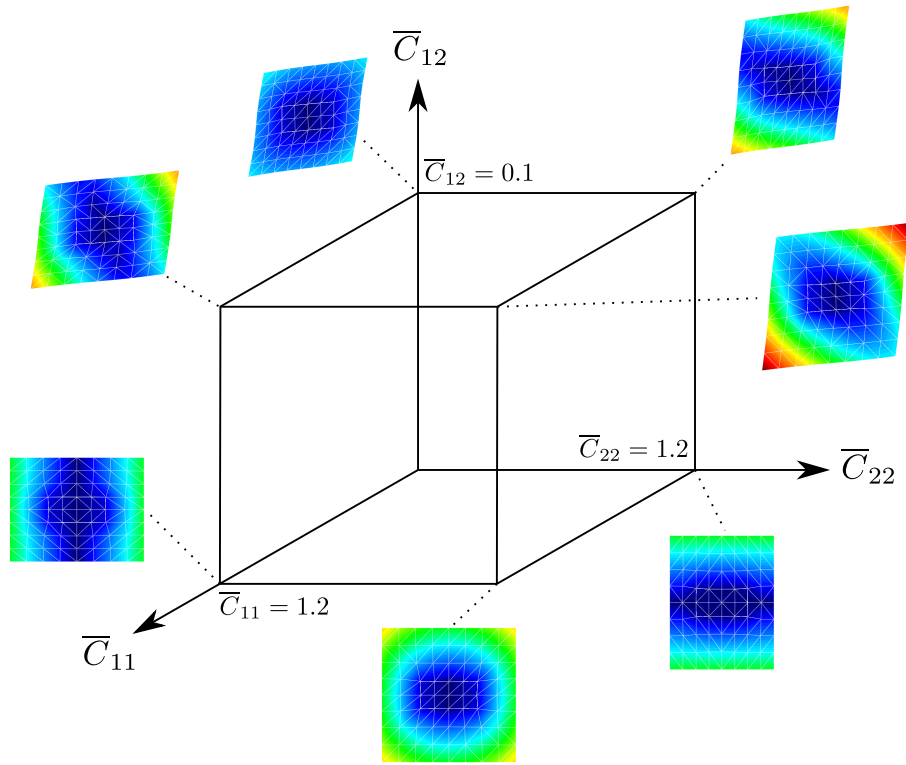
The computational example in the previous chapter demonstrated the  $FE^2$  methods ability to capture microscopic effects at the macro scale. While the characteristics of material degradation were captured, a denser macroscopic mesh was required for a more accurate solution. This need, however, would increase the number of RVEs, and profoundly impact the computational demand, if a densely meshed RVE is considered. A two-scale database (TSD) model is now presented to reduce this computational demand. Instead of obtaining the macroscopic quantities,  $\bar{\mathbf{S}}$  and  $\bar{\mathbb{H}}$ , by homogenizing the results of a microscopic boundary value problem, the quantities are now approximated using a set of precomputed RVEs. These RVEs are solved and homogenized, for a series of macroscopic strain states, in an off-line step and stored in a discretized macroscopic strain space, referred to as the *material database*. The approximations are made using the *Moving Least Squares* (MLS) approximation method.

The chapter can be broken up as follows: First, the TSD model is introduced, with its main steps highlighted. Following this introduction, the computational details of the theory are discussed. We then elaborate on the macroscopic strain space, for which the precomputed RVE results are stored. In this regard, the limits of the macroscopic strain domain and its discretization, from which the *material database* is conceived, are considered. The approximation of the stored macroscopic quantities,  $\bar{\mathbf{S}}$  and  $\bar{\mathbb{H}}$ , are then expanded on and the MLS approximation method reviewed. Finally, the chapter is concluded with the implementation of the TSD model, and its algorithmic treatment, described.

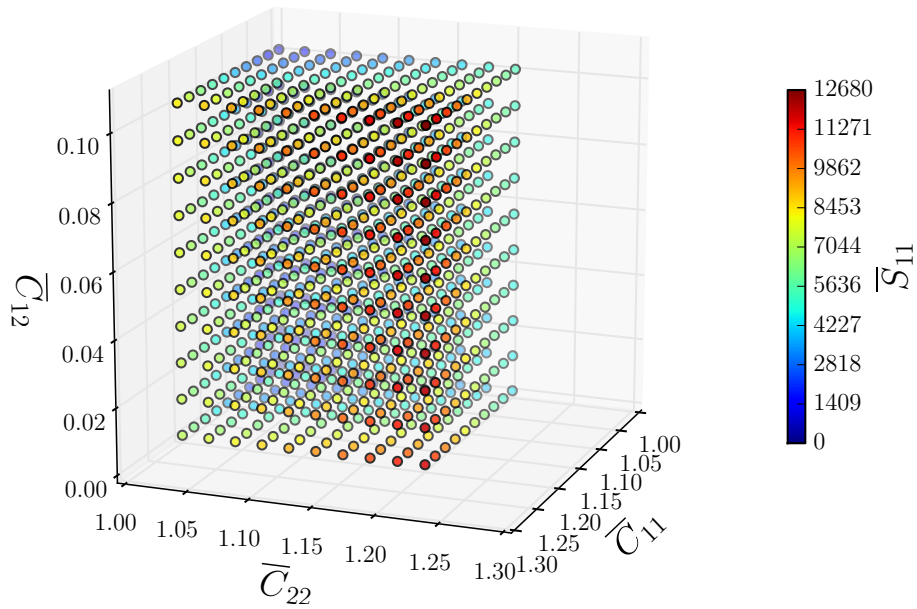
### 4.1 Introduction

As previously discussed in Section 2.1.4, the variational formulation at the macro scale requires both the macroscopic stress  $\bar{\mathbf{S}}$  and tangent operator  $\bar{\mathbb{H}}$ . The TSD model aims to compute both these macroscopic quantities by interpolating the results of an RVE in a macroscopic strain space. This space is defined by the components of the macroscopic right *Cauchy-Green deformation tensor*  $\bar{\mathbf{C}}$ , and represent the boundary conditions for the RVE. Finite element computations are conducted on the RVE, for points belonging to this space. Once the RVE has been evaluated for a point,  $\bar{\mathbf{S}}$  and  $\bar{\mathbb{H}}$  are computed and stored using Equations (2.68) and (2.77) and Equations (2.83) and (2.84), respectively. An illustration of

the macroscopic strain space, in a two-dimensional setting, with the associated RVE solutions, is provided in Figure 4.1.



(a) The deformation state of the RVE associated with a point in the strain space.



(b)  $\bar{S}_{11}$  values, stored across the discretized strain space.

Figure 4.1: Illustrations of the two-dimensional strain space, made up of components  $\bar{C}_{ij}$  for a two-dimensional problem.

Once the RVE has been computed for a sufficient number of points, and the results

homogenized and stored in the macroscopic strain space,  $\bar{\mathbf{S}}$  and  $\bar{\mathbf{H}}$  can be interpolated using suitable approximation techniques. The main steps of the approach are summarised up as follows:

1. Identification of an RVE representing the microstructure of the heterogeneous material to be modeled;
2. Definition of a strain domain,  $\Delta$ , describing the space of macroscopic right *Cauchy-Green deformation tensors*  $\bar{\mathbf{C}}$ . This is defined in a three-dimensional setting as  $\Delta \subset \mathbb{R}^6$ , and  $\Delta \subset \mathbb{R}^3$  for the two-dimensional setting.
3. Discretization of the strain domain into a finite number of particles, producing a *material database*, where each particle corresponds to a unique  $\bar{\mathbf{C}}$ . This strain measure is used to prescribe boundary conditions on the RVE. Following the solution of the RVE problem,  $\bar{\mathbf{S}}$  and  $\bar{\mathbf{H}}$  are computed and stored. This process is repeated for all particles across the discretized domain, as shown in Figure 4.1b. We shall express quantities in this database as  $(\bullet)^I$
4. Given the material database, a continuous approximation of  $\bar{\mathbf{S}}(\bar{\mathbf{C}})$  and  $\bar{\mathbf{H}}(\bar{\mathbf{C}})$  is realized using a suitable interpolation scheme. Figure 4.2 gives an illustration of this process. In this work, the Moving Least Square approximation method (MLS) is used and discussed in Section 4.4.1.

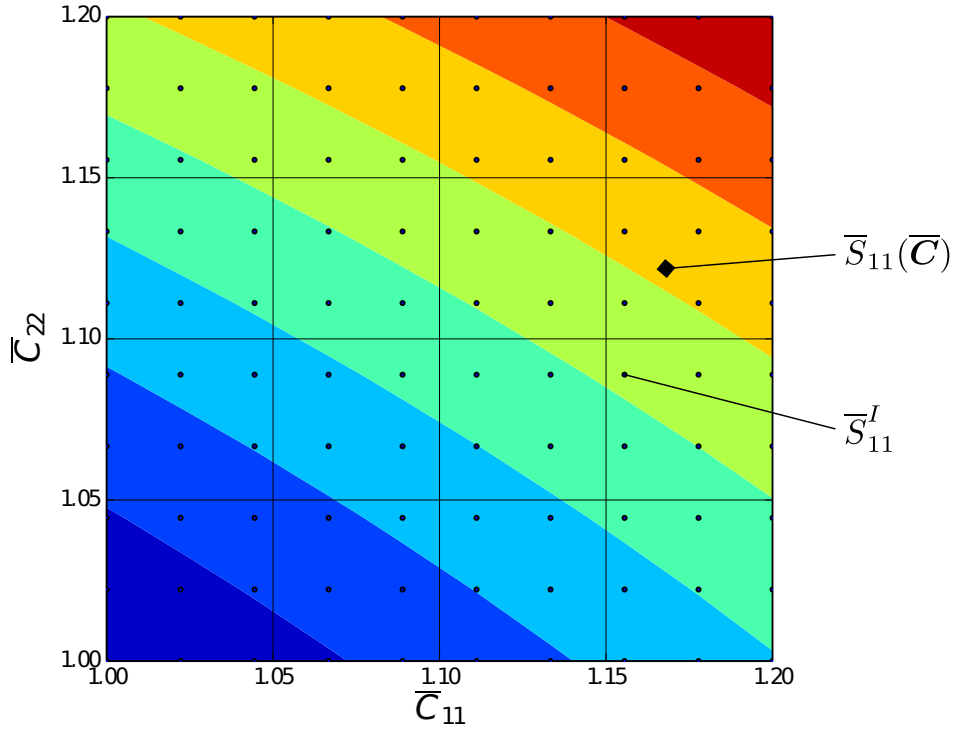


Figure 4.2: Approximation of  $\bar{S}_{11}(\bar{\mathbf{C}})$  from the stored values  $\bar{S}_{11}^I(\bar{\mathbf{C}})$  in the  $\bar{C}_{11} - \bar{C}_{22}$  plane.

## 4.2 Computational details

The  $\text{FE}^2$  method, described in Chapters 2 and 3, computes the macroscopic stress  $\bar{\mathbf{P}}$  and tangent operator  $\bar{\mathbb{A}}$  by homogenizing the structural response of an RVE, using Equations (2.68) and (2.83). To invoke this response, the macroscopic deformation gradient  $\bar{\mathbf{F}}$  is transitioned to the micro scale via the macro-homogeneity condition, discussed in Section 2.3.3. Considering that the same RVE is assigned to each macroscopic integration point,  $\bar{\mathbf{P}}$  could then be said to be a function defined over the space of macroscopic deformations  $\bar{\mathbf{F}}$ . In other words, the evaluated  $\bar{\mathbf{P}}$  is said to be a discrete representation of the function  $\bar{\mathbf{P}}(\bar{\mathbf{F}})$  at a point in the macroscopic deformation space of  $\bar{\mathbf{F}}$  tensors. Likewise,  $\bar{\mathbb{A}}$  can be evaluated at the same point, with the function

$$\bar{\mathbb{A}}(\bar{\mathbf{F}}) = \frac{\partial \bar{\mathbf{P}}(\bar{\mathbf{F}})}{\partial \bar{\mathbf{F}}}. \quad (4.1)$$

When solving for the boundary value problem at the micro level, we assume  $\bar{\mathbf{F}}$  to be constant across the RVE. The macroscopic rotation part  $\bar{\mathbf{R}}$ , see Equation (2.11), is thus said to be a rigid body rotation of the RVE. In view that both  $\bar{\mathbf{P}}$  and  $\bar{\mathbb{A}}$  are a result of the structural response within the RVE, and considering the definition in Equation (2.12), it can also be said that their discrete representations are also functions of the macroscopic right *Cauchy-Green deformation tensor*  $\bar{\mathbf{C}}$ . In the case of the *periodic boundary displacement* model, we thus rewrite the boundary condition in Equation (2.52) as:

$$\mathbf{x}^+ - \mathbf{x}^- = \bar{\mathbf{C}}^{\frac{1}{2}} (\mathbf{X}^+ - \mathbf{X}^-). \quad (4.2)$$

Transforming  $\bar{\mathbf{P}}$  and  $\bar{\mathbb{A}}$ , with Equations (2.77) and (2.84) respectively, we can obtain a discrete representation of the macroscopic stress  $\bar{\mathbf{S}}(\bar{\mathbf{C}})$  and tangent operator  $\bar{\mathbb{H}}(\bar{\mathbf{C}})$  at a point in the macroscopic strain space of  $\bar{\mathbf{C}}$  tensors. Provided that these discrete representations have been computed for a sufficient number of points, one could then expect a good approximation for the functions  $\bar{\mathbf{S}}(\bar{\mathbf{C}})$  and  $\bar{\mathbb{H}}(\bar{\mathbf{C}})$  in that space.

## 4.3 Macroscopic strain domain and its discretization

The components of  $\bar{\mathbf{C}}$  define the macroscopic strain space. To reduce the dimensions of this space, we utilize the symmetry property associated with the strain tensor and express  $\bar{\mathbf{C}}$  as a vector,

$$\bar{C}_1 = \bar{C}_{11}, \quad \bar{C}_2 = \bar{C}_{22}, \quad \bar{C}_3 = \bar{C}_{33}, \quad \bar{C}_4 = \bar{C}_{12}, \quad \bar{C}_5 = \bar{C}_{23}, \quad \bar{C}_6 = \bar{C}_{13}. \quad (4.3)$$

The strain domain  $\Delta$ , for the case of three-dimensional problems, is thus defined as:

$$\Delta \subset \mathbb{R}^6 = \Delta_1 \times \Delta_2 \times \Delta_3 \times \Delta_4 \times \Delta_5 \times \Delta_6 \quad (4.4)$$

where  $\Delta_i$  are the one-dimensional subdomains of  $\Delta \subset \mathbb{R}^6$  and correspond to  $\bar{C}_i$ , in Equation (4.3). In establishing the limits of each subdomain, for a chosen RVE, various aspects need to be considered. Firstly, the limits need to encompass all the macroscopic strains expected for a given macroscopic problem. Secondly, the limits for each subdomain must be chosen in such that it is compatible with the limits of the other subdomains. This compatibility check ensures that the generated material database is error-free when discretizing the strain domain.

Yvonnet et al. [118] suggested a practical approach in this regard. By carrying out macroscopic simulations for a series of homogeneous materials, which are the respective constituents of the microstructure, one can determine *a posteriori* the range of strain values in the structure. As pointed out though, this approach cannot guarantee that no strain point exceeds the limits of the strain domain during a simulation.

In cases where a macroscopic strain falls outside of the domain limits, Yvonnet et al. [118] proposed a technique to extrapolate the stored data out of the strain domain. This technique, however, is only applicable to cases where the stored data is one dimensional. An alternative method to handle this issue is the *adaptive homogenization strategy*, proposed by Temizer and Wriggers [101, 103]. When a macroscopic strain falls outside of the domain, the RVE problem is activated and the required quantities computed. No strategy is proposed in the present work; however, the adoption of the *adaptive homogenization strategy* above is possible and could be a topic for further investigation.

The discretization of the strain domain, into a finite number of particles, generates the material database. For the sake of simplicity, we choose the number of discretizations,  $p$ , in each subdomain  $\Delta_i$  to be the same, and their spacings between equidistant. It should be noted here that the discretizations must incorporate the prescribed lower and upper limits of each subdomain. Thus the minimum number of discretizations for each subdomain is two. We shall denote these upper and lower limits as  $\Delta_i^{\min}$  and  $\Delta_i^{\max}$ , respectively. With this in hand, the discretized set of particles in each subdomain,  $\Delta_i^e$ , can be expressed as:

$$\Delta_i^e = \{\Delta_i^{\min}, \Delta_i^2, \Delta_i^3, \Delta_i^4, \dots, \Delta_i^{p-1}, \Delta_i^{\max}\}, \quad (4.5)$$

with each discrete particle  $\Delta_i^I \in \Delta_i^e$  corresponding to a value  $\bar{C}_i$  in the macroscopic strain space of  $\bar{C}$  tensors. Using Equation (4.3), the discretized domain  $\Delta^e$  can then be said to be a set of macroscopic right *Cauchy-Green deformation tensors*  $\bar{C}$ .

The material database is now generated, using this set of tensors, by storing the homogenized structural response of the chosen RVE associated with a  $\bar{C}$ . This process, of computing  $\bar{S}$  and  $\bar{H}$ , is similar to that of a typical RVE boundary value problem described in Section 3.3 but prescribes the boundary condition using Equation (4.2).

An expression for the number of simulations required to generate the material database, for three-dimensional problems, is given by:

$$\text{number of simulations} = p^6, \quad (4.6)$$

where  $p$  is the number of discretizations in each subdomain. This exponential relationship shows that one must be mindful when considering the number of discretizations. Although the computational cost associated in generating the database may be high, this once-off process is justified by its applicability to multiple problems, which was also pointed out by Temizer and Wriggers [101].

To reduce the storage space required by the database, we exploit the symmetry property and express these stored quantities,  $\bar{\mathbf{S}}$  and  $\bar{\mathbb{H}}$ , as a vector and second-order tensor, respectively. In the case of  $\bar{\mathbf{S}}$ , we follow the same expression as that given for  $\bar{\mathbf{C}}$ ,

$$\bar{S}_1 = \bar{S}_{11}, \bar{S}_2 = \bar{S}_{22}, \bar{S}_3 = \bar{S}_{33}, \bar{S}_4 = \bar{S}_{12}, \bar{S}_5 = \bar{S}_{23}, \bar{S}_6 = \bar{S}_{13}. \quad (4.7)$$

For the fourth-order tensor,  $\bar{\mathbb{H}}$ , we utilize the expressions in Equations (4.3) and (4.7),

$$\bar{H}_{\alpha\beta} = \frac{\partial \bar{S}_\alpha}{\partial \bar{C}_\beta}, \quad (4.8)$$

with  $\alpha$  and  $\beta$  representing the vector indices of  $\bar{\mathbf{C}}$  and  $\bar{\mathbf{S}}$ , respectively.

## 4.4 Approximation of macroscopic variables

With the generation of the material database, a continuous approximation of  $\bar{\mathbf{S}}(\bar{\mathbf{C}})$  and  $\bar{\mathbb{H}}(\bar{\mathbf{C}})$  can be attained using suitable interpolation schemes. The interpolation of tensors is typically done on the tensor components, allowing for the use of common scalar interpolation methods [49]. In cases where the shape and direction information of a tensor are of importance, such an approach can introduce errors. This problem is prevalent when tracing fibres in diffusion MRI data. Under these circumstances, invariant-based tensor interpolation methods have shown to be more suitable as the interpolations are shape-preserving [39]. The stress tensor  $\bar{\mathbf{S}}$  considered here has no physical interpretation in terms of the surface tractions, meaning that interpolation of its components is permissible [38].

Similarly, difficulties in interpolating fourth-order tensors have only been realized for diffusion tensors, where again the shape and direction information are of critical importance [115]. It is thus assumed that the interpolation of tensor components for the tangent operator  $\bar{\mathbb{H}}$  is also permissible. The approximation of both stress and tangent operator values, stored in a principle strain space, has been done in previous works, see Terada and Kikuchi [105]; however, concerns arising from these quantities were never discussed.

The interpolation of variables in a precomputed database using piecewise continuous interpolation has been one such technique used to compute the approximated values [104, 101]. Yvonnet et al. [117] more recently used a multi-dimensional spline and separated variables technique to approximate variables stored in a multi-dimensional strain domain. In this research, the approximations are obtained using the Moving Least Square approximation method (MLS). This method has been used in previous database approximations and has shown to be useful in multi-dimensional problems, see Rama et al. [79].

#### 4.4.1 Moving Least Squares Approximation

The Moving Least Square approximation method (MLS) is an interpolation scheme used for multi-dimensional problems. Described by Lancaster and Salkauskas [52], the method uses a data fitting algorithm to construct an approximation function for a given a set of data points, over the prescribed domain. These data points can vary in size, making it well suited to this case. The approximation function is constructed from three components:

1. a basis function,  $P(\theta)$ , consisting of a polynomial of chosen order;
2. a set of non-constant coefficients,  $a(\theta)$ ; and
3. a weight function of compact support,  $\Phi$ , which is affiliated to each point.

The data points are not associated with spatial coordinates but with a set of parameters  $\theta$  that describes the problem's solution, such as stress or stiffness. This association means that the domain is not geometrical and can have multiple dimensions. Consider the function  $f(\theta)$  defined over a domain  $\Omega$  that is associated with a parameter set  $\theta$ . An approximation function  $f^h(\theta)$  for the above can be given by a polynomial, of order  $m$ , and a set of non-constant coefficients

$$f^h(\theta) = P(\theta) \cdot a(\theta) \quad , \text{ with } P(\theta) = [1, \theta, \theta^2, \dots, \theta^m]. \quad (4.9)$$

The domain  $\Omega$  is now discretized by a finite set of parameters  $\Theta = \{\theta^1, \dots, \theta^p\}$ . Each parameter, the so-called *particle*, within the domain  $\Omega$  is assigned a weight function  $\Phi$  of compact support. The support size of each particle  $\theta^I \in \Theta$  is determined by its so-called *influence radius*  $\varrho$  and defines the subset of particles  $\Lambda \subset \Theta$  supporting a point  $\theta$ . We shall refer to this subset of particles, supporting  $\theta$ , as the points *supporting particles*. A weighted difference between the local approximating function  $f^h(\theta)$  and the exact values of the points supporting particles can then be constructed

$$J(a(\theta)) := \sum_{I \in \Lambda} [P(\theta) \cdot a(\theta) - f(\theta^I)]^2 \Phi \left( \frac{\theta - \theta^I}{\varrho} \right). \quad (4.10)$$

The limited support of the weight function, which can be achieved by limiting the influence radius  $\varrho$  in Equation (4.10), ensures that the local behavior of the approximating function  $f^h(\theta)$  is captured. Minimizing this weighted least square fit,  $J(a(\theta))$ , with respect to  $a(\theta)$  enables the determination of the unknown coefficients  $a(\theta)$ . Substituting these coefficients into Equation (4.9), the approximating function  $f^h(\theta)$  takes the form

$$f^h(\theta) = P(\theta) \cdot M^{-1}(\theta) \sum_{I \in \Lambda} \left\{ P(\theta^I) \Phi \left( \frac{\theta - \theta^I}{\varrho} \right) f^I \right\}, \quad (4.11)$$

where  $M(\theta)$  is the *moment matrix* of the weight function  $\Phi$ ,

$$M(\theta) = \sum_{I \in \Lambda} P(\theta^I) P(\theta^I) \Phi \left( \frac{\theta - \theta^I}{\varrho} \right), \quad (4.12)$$

and  $f^I$  the *particle parameters*.

The capturing of the localized behavior in Equation (4.10) means that, with discretization refinements, the approximation  $f^h(\boldsymbol{\theta})$  converges to the exact function  $f(\boldsymbol{\theta})$  as  $\boldsymbol{\varrho} \rightarrow \mathbf{0}$ . The prerequisite number of supporting particles, for the point  $\boldsymbol{\theta}$ , is dependent on the chosen polynomial basis due to the inversion of the moment matrix  $\mathbf{M}(\boldsymbol{\theta})$ . The smoothness of the MLS approximation in Equation (4.11) is also dependent on the continuity of both the basis polynomial  $\mathbf{P} \in C^m(\Omega)$  and the weight function  $\Phi \in C^m(\Omega)$  [52]. The following holds as a result:

$$f(\boldsymbol{\theta}) \in C^k, \quad (4.13)$$

with  $k = \min(m, n)$ . In this work, we choose the weight function to be the cubic spline, given by

$$\omega(r) = \begin{cases} \frac{2}{3} - 4r^2 + 4r^3 & \text{for } |r| \leq \frac{1}{2} \\ \frac{4}{3} - 4r + 4r^2 - \frac{4}{3}r^3 & \text{for } \frac{1}{2} \leq |r| \leq 1 \\ 0 & \text{for } r \leq 1 \end{cases}, \quad (4.14)$$

where  $r$  is the normalized radius of the particle. Constructing the weight function  $\Phi$  for a three-dimensional domain, for example, would then be given as

$$\Phi\left(\frac{\boldsymbol{\theta} - \boldsymbol{\theta}^I}{\boldsymbol{\varrho}}\right) = \Phi\left(\prod_{j=1}^3 \omega\left(\frac{\theta_j - \theta_j^I}{\varrho_j}\right)\right) = \Phi\left(\prod_{j=1}^3 \omega(r_j)\right). \quad (4.15)$$

We now evaluate the effectiveness of the MLS method by approximating a function in the 1D and 2D domain, respectively. For the MLS approximation, we choose a basis polynomial of second-order, for both domains, and evaluate the approximated solution using the  $L_2$ -norm error. In the case of the 1D domain, we consider the 3<sup>rd</sup> order polynomial

$$f(x) = 10^3 - 200x + 15x^3. \quad (4.16)$$

The chosen domain ranges from -5m to 5m and is discretized into particles, evenly spaced at 1m intervals. Figure 4.3 shows the exact solution and the approximated function, which appears to be in good agreement. While the cumulative  $L_2$ -norm error across the domain was computed to be  $7.56894 \times 10^{-06}$ , its distribution, shown in Figure 4.3b, was uneven. These variations in error across the domain are due to both the number of supporting particles and their positions, with respect to the approximated point. As the approximation nears the bounds of the domain, the number of supporting particles available decreases, thus increasing the errors shown. In cases where the approximation nears a supporting particle, falling inside the domain, the MLS method is able almost to reproduce the exact value, which is a characteristic common with the method.



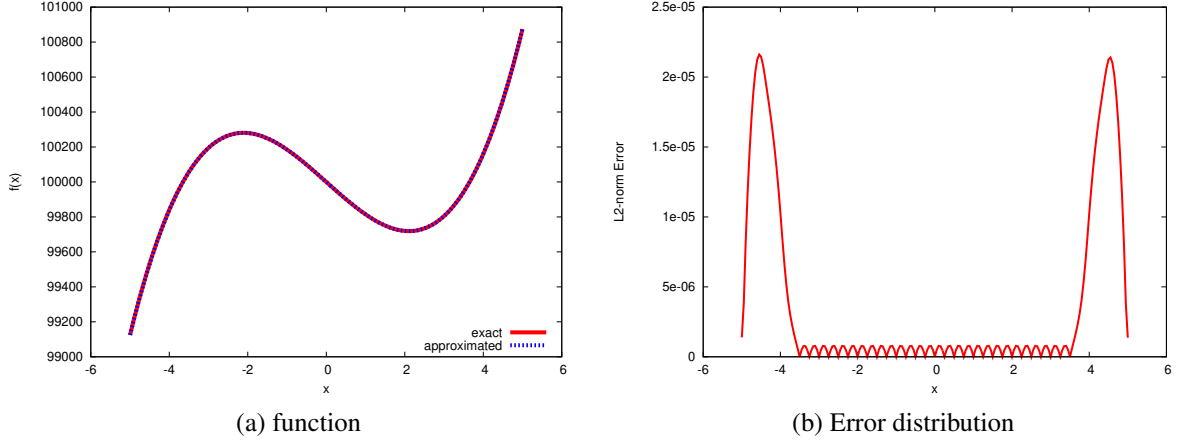


Figure 4.3: Evaluation of the approximated 1D polynomial function using the MLS method: showing the approximation function to be in good agreement with the exact solution (left) and the error distribution to be highest near the bounds of the domain (right).

The second case looks to extend the 1D example above to the 2D domain, with the function

$$f(x, y) = 10^5 - 200x - 200y + 15x^3 + 15y^3. \quad (4.17)$$

This 3<sup>rd</sup> order polynomial function is defined in a square domain ranging from -5m to 5m in both the  $x$  and  $y$  directions. Particles, discretising the domain, were evenly spaced at 1m in both directions. The cumulative  $L_2$ -norm error in this case was computed to be  $1.05549 \times 10^{-5}$ , with the error distribution illustrated in Figure 4.4. Once again the error distribution is shown to vary across the domain. Similar to the 1D case, these errors were shown to be minimal for the inner parts and highest near the bounds of the domain.

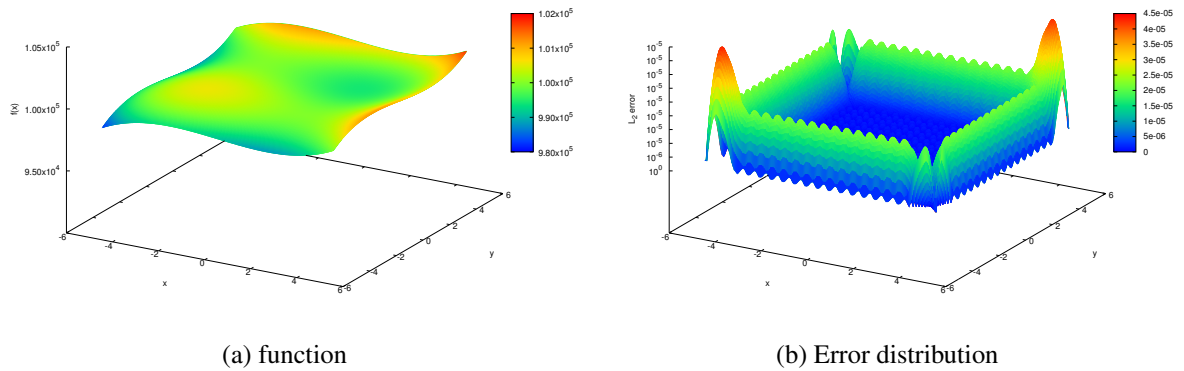


Figure 4.4: Evaluation of the approximated 2D polynomial function using the MLS method: showing the error distribution to be highest near the bounds of the domain.

The extension of the 1D function to the 2D domain shows the ability of the MLS method to be extended to multiple domains. These approximations are shown to be more accurate in the middle of the domain than the bounds.

## 4.5 Implementation and algorithmic treatment

In this section, the implementation and algorithm of the TSD model is outlined. We discuss its implementation in two parts:

1. *material database construction*, as discussed in Section 4.3; and
2. *query procedure and interpolation*, which elaborates on the approximation itself.

A workflow chart, showing the process of the method for a typical boundary value problem, is provided in Figure 4.6. The MLS approximations are carried out using the C++ code Orion, described by Rama et al. [79]. As per the FE<sup>2</sup> method, the balance equation is solved using the *Newton-Raphson* iterative solving scheme.

### Material database construction

The database is constructed using the in-house simulation software SESKA. Conventional FEM simulations of the RVE were run by prescribing the various  $\bar{\mathbf{C}}$  tensors of the discrete strain domain, using Equation (4.2). Once solved, the RVE results were homogenized and the macroscopic quantities,  $\bar{\mathbf{S}}$  and  $\bar{\mathbb{H}}$ , stored. This process was done on high-performance computers, allowing simulations to be performed in parallel.

Once all the results were obtained, the database was relocated and locally stored on a hard-drive. A basic database management system, involving a registry and a result file, was used to handle the data. The registry contains information on the database. This information includes the file location for each discrete particle  $\Delta^I$ , as well as its component values. Uploaded to Orion at the start of a problem, the registry is used in determining the subset of particles belonging to a supporting zone. The result file is a binary file and utilized to extract the stored quantities belonging to the supporting particles efficiently.

### Query procedure and interpolation

Before running the TSD model, the influence radii values  $\varrho_i$  of each subdomain  $\Delta_i$  are established. These influence radii values are used to determine the subset of particles belonging to the zone supporting  $\bar{\mathbf{C}}$ , which are used in the MLS approximation. We shall refer to this zone as the *zone of influence* and schematically represent this in Figure 4.5. The influence radii values are established by assessing the values characterizing the particles of each subdomain, see Equation (4.5).

For every  $\bar{\mathbf{C}}$  to be approximated, a preliminary assessment of the number of supporting particles is done. This ensures that the moment matrix, Equation (4.12), is invertible. In cases where the assessment returns an insufficient number of particles, the influence radius needs to be increased and the simulation restarted. Once the set of supporting particles is sufficient, the stored macroscopic quantities,  $\bar{\mathbf{S}}^I$  and  $\bar{\mathbb{H}}^I$ , associated with their supporting particle  $\Delta^I$ , are extracted and the approximated values computed.

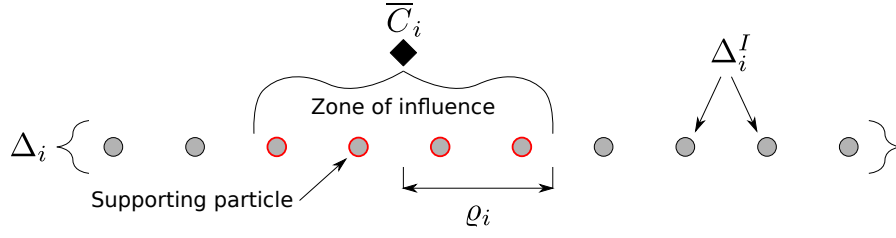


Figure 4.5: Zone of influence in the subdomain  $\Delta_i$ , for the macroscopic strain component  $\bar{C}_i$ , showing the set of supporting particles.

The algorithm can be summarised as follows, with the assumption that a database has already been created:

First, the macroscopic boundary value problem is set up in SESKA, with boundary conditions prescribed and the macroscopic structure discretized. The macroscopic loads in this algorithm are applied incrementally. During this preprocessing stage, Orion reads in the database and parameter values.

The local macroscopic right *Cauchy-Green deformation tensor* is then computed in SESKA, via the macroscopic deformation gradient, at a macroscopic integration point. This strain is then transferred to Orion. Once received, the set of particles supporting  $\bar{C}$  are determined and queried. If the set of supporting particles is sufficient, the stored macroscopic quantities,  $\bar{S}^I$  and  $\bar{H}^I$ , in each supporting particle are extracted. Using the MLS approximation method, described in Section 4.4.1, the macroscopic stress  $\bar{S}$  and tangent operator  $\bar{H}$  is then computed for  $\bar{C}$  and handed back to SESKA. This process is repeated for all the macroscopic integration points, allowing for the computation of the macroscopic internal forces and stiffness matrix.

Like the  $FE^2$  method, prior to the macroscopic loading, a zero deformation exists, i.e.  $\bar{C} = \mathbf{I}$ . While the macroscopic stress  $\bar{S}$  is known to be zero at this stage, the necessity for the tangent operator  $\bar{H}$  would still require an approximation. If a precomputed  $\bar{H}$ , for  $\bar{C} = \mathbf{I}$ , can be stored in the database, we can circumvent the need of approximating this value by directly extracting this stored quantity. This not only reduces the computational time taken to compute  $\bar{H}$ , but yields a value that is exact to one that would be obtained from the  $FE^2$  method.

Following the solution to the macroscopic equation system, incremental updates of the macroscopic nodal displacements occur, and the system checked for convergence. Should a non-converged solution be obtained, we repeat the procedure for the newly updated macroscopic nodal displacements. If the solution has reached a converged state, the next loading step is applied and the process repeated. The solution scheme is complete once all the loading steps are applied.

The TSD model offers a computationally cheaper alternative to the  $FE^2$  method by approximating the homogenized response from a set of precomputed RVEs. This alternative would enable designers to analyze the geometries and loadings on macroscopic structures, made of complex composites, with little computational effort. In the next two chapters, we assess the TSD models' performance against the  $FE^2$  method.

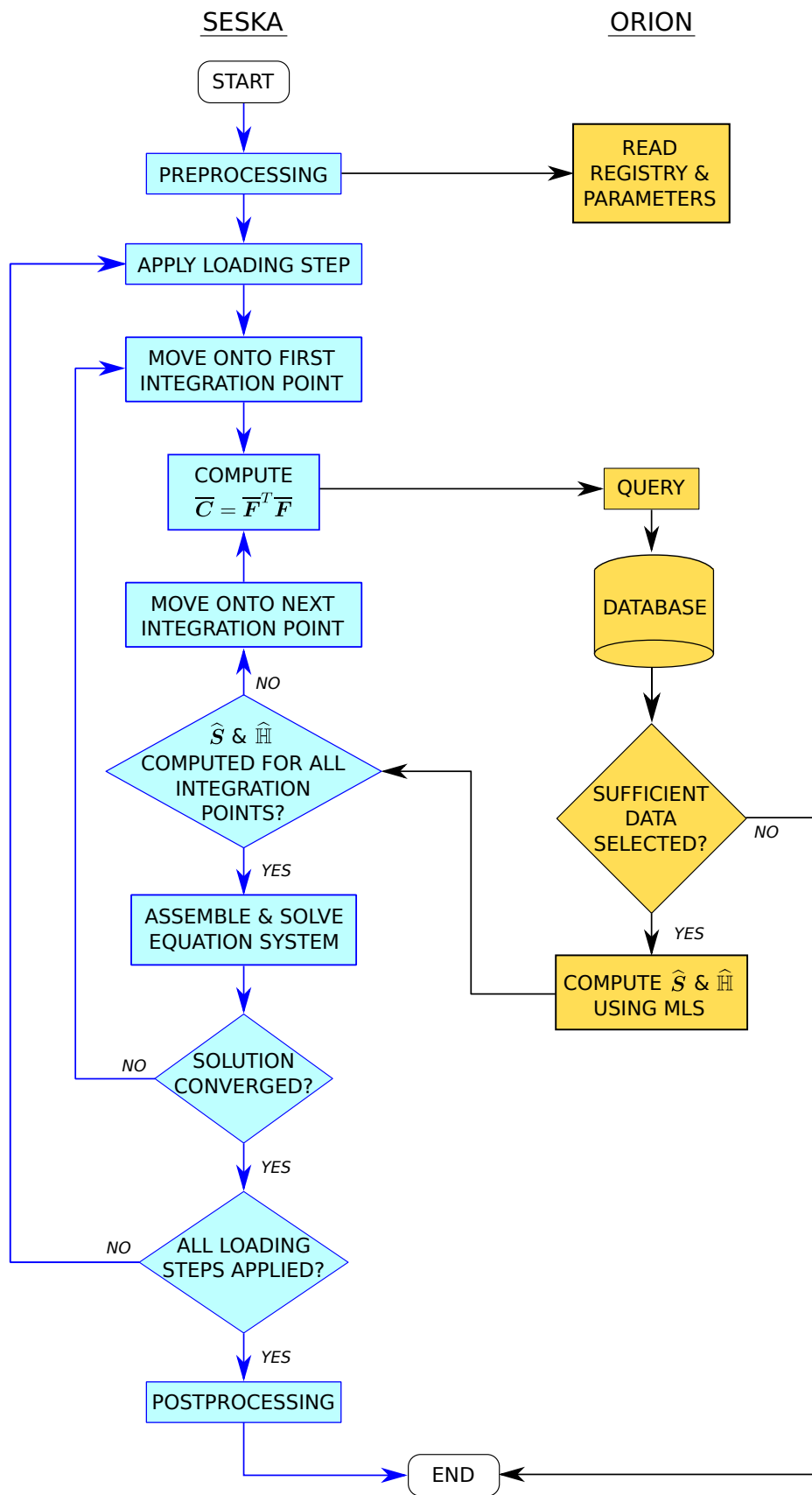


Figure 4.6: Algorithm for the TSD model model

# Chapter 5

## Numerical Analysis

The performance of the TSD model is now evaluated against the  $FE^2$  method. In this chapter, we analyze the TSD models accuracy and computational performance for a series of different macroscopic right *Cauchy-Green* strain states. Solutions to these macroscopic strain states are presented, as well as the errors of the TSD model. An RVE comprised of four layers of two different materials is considered in this analysis. To evaluate the computational performance of the TSD model, the computational time, to obtain  $\bar{\mathbf{S}}$  and  $\bar{\mathbb{H}}$ , is compared against the  $FE^2$  method.

In the sections to follow, the RVE is described, which is then analyzed, for a series of different macroscopic strain states. Following this microstructural analysis, the TSD model is then evaluated for a series of  $\bar{\mathbf{C}}$  states.

### 5.1 Micro model description

The microstructure considered is an extension of that previously discussed in Section 3.4, being a laminated composite consisting of several layers of two materials. We do not consider degradation of the material layers in this case, but instead describe the isotropic materials with a non-linear material law. The *Neo-Hookean* model, chosen here, is described by its strain energy function,

$$\Psi(\mathbf{C}) = \frac{1}{2}\lambda \ln J^2 - \mu \ln J + \frac{1}{2}\mu[\text{tr}\mathbf{C} - 3], \quad (5.1)$$

with the Second *Piola-Kirchhoff* stress given as

$$\mathbf{S} = \lambda \ln J \mathbf{C}^{-T} - \mu(\mathbf{I} - \mathbf{C}^{-T}). \quad (5.2)$$

$\lambda$  and  $\mu$  are denoted as the Lamé parameters. The chosen values for these parameters are presented in Figure 5.1, along with the chosen RVE configuration. The RVE chosen is a cube, with unit length sides, comprised of four layers. First order hexahedra elements are used to

discretize the RVE into an  $8 \times 8 \times 8$  element mesh, making up a total of 512 elements. We note here that the chosen RVE is presented to illustrate the method and should thus not be critically analyzed.

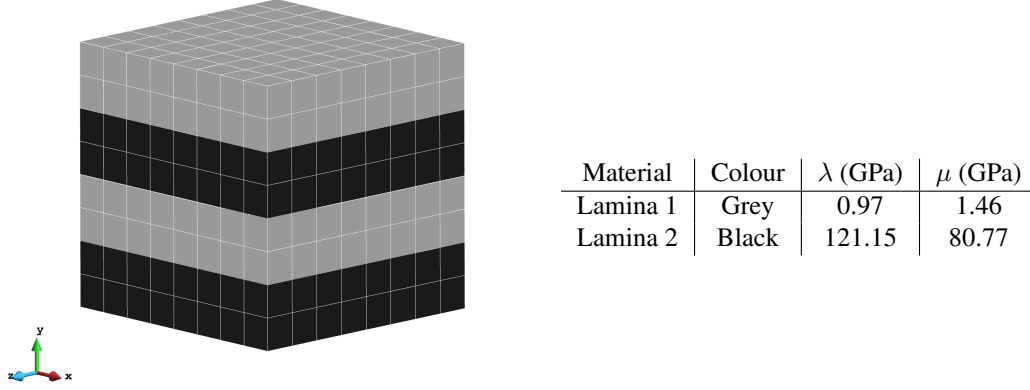


Figure 5.1: Chosen RVE and its material parameters: consisting of 4 layers of 2 non-linear isotropic materials, each described by Neo-Hookean model.

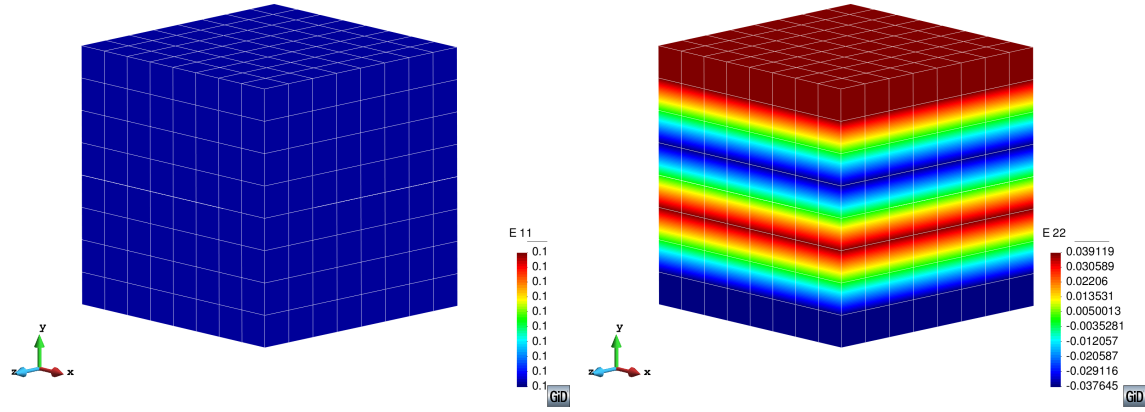
The RVE problem is solved using the *periodic boundary displacement* model, described in Section 3.1. Since the analysis is conducted for a series of different macroscopic right *Cauchy-Green* deformation states, the boundary conditions in Equation (4.2) are prescribed. In the next section, the microstructural mechanics of the RVE are investigated to gain insight into the laminated composite effects at the macro level.

## 5.2 Microstructural analysis

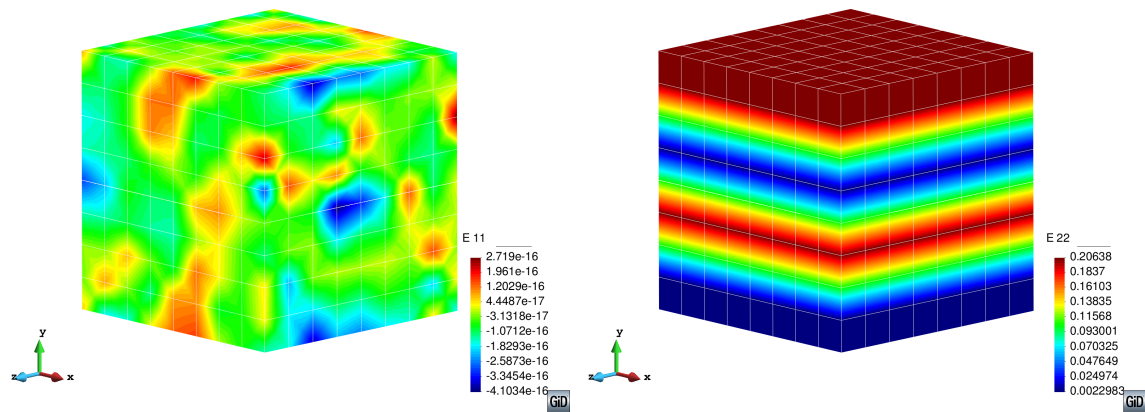
The RVEs response is analyzed for cases where only one component of  $\bar{\mathbf{C}}$  varies. Due to the axis of material symmetry, only two normal and shear components of  $\bar{\mathbf{C}}$  are considered. These components are  $\bar{C}_{11}$ ,  $\bar{C}_{22}$ ,  $\bar{C}_{12}$  and  $\bar{C}_{13}$ .

In our first analysis, we consider the macroscopic tensile strains  $\bar{C}_{11} = 1.2$  and  $\bar{C}_{22} = 1.2$ , respectively. Figure 5.2 shows the contour plots of the microscopic *Green strain* values,  $E_{11}$  and  $E_{22}$ , for these applied macroscopic strains. We compute the *Green strain* values using Equation (2.47).

The variations seen in  $E_{22}$  between the material layers, as well as the uniformities in  $E_{11}$ , for both  $\bar{C}_{11}$  and  $\bar{C}_{22}$ , indicates the RVEs response to be transversely isotropic. This effect, where the stiffness is higher in the material layer direction ( $\mathbf{e}_1$  and  $\mathbf{e}_3$ ) than its transverse direction ( $\mathbf{e}_2$ ), is a well-known characteristic of laminated composites. Gürdal et al. [29] explains this by analogously comparing the material configuration to two spring systems and their equivalences in apparent stiffness. The material layer direction would be equivalent to two springs connected in parallel, while the direction transverse to these layers would be two springs connected in series. We illustrate this comparison to the chosen RVE in Figure 5.3, with the compliant



(a)  $E_{11}$  (left) and  $E_{22}$  (right) for  $\bar{C}_{11} = 1.2$



(b)  $E_{11}$  (left) and  $E_{22}$  (right) for  $\bar{C}_{22} = 1.2$

Figure 5.2: Microscopic *Green strain* contour plots for the macroscopic normal strains,  $\bar{C}_{11}$  and  $\bar{C}_{22}$ , showing a uniform and non-uniform distribution of  $E_{11}$  and  $E_{22}$ , respectively.

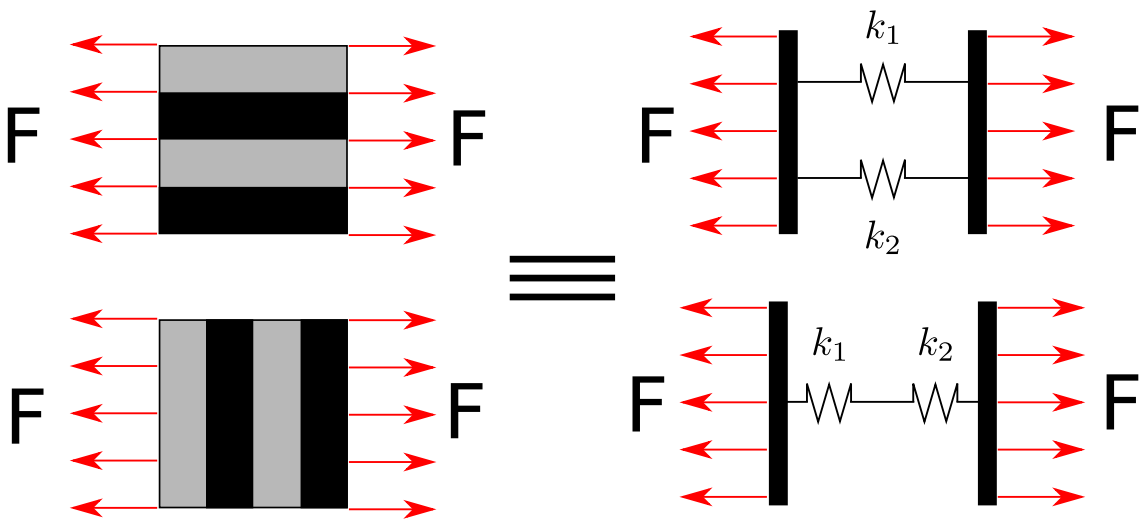


Figure 5.3: Simple analogy of the directional stiffness given by the laminated composite.

grey (Lamina 1) and stiff black (Lamina 2) material layers equivalent to springs  $k_1$  and  $k_2$ , respectively.

In the case of  $E_{22}$ , for  $\bar{C}_{11}$ , this inhomogeneous distribution is also a result of  $\bar{C}$  being prescribed across the entire surface of the RVE. Due to a zero deformation being prescribed in the  $e_2$  direction, the Lamina 1 layers stretch transversely in response to the Lamina 2 layers lateral contraction.

We now analyze the RVEs response to macroscopic shear strains, with  $\bar{C}_{12} = 0.1$  and  $\bar{C}_{31} = 0.1$ , respectively. The contour plots of the microscopic *Green strain* values,  $E_{12}$  and  $E_{31}$ , are individually shown in Figure 5.4. These microscopic strains are again a result of the RVEs configuration, with  $\bar{C}_{31}$ , which acts parallel to the material layers, yielding homogeneous  $E_{31}$  values. Due to the nature of the *periodic boundary displacement* model,  $\bar{C}_{31}$  constrains the boundaries of the RVE, thus yielding the linear deformations observed. For  $\bar{C}_{12}$ , the regions with lower  $E_{12}$  values correspond to the Lamina 2 layers, whose greater stiffness than Lamina 1 explains the higher  $E_{12}$  values.

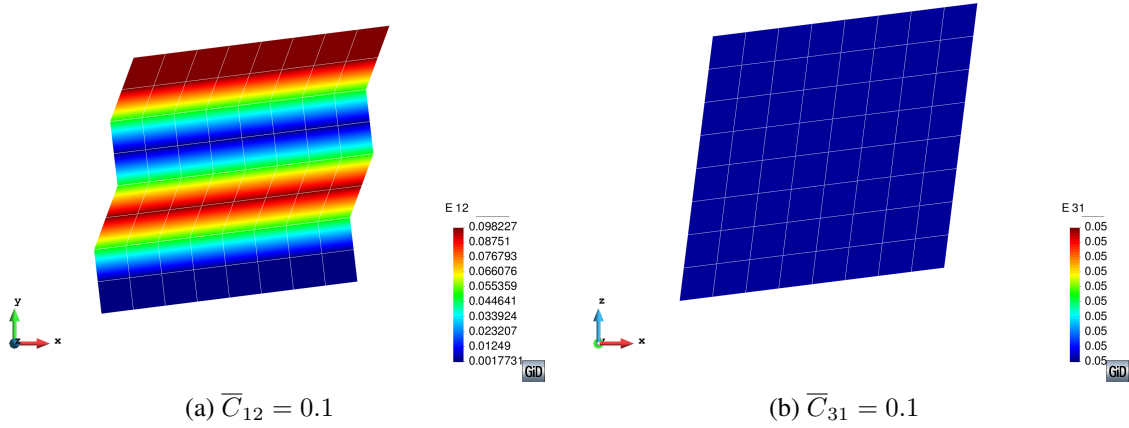


Figure 5.4: Contour plots of shear *Green strain* values,  $E_{12}$  (left) and  $E_{31}$  (right), for the macroscopic normal strains,  $\bar{C}_{12}$  and  $\bar{C}_{31}$ , respectively.

The microscopic second *Piola-Kirchhoff* stresses in the RVE, for the macroscopic strains above, are individually given in Figure 5.5. As is expected, the stresses in the RVE are higher for  $\bar{C}_{11}$  and  $\bar{C}_{31}$ . This higher stress state is owed to the strain components evoking a more significant response in the Lamina 2 layers than  $\bar{C}_{22}$  and  $\bar{C}_{12}$ , inducing the high stress concentrations shown. The homogeneous  $\bar{S}_{22}$  values, in Figure 5.5b, come as a result of the apparent stiffness given by the RVE, in the transverse direction. Analogously explained using Figure 5.3 again, the arrangement in the material layers enables the stress  $\bar{S}_{22}$  to be uniformly distributed across the RVE.

The results above revealed the RVEs response to be transversely isotropic. This response was owed mainly to the material arrangement, with components of  $\bar{C}$  coinciding with the layers yielding a stiffer response than those transverse to the layers. Furthermore, the deformations in the grey compliant material (Lamina 1) were shown to be dependent on the stiff black materials response (Lamina 2) and the periodic boundary conditions prescribed. In the section to follow,



the microscopic quantities,  $\mathbf{S}$  and  $\mathbb{H}$ , are homogenized to evaluate the TSD model, for a given  $\bar{\mathbf{C}}$ .

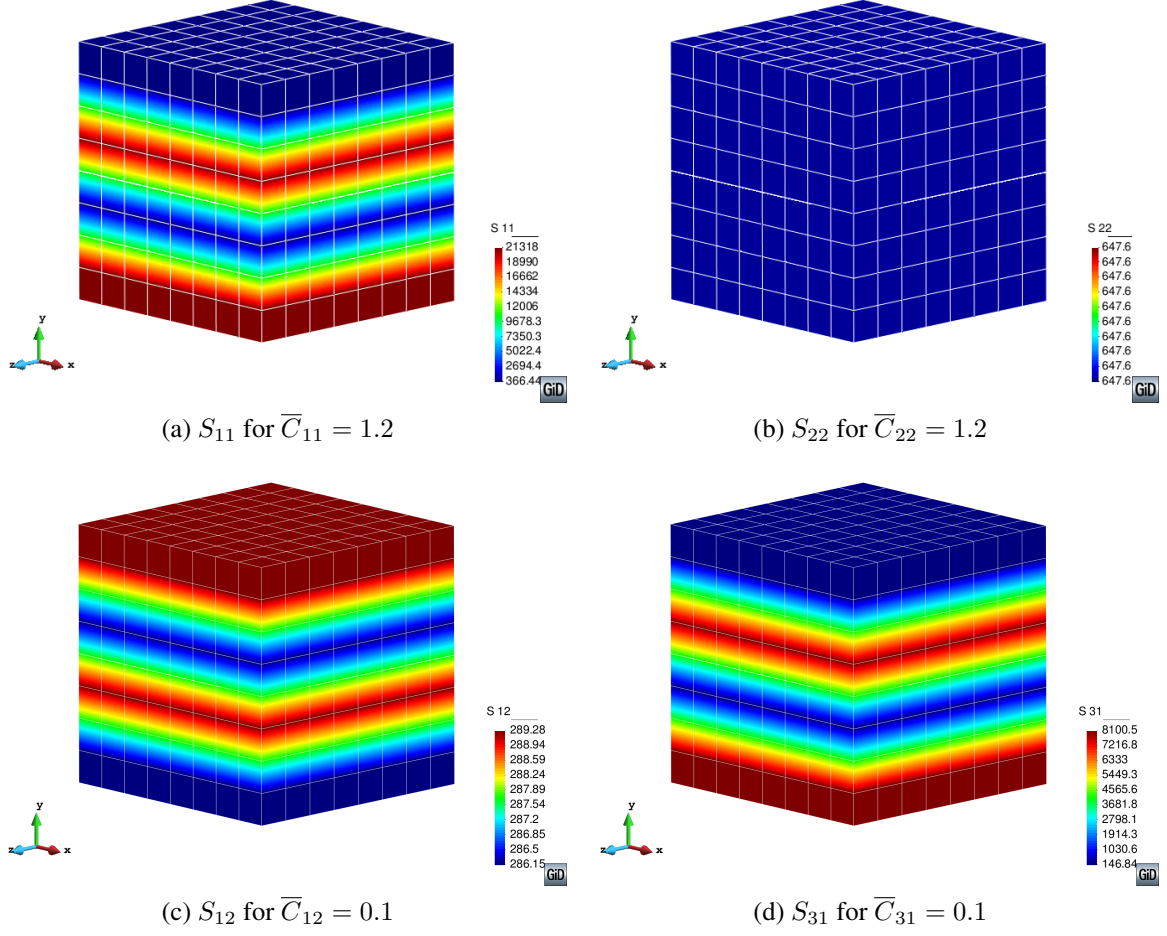


Figure 5.5: Microscopic second *Piola-Kirchhoff* stress contour plots for the various  $\bar{\mathbf{C}}$  strains.

### 5.3 Evaluation of the TSD model

The performance of the TSD model is now evaluated against the  $\text{FE}^2$  method, for a series of macroscopic right *Cauchy-Green* strain states. Solutions to these strain states are presented, as well as the errors of the TSD model. To evaluate the numerical accuracy of the TSD model, we compute the absolute and  $L_2$ -norm relative errors of each component. These error measurements are respectively computed as

$$\text{Relative Error}_i = \frac{|(\hat{\bullet})_i - (\bar{\bullet})_i|}{|(\bar{\bullet})_i|} \quad \text{and} \quad (5.3)$$

$$\text{L}_2\text{-norm} = \frac{\left( \sum_{i=1}^n \|(\hat{\bullet})_i - (\bar{\bullet})_i\|^2 \right)^{1/2}}{\left( \sum_{i=1}^n \|(\bar{\bullet})_i\|^2 \right)^{1/2}}, \quad (5.4)$$

where  $(\hat{\bullet})$  and  $(\bar{\bullet})$  denotes the component of the approximated and reference solutions, respectively, while the subscript  $i$  reflects the current macroscopic right *Cauchy-Green* strain state. We compute the approximated solutions from the TSD model using a *material database*, as outlined in Section 4.5. The  $\text{FE}^2$  solutions, which are treated as the reference solutions here, are computed using the homogenization method described in Section 2.3. An evaluation of the TSD models computational performance is then undertaken by comparing its computational time, to obtain  $\bar{\mathbf{S}}$  and  $\bar{\mathbf{H}}$ , against the  $\text{FE}^2$  method.

### 5.3.1 Material database description and MLS approximation details

To construct the database, the RVE described in Section 5.1 is used. As previously discussed, the database is characterized by the components of  $\bar{\mathbf{C}}$ . Recalling the expression in Equation (4.3), we specify the limits of each subdomain  $\Delta_i$ , of the macroscopic strain space  $\Delta$ , as

$$\begin{aligned}\Delta &= \{\Delta_1\} \times \{\Delta_2\} \times \{\Delta_3\} \times \{\Delta_4\} \times \{\Delta_5\} \times \{\Delta_6\} \\ &= \{0.7; 2\} \times \{0.7; 2\} \times \{0.7; 2\} \times \{-0.3; 0.3\} \times \{-0.3; 0.3\} \times \{-0.3; 0.3\}.\end{aligned}\quad (5.5)$$

These large stain values were chosen based on those similar to Yvonnet et al. [118]. Each subdomain is discretized into ten equidistant particles, resulting in one million macroscopic right *Cauchy-Green* deformations,  $\bar{\mathbf{C}}^I$ . We present the particle values, for each discretized subdomain, in Table 5.1.

Table 5.1: Particles of the discretized macroscopic strain space.

Subdomain	Particles in the strain domain									
$\Delta_1$	0.7	0.844	0.988	1.133	1.278	1.422	1.567	1.712	1.856	2.0
$\Delta_2$	0.7	0.844	0.988	1.133	1.278	1.422	1.567	1.712	1.856	2.0
$\Delta_3$	0.7	0.844	0.988	1.133	1.278	1.422	1.567	1.712	1.856	2.0
$\Delta_4$	-0.3	-0.234	-0.167	-0.1	-0.033	0.033	0.1	0.167	0.234	0.3
$\Delta_5$	-0.3	-0.234	-0.167	-0.1	-0.033	0.033	0.1	0.167	0.234	0.3
$\Delta_6$	-0.3	-0.234	-0.167	-0.1	-0.033	0.033	0.1	0.167	0.234	0.3

Solving and homogenizing the RVE, for each deformation tensor, in an off-line step, the macroscopic stress and tangent operator values are stored, thus creating the material database. We denote these stored quantities as  $\bar{\mathbf{S}}^I$  and  $\bar{\mathbf{H}}^I$ , respectively.

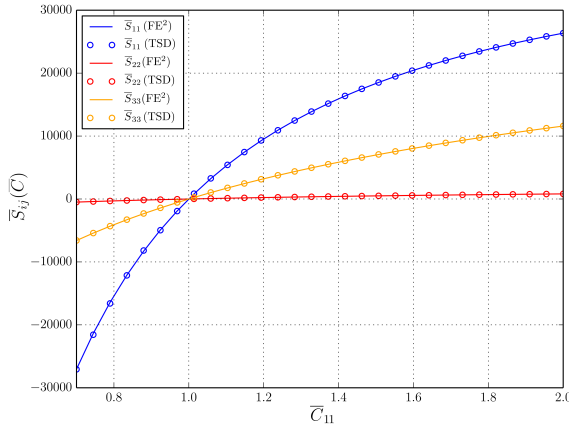
For the MLS approximation, a polynomial basis of two is chosen, with the influence radii values,  $\varrho_i$ , taken to include four particles per a subdomain. An average set of 4096  $\bar{\mathbf{C}}^I$  tensors is thus selected when approximating for a macroscopic strain. This set size can vary though, based on the locality of the approximation in the macroscopic strain space.

### 5.3.2 Macroscopic stress

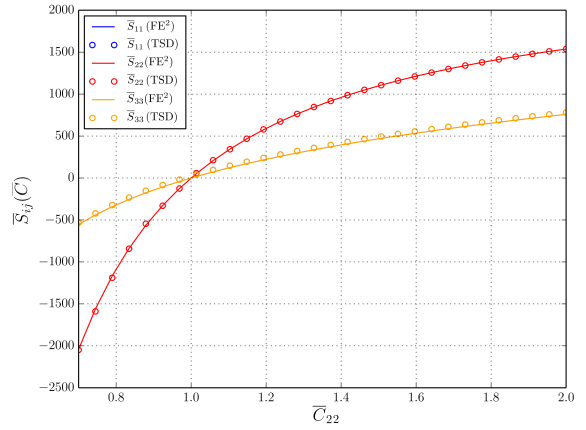
We first consider a series of macroscopic strain states, whose individual components increase linearly from a lower to an upper limit. The strain components considered, as well as their limits, are

- Normal strain components  $\bar{C}_{11}$  and  $\bar{C}_{22}$ :  $\{0.7; 2\}$
- Shear strain components  $\bar{C}_{12}$  and  $\bar{C}_{31}$ :  $\{0; 0.3\}$

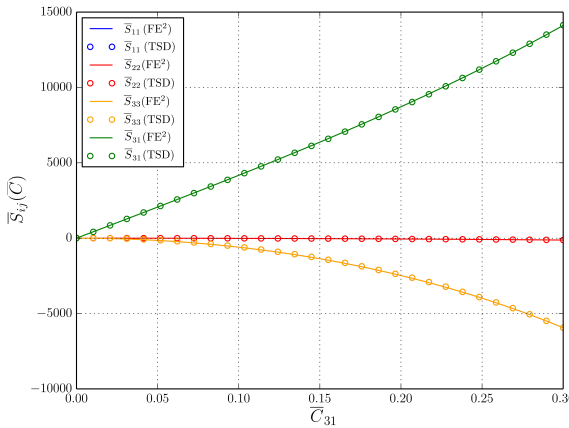
The TSD and FE<sup>2</sup> solutions, for these considered strain states, are provided in Figure 5.6. Components, whose values were considered negligible, were ignored in this case. As expected, the trends showed here follow those described in Section 5.2, with  $\bar{C}_{11}$  and  $\bar{C}_{12}$  exhibiting a higher response in the stress values. Comparing the TSD and FE<sup>2</sup> solutions, it can be seen that, for  $\bar{C}_{11}$  and  $\bar{C}_{12}$ , the approximations are in good agreement. This is not the case for  $\bar{C}_{22}$  and  $\bar{C}_{31}$  though, as slight discrepancies are observed.



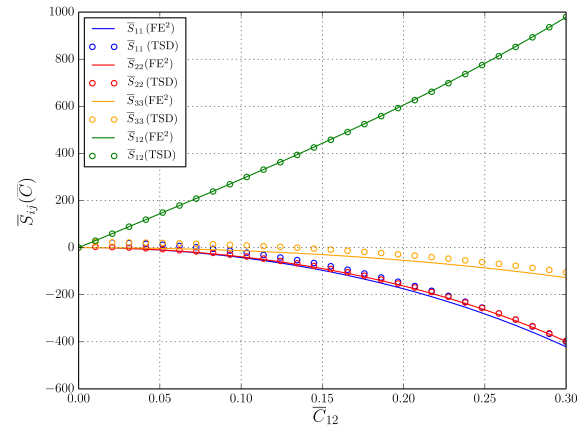
(a)  $0.7 < \bar{C}_{11} < 2$



(b)  $0.7 < \bar{C}_{22} < 2$



(c)  $0 < \bar{C}_{31} < 0.3$



(d)  $0 < \bar{C}_{12} < 0.3$

Figure 5.6: Comparison of the TSD and FE<sup>2</sup> solutions, for variations in  $\bar{C}_{ij}$ .

As shown, each strain state considered has a zero response in the stress at some point. It is thus impractical to assess the numerical accuracy using Equations (5.3) and (5.4), as the error

values would not reflect the discrepancies seen. We thus assess the accuracy by computing the absolute difference between the two solutions and present the results, with the FE<sup>2</sup> solutions, in Figure 5.7. The absolute difference in the stresses is shown to fluctuate across the various strain states. While a common characteristic of the MLS scheme, the fluctuations here become greater as the non-linearity, exhibited in the stress plots, increases. This behavior indicates the chosen polynomial basis, for the MLS approximation, to be too low, and would need to increase should a better approximation be attained. The larger values for  $|\hat{S}_{11} - \bar{S}_{11}|$  and  $|\hat{S}_{33} - \bar{S}_{33}|$ , in Figures 5.7c and 5.7d, is attributed to the locality of the approximations in the database, and the larger spacings between the particles in the subdomains  $\Delta_1$  and  $\Delta_3$ . Reducing the particle spacings in these subdomains would thus improve the approximation of  $\bar{S}_{11}$  and  $\bar{S}_{33}$ , which have shown to be more responsive to the macroscopic strain states than  $\bar{S}_{22}$ .

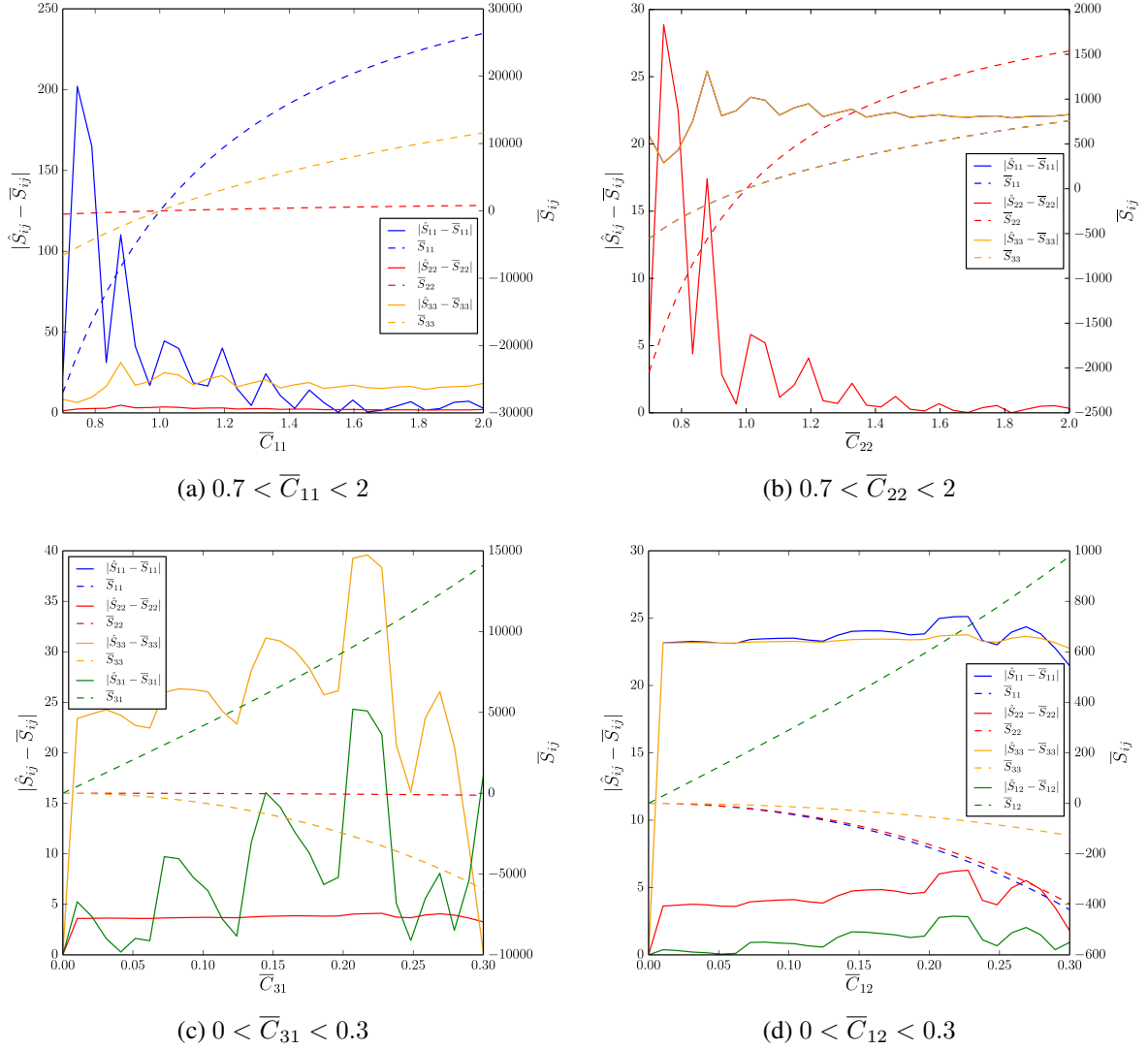


Figure 5.7: Absolute difference between the TSD and FE<sup>2</sup> solutions, which are denoted as  $\hat{S}_{ij}$  and  $\bar{S}_{ij}$ , respectively, along with the FE<sup>2</sup> solutions shown for variations in  $\bar{C}_{ij}$ .

To adequately analyze the TSD models accuracy, and evaluate its potential impact for macroscopic problems, a separate set of two hundred macroscopic strain states is considered.

The values of the first and last strain states are

$$\overline{\mathbf{C}}(1) = \begin{bmatrix} 0.7 & -0.3 & -0.3 \\ -0.3 & 0.7 & -0.3 \\ -0.3 & -0.3 & 0.7 \end{bmatrix} \quad (5.6)$$

and

$$\overline{\mathbf{C}}(200) = \begin{bmatrix} 2 & 0.3 & 0.3 \\ 0.3 & 2 & 0.3 \\ 0.3 & -0.3 & 2 \end{bmatrix}, \quad (5.7)$$

respectively, with the components of the remaining strains linearly incremented between both states of strain. Although large, the limits of this strain set were chosen to get a full evaluation of the constructed database. Only two normal and shear stress components are considered here due to the RVEs axis of material symmetry. We compute the relative error of the TSD solutions using Equation (5.3) and plot these normal and shear stress errors against the FE<sup>2</sup> solutions in Figures 5.8 and 5.9, respectively. The L<sub>2</sub>-norm relative error for each of these approximated  $\overline{\mathbf{S}}$  values, which are computed using Equation (5.4), are provided in Table 5.2.

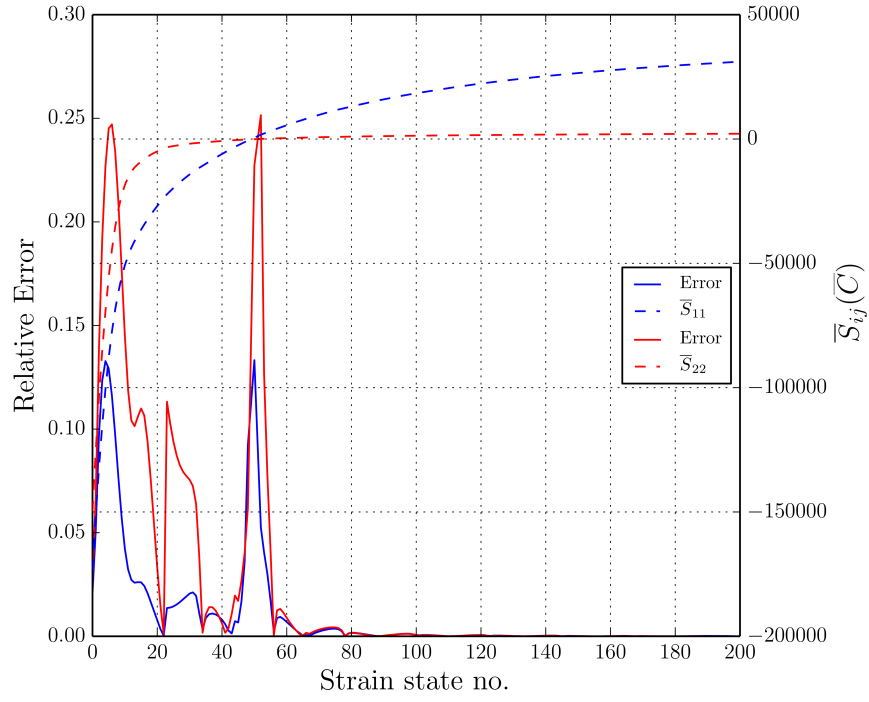
Table 5.2: L<sub>2</sub>-norm relative error values of the approximated  $\overline{\mathbf{S}}$  components.

Component	$\overline{S}_{11}$	$\overline{S}_{22}$	$\overline{S}_{12}$	$\overline{S}_{31}$
L <sub>2</sub> -norm	0.0677	0.1459	0.164	0.0985

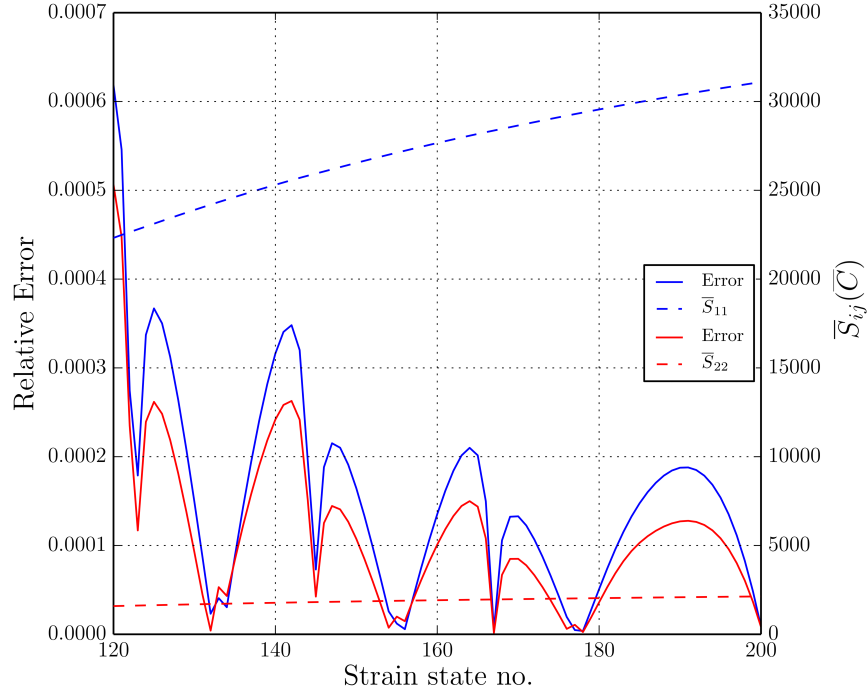
The error distributions in both the normal and shear stresses are shown to be highest in the first 40 strain states. While this is not reflected in Figure 5.8a, we note the peak, in the vicinity of  $\overline{\mathbf{C}}(50)$ , to be a result of the stress values passing through zero, and thus regard this error region negligible. This peak also exists in Figure 5.9a, near  $\overline{\mathbf{C}}(100)$ , but has a lower magnitude due to the shear stress plots here being flatter. A close correlation is once again seen between the errors and the non-linearity, exhibited by the stress plots of this region. These non-linearities are greatest in  $\overline{S}_{22}$  and  $\overline{S}_{12}$ , and explains the cumulative L<sub>2</sub>-norm errors in Table 5.2 being the highest.

While the relative errors seen in the first 40 strain states is a result of the non-linearity, shown in the stress plots, another contributor to this error is the number of supporting particles available for these approximations. As discussed in Section 4.4.1, the MLS scheme utilizes a *influence radius* to obtain the subset of particles supporting the approximation. Due to the locality of these approximations, in the macroscopic strain domain, the size of this subset is reduced, thus reducing the accuracy of the approximation.

Investigating the set of strain states, between  $\overline{\mathbf{C}}(120)$  and  $\overline{\mathbf{C}}(200)$ , in Figures 5.8b and 5.9b, reveals a fluctuation in the error distributions. These trends are similar to that shown for the MLS examples, in Section 4.4.1, and are owed to both the spacings between the supporting particles and their positions to the approximated strain state. Although the amplitudes in



(a) Results for the entire strain set  $\bar{C}(0)$  and  $\bar{C}(200)$



(b) Results for strain set  $\bar{C}(120)$  and  $\bar{C}(200)$

Figure 5.8: Relative error distribution of the macroscopic stress components  $\bar{S}_{11}$  and  $\bar{S}_{22}$  of the TSD model, plotted against the solutions of the  $FE^2$  method, for the set of macroscopic strain states, as indicated.

relative errors are significantly higher, this trend is also shown in the initial strain states,  $\overline{C}(1)$  to  $\overline{C}(40)$ . These higher amplitudes come as a result of the particles supporting this region, and the differences between their stored quantities.

### 5.3.3 Macroscopic tangent operator

We continue with the set of macroscopic strain states, discussed above, and evaluate the accuracy of the TSD models macroscopic tangent operator. The relative error distributions of  $\overline{H}_{1111}$  and  $\overline{H}_{2222}$  are presented in Figure 5.10, along with  $\overline{H}_{1212}$  and  $\overline{H}_{3131}$  in Figure 5.11. As per the stress analysis, a plot of the corresponding macroscopic tangent operator components of the  $FE^2$  solution is also included. Table 5.3 summarizes the  $L_2$ -norm relative error values of these components.

Table 5.3:  $L_2$ -norm relative error values of the approximated  $\overline{\mathbb{H}}$  components.

Component	$\overline{H}_{1111}$	$\overline{H}_{2222}$	$\overline{H}_{1212}$	$\overline{H}_{3131}$
$L_2$ -norm	0.1368	0.1467	0.1881	0.1737

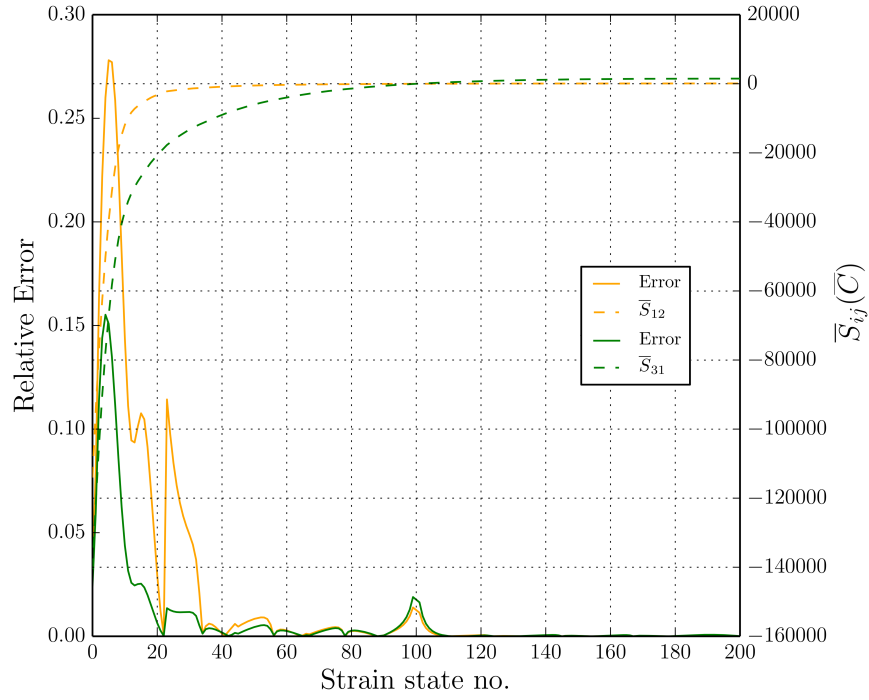
Confirming the observations made in Section 5.2, a higher apparent stiffness is seen in the components, whose directions are parallel to the RVE material layers ( $\bar{e}_1$  and  $\bar{e}_2$ ). This is not exhibited in the first few macroscopic strain sets though, with  $\overline{H}_{2222}$  being more non-linear than  $\overline{H}_{1111}$ .

The results also display the same characteristics, observed in the macroscopic stresses, with  $\overline{H}_{2222}$  and  $\overline{H}_{1212}$  having larger errors than  $\overline{H}_{1111}$  and  $\overline{H}_{3131}$ , and these errors being highest in regions where the plots of the tangent operator are non-linear. However, the magnitude of the relative errors here are higher. While this could be linked to the values in the tangent operator being larger than the stress, for the initial set of strain states,  $\overline{C}(1)$  to  $\overline{C}(40)$ , this is not the case, with Figures 5.10b and 5.11b showing the converse.

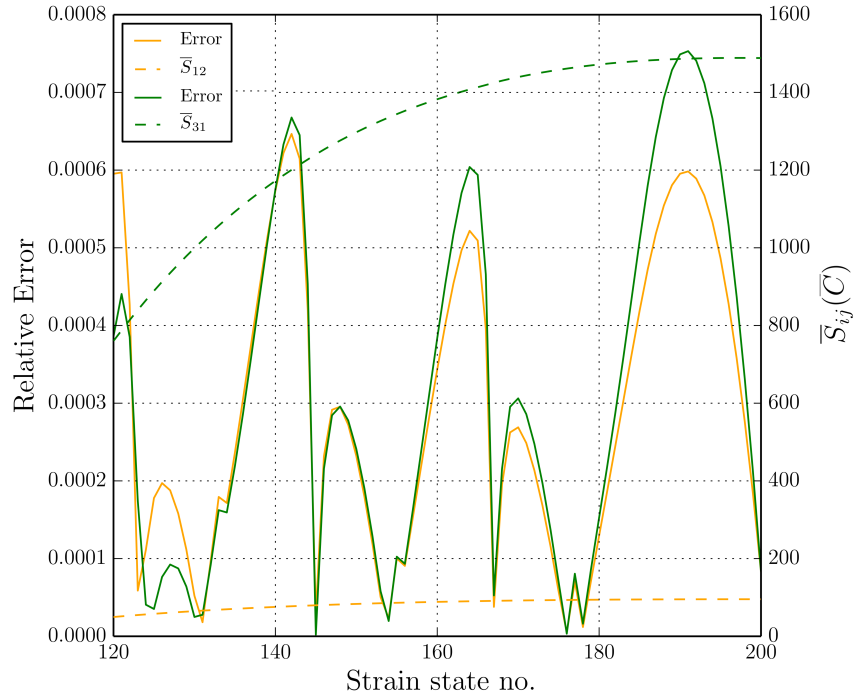
A consistent fluctuation, in each of the error distributions, is shown in Figures 5.10b and 5.11b. Unlike the stress analysis, no minor relative error peak is observed, due to the components of the tangent operator remaining above the zero value. An interesting observation here is the relative errors being larger for  $\overline{H}_{2222}$  than  $\overline{H}_{1111}$ , despite its values and non-linearity, shown over this region, being less.

Analyzing the accuracy of the TSD model, for both the macroscopic stress and tangent operator, it can be deduced that in regions where the stress and tangent operator values are more non-linear, higher inaccuracies in the approximations can be anticipated. This issue has been noted to be a common problem for these model types [118], as the models fail to capture the highly non-linear geometries accurately.

Considering that the MLS scheme only uses a basis polynomial of two, it can be seen that this order would need to be increased. This option would need to be further investigated though,



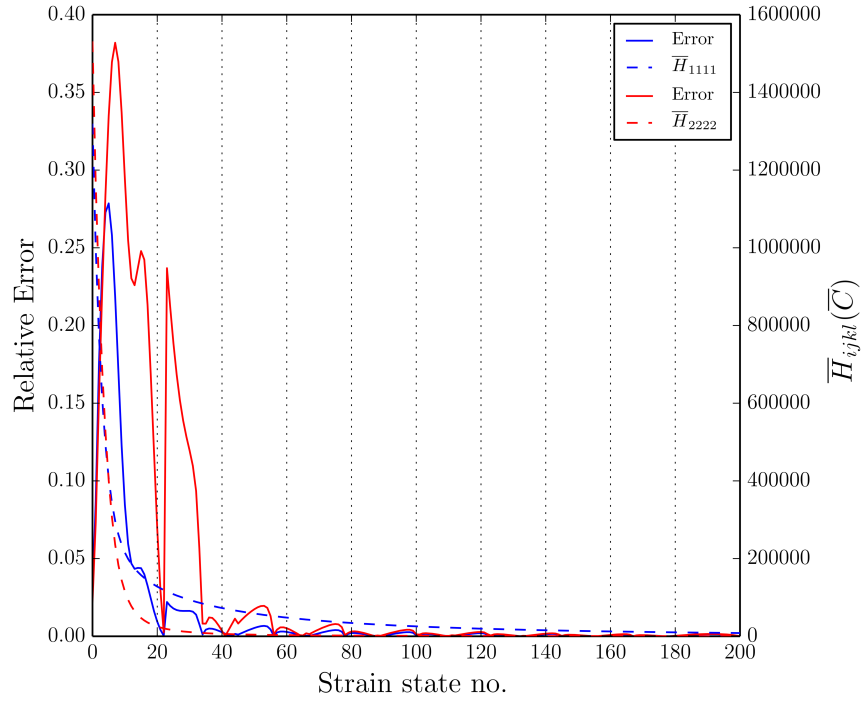
(a) Results for the entire strain set  $\bar{C}(0)$  and  $\bar{C}(200)$



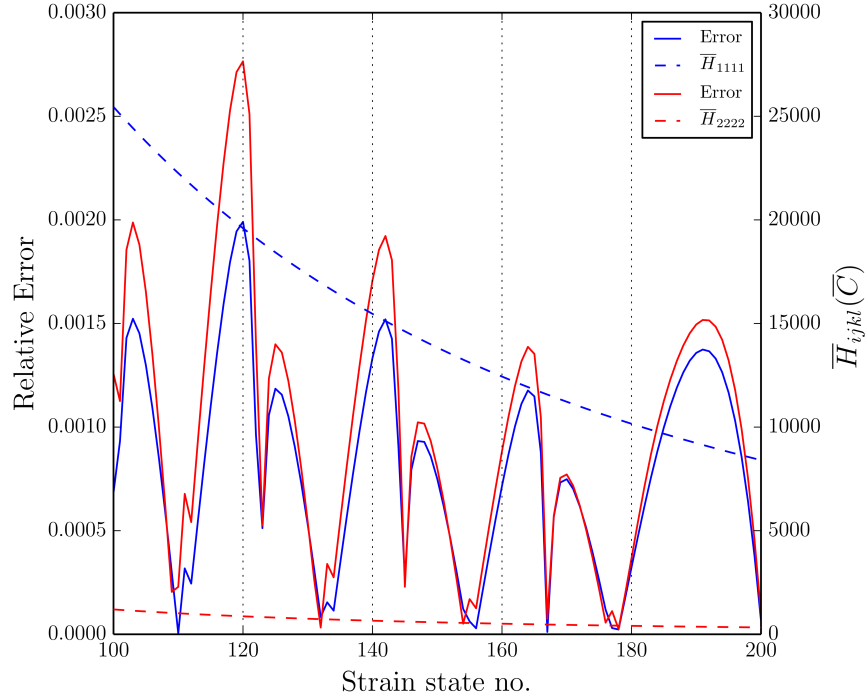
(b) Results for strain set  $\bar{C}(120)$  and  $\bar{C}(200)$

Figure 5.9: Relative error distribution of the macroscopic stress components  $\bar{S}_{12}$  and  $\bar{S}_{31}$  of the TSD model, plotted against the solutions of the  $FE^2$  method, for the set of macroscopic strain states, as indicated.



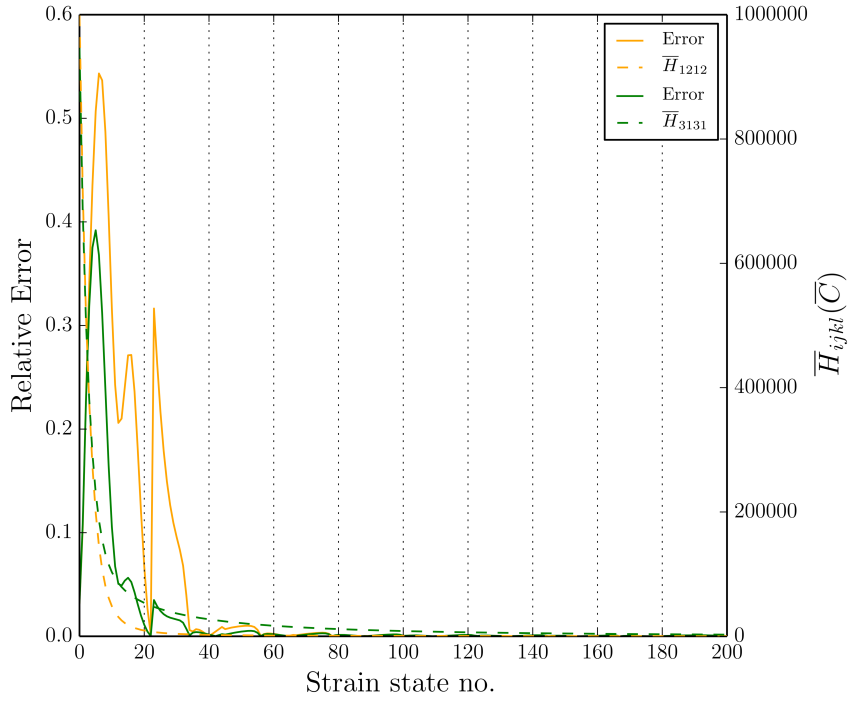


(a) Results for the entire strain set  $\bar{C}(0)$  and  $\bar{C}(200)$

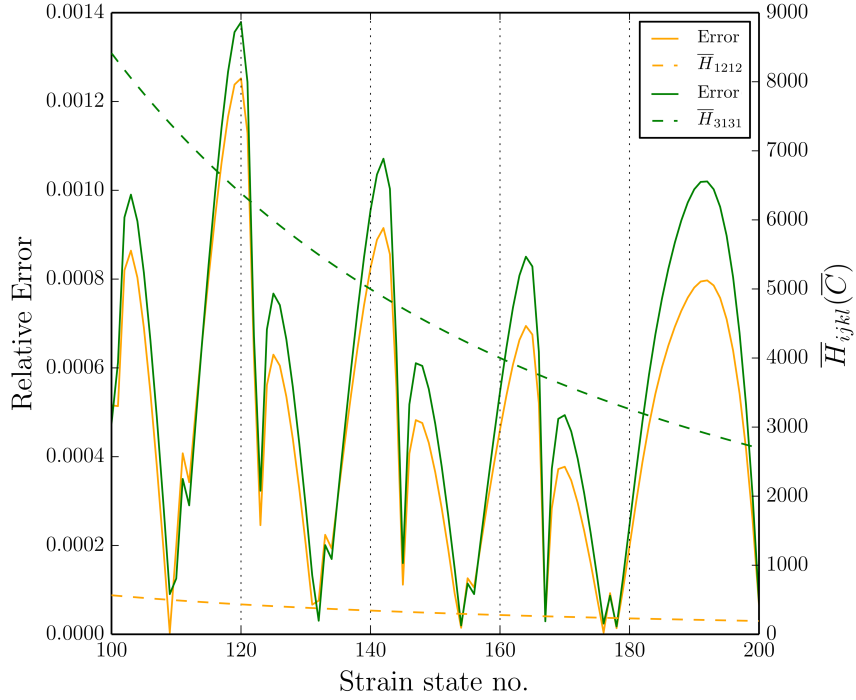


(b) Results for strain set  $\bar{C}(100)$  and  $\bar{C}(200)$

Figure 5.10: Relative error distribution of the macroscopic tangent operator components  $\bar{H}_{1212}$  and  $\bar{H}_{3131}$  of the TSD model, plotted against the solutions of the  $FE^2$  method, for the set of macroscopic strain states, as indicated.



(a) Results for the entire strain set  $\bar{C}(0)$  and  $\bar{C}(200)$



(b) Results for the strain set  $\bar{C}(100)$  and  $\bar{C}(200)$

Figure 5.11: Relative error distribution of the macroscopic tangent operator components  $\bar{H}_{1212}$  and  $\bar{H}_{3131}$  of the TSD model, plotted against the solutions of the  $FE^2$  method, for the set of macroscopic strain states, as indicated.

as the increase in the polynomial basis could require a larger set of supporting particles to approximate the strain, thus increasing the computational effort. Furthermore, its effect on approximating strain states near the limits of the macroscopic strain domain would also need to be considered, as the number of supporting particles available here is reduced.

An additional remedy is increasing the number of discretizations, in regions where  $\bar{\mathbf{S}}$  and  $\bar{\mathbf{H}}$  are non-linear. While this would improve on the accuracy of the approximations, the computational effort required to generate the database would increase. A more feasible option here would be to strategically discretize the macroscopic strain domain, with the number of discretizations increasing in regions exhibiting high non-linearity.

### 5.3.4 Computational time

In our final assessment, we analyze the computational performance of the TSD model. This analysis is conducted using the same set of macroscopic strain states, as per the previous analysis, and comparing the computational times of the TSD model and conventional  $\text{FE}^2$  method. The computational times taken, to obtain  $\bar{\mathbf{S}}$  and  $\bar{\mathbf{H}}$ , for each strain state, are plotted in Figure 5.12. As shown, the TSD model is significantly faster than the  $\text{FE}^2$  method, averaging 0.91 and 21.03 seconds, respectively.

For the initial strain states, an increase in the computational time of the  $\text{FE}^2$  method was observed. This increase could be associated to the RVE nearing incompressibility. The TSD model here however, shows a decline in computational time. This decline is owed to the locality of the approximations in the macroscopic strain domain, and the number of supporting particles available, which is evident when considering the computational times decrease at both ends of the strain set.

The results in the TSD model are seen to be significantly advantageous, as the computational time in computing  $\bar{\mathbf{S}}$  and  $\bar{\mathbf{H}}$  is only limited by the number of supporting particles in the MLS approximation. Furthermore, in the case of the conventional  $\text{FE}^2$  method, the computational times of the method can only increase with the complexities of the RVE. This limitation is only applicable to the TSD model when constructing the database.

A severe drawback of the TSD model, however, is the accuracy. Owed to both the locality of the approximations (in the macroscopic strain domain) and the regions of non-linearity (exhibited by both  $\bar{\mathbf{S}}$  and  $\bar{\mathbf{H}}$ ) improvements to the TSD model could be obtained by increasing the basis polynomial of MLS scheme and strategically discretizing the macroscopic strain space. An error sensitivity analysis would need to be undertaken in this regard though, and could be a topic for future research. In the next chapter, we continue with this analysis via a macroscopic boundary value problem.

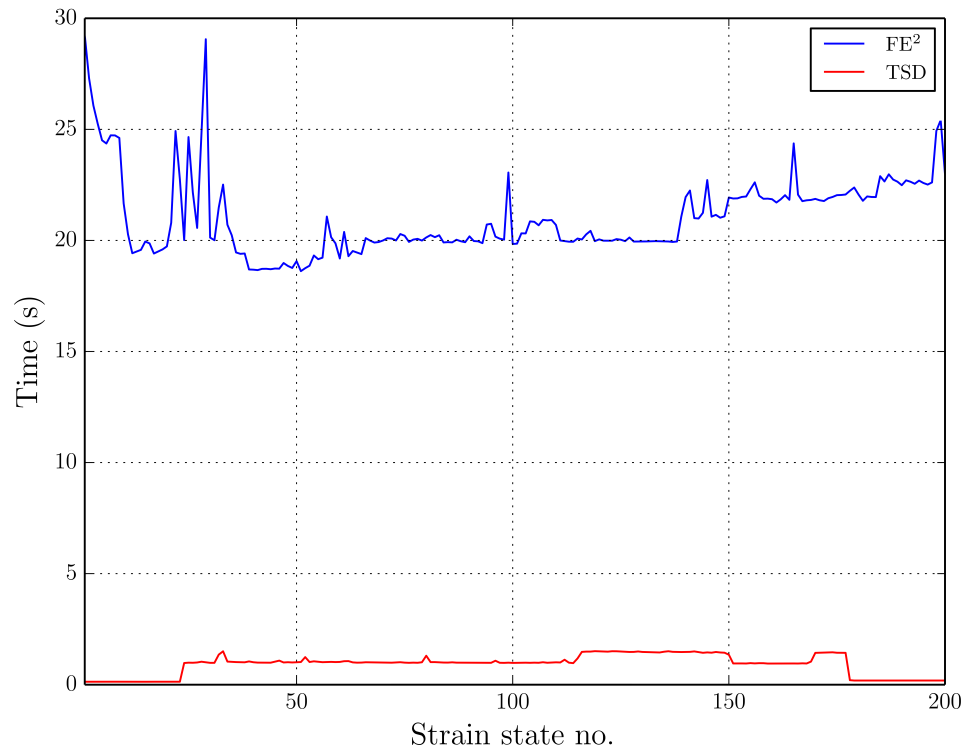


Figure 5.12: Computational times of the TSD model and  $\text{FE}^2$  method, for the set of 200 macroscopic strain states.

# Chapter 6

## Computational example

This chapter looks to evaluate the accuracy of the TSD model further and assess its ability in solving problems at the macro scale via a computational example. In this regard, a cantilever beam is analyzed for three different macroscopic loading types: tension, compression, and bending. To continue with the analysis from the previous chapter, the same database and MLS parameters discussed in Section 5.3.1 are used. Once again, we utilize the  $FE^2$  method to obtain a reference solution and evaluate the TSD model. The same RVE, as described in Section 5.1, is thus employed at the micro scale, with periodic boundary conditions prescribed. High-performance computers were utilized to reduce the computational effort of the  $FE^2$  method, enabling RVE simulations to be performed in parallel. In the case of the TSD model, only one processor was used.

In our previous analysis, the chosen RVE exhibited different responses to macroscopic strain states. This response, which reflected on both scales, was owed mainly to the material arrangement at the micro scale. To further extend our investigation into these effects, we consider the same macroscopic problem but reorientate the vector basis such that the material layers are no longer horizontal, but vertical.

The chapter is broken up into four parts. The first part describes the macroscopic geometry and introduces each of the loading cases. Results to each loading case, from both the TSD and  $FE^2$  model, are then discussed in their respective sections.

It should be noted here that the difference between the number of processes used for the  $FE^2$  and TSD models mean that an equivalent comparison in computational times is not possible. Thus, since the computational times in obtaining the macroscopic quantities required to solve the macroscopic problem was analysed in Section 5.3.4, no analysis in the computational time is discussed.

### 6.1 Macroscopic problem description

We describe the macroscopic problem as a cantilever beam with an incrementally applied deflection prescribed on the cross-sectional face, located at the end of the beam. Figure 6.1a shows the geometry of the beam, with the support and loading prescribed. We represent the

fixed supports by prescribing a zero displacement, in all three directions, on the cross-sectional end of the beam. The beam is discretized into 40 macroscopic elements and is illustrated in Figure 6.1. As per the computational example in Section 3.4, first order hexahedra elements are used to discretize the macroscopic sample.

As mentioned, the RVEs response is direction dependent. To analyse the effects of the RVE at the macro scale, we change the orientation of the macroscopic problem, with the  $y$  axis now being the parallel to the longitudinal length of the beam. This vector base transformation effectively describes a "new" RVE at the micro level, where the material layers are now vertically aligned. We use this material layer alignment to distinguish between the two macroscopic problems, denoting them H-RVE and V-RVE. Figure 6.1 gives a visualisation of the two beams, with their effective RVEs.

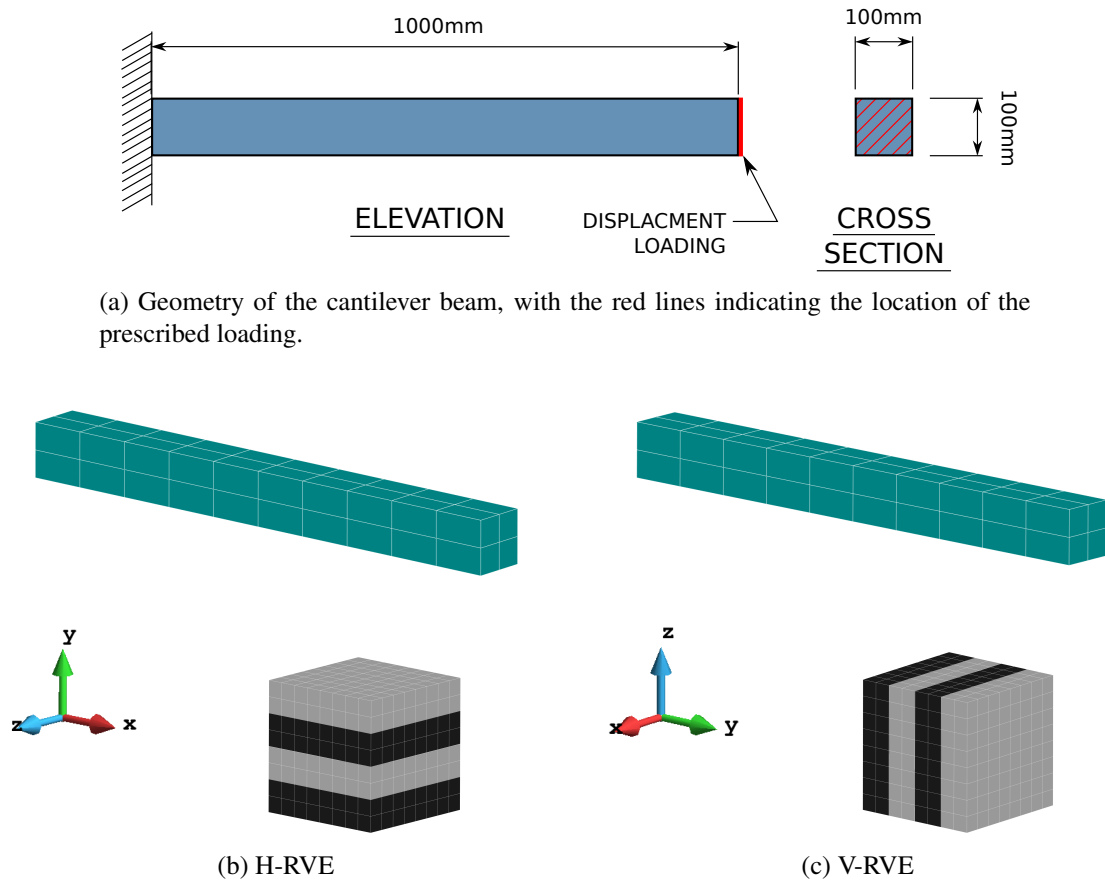


Figure 6.1: Macroscopic boundary value problem example: showing the beams geometry (a) and its discretized form and orientations at both scales, which are denoted according to the material layers orientation, (b) and (c).

The loading, which is prescribed on the right side, on the cross-sectional end as shown in Figure 6.1a, is prescribed as a fixed displacement. Table 6.1 presents the three loading cases to be analysed. The last two columns in this table are the directions of the fixed displacement, which correlate to the axes in Figure 6.1.

Table 6.1: Beam loading cases

Loading case	Displacement (mm)	Direction (H-RVE)	Direction (V-RVE)
Tension	150	$x$	$y$
Compression	-40	$x$	$y$
Bending	-80	$y$	$z$

In our analysis, we compute the traction forces on the boundary of the prescribed load using Equation (2.16),

$$\bar{\mathbf{t}} = \int_{\Gamma^t} \bar{\mathbf{P}} \bar{\mathbf{N}} d\Gamma = \int_{\Gamma^t} \bar{\mathbf{F}} \bar{\mathbf{S}} \bar{\mathbf{N}} d\Gamma, \quad (6.1)$$

where  $\Gamma^t$  is the surface boundary of the prescribed displacement load. In the load cases to follow, we present these traction forces as a magnitude and the displacements as an absolute value. To assess the TSD models accuracy, the  $L_2$ -norm relative error measure in Equation (5.4) is used, with  $(\hat{\bullet})$  and  $(\bar{\bullet})$  being the discrete displacements of the TSD and  $FE^2$  model, respectively.

## 6.2 Load Case 1: Tension

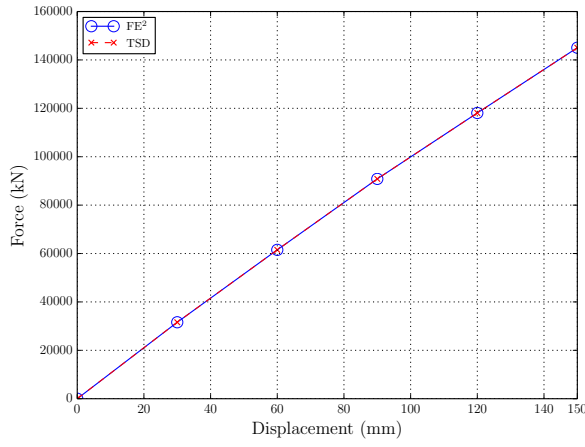
The first loading case deals with tension, which is prescribed as a loading displacement of 150mm. Figure 6.2 shows the results for both beams, solved using both models. We see here that the beams response is highly dependent on the orientation of the material layers, with beam H-RVE yielding a much stiffer response. This result was expected though, as the results from the previous chapter indicated the macroscopic response to be stiffer for strains acting parallel to the material layers. Another observation is the non-linear relationship between the reaction force and displacement, which is shown to be greater in beam V-RVE. This non-linearity is captured by the TSD model, for both beams, whose results appear to be in good agreement with the  $FE^2$  method.

The  $L_2$ -norm relative error of the displacements in both beams is provided in Table 6.2, and shows a better approximation for beam V-RVE.

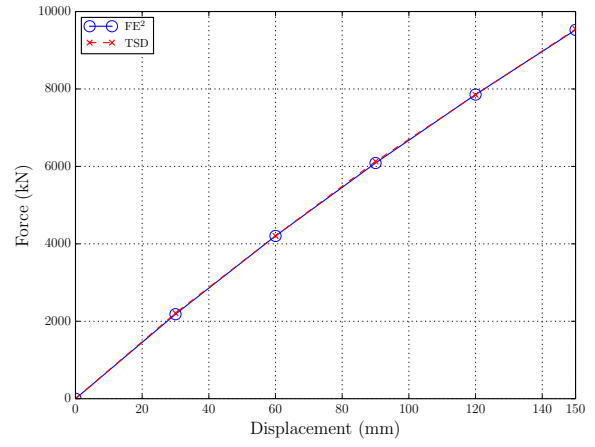
Table 6.2:  $L_2$ -norm relative error for the tensile loading case

Beam	H-RVE	V-RVE
$L_2$ -norm error	$2.95 \times 10^{-04}$	$6.03 \times 10^{-05}$

In Figure 6.3, the rate of convergence of the TSD and the  $FE^2$  model, for a typical Newton iteration, is compared for both beams. Despite the results being in good agreement, the TSD

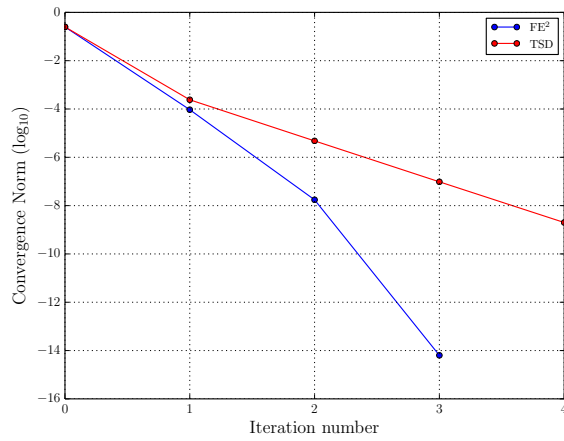


(a) H-RVE

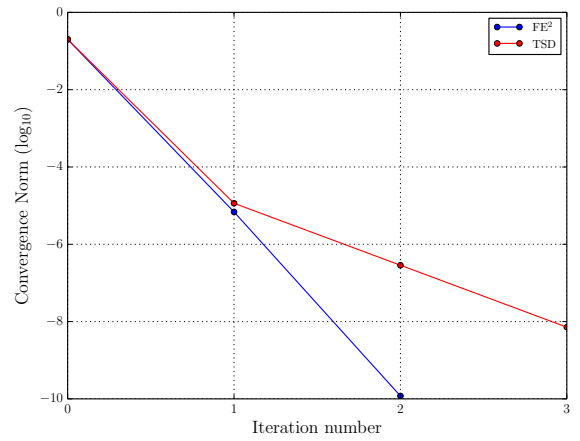


(b) V-RVE

Figure 6.2: Response to tension



(a) H-RVE



(b) V-RVE

Figure 6.3: Convergence results of a typical Newton iteration, for the tensile loading case, with  $\log_{10}$  scaling and a cut-off convergence norm of  $1 \times 10^{-8}$ .



model only exhibits first-order convergence, while the  $FE^2$  model shows second-order convergence.

### 6.3 Load Case 2: Compression

A 40mm longitudinal displacement is prescribed for the compressive load case. We present the results in Figure 6.4, with the response again being stiffer for beam H-RVE. Despite the non-linear relationship in the plots being less than the tensile loading case, a slight deviation between the TSD and  $FE^2$  solutions is shown, for both beams.

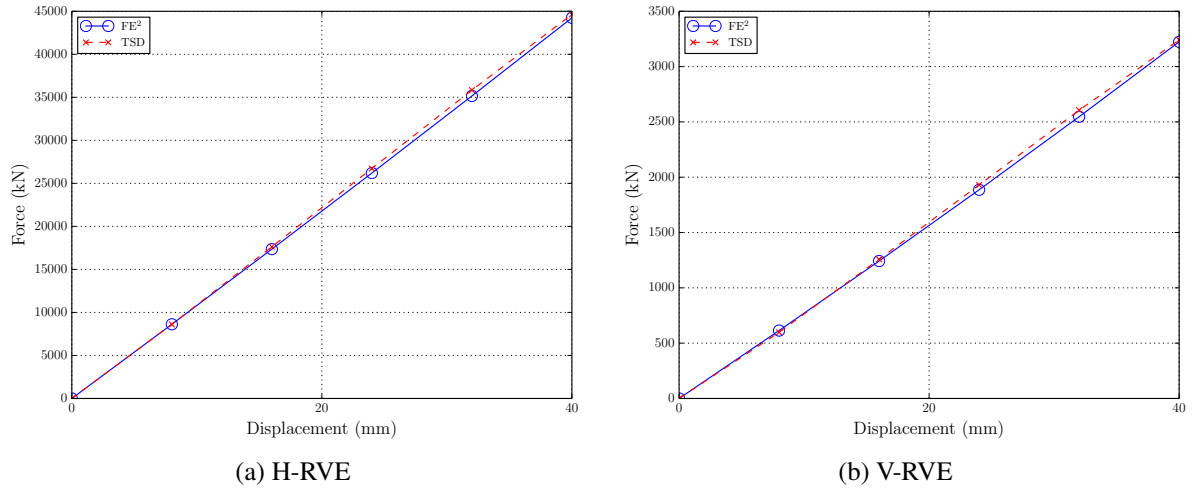


Figure 6.4: Response to compression

The  $L_2$ -norm relative error of the displacements for each beam is provided in Table 6.3. As per the tensile loading case, a better approximation is achieved for V-RVE.

Table 6.3:  $L_2$ -norm relative error for the compressive loading case

Beam	H-RVE	V-RVE
$L_2$ -norm error	$1.42 \times 10^{-03}$	$3.78 \times 10^{-04}$

The deviations exhibited in the results above are owed to the compressive strains, and their affiliation to the high non-linearities, exhibited by both  $\bar{\mathcal{S}}$  and  $\bar{\mathcal{H}}$ , in these regions. Due to the errors of the approximations, in these regions, which were shown to be higher for compressive than tensile strains, the TSD solutions are less accurate.

In the case of the two beams, and their  $L_2$ -norm error, a better approximation for beam V-RVE is attained due to the errors for  $\bar{\mathcal{S}}_{11}$  being higher than  $\bar{\mathcal{S}}_{22}$ , for the initial states of compressive strain. This is exemplified when comparing the magnitudes of the axial stresses, in Figure 6.5,

and their absolute differences, between the TSD and  $FE^2$  models, for the corresponding strains  $\bar{C}_{11}$  and  $\bar{C}_{22}$  in Figure 5.7.

Comparing the TSD and  $FE^2$  convergence rates, for both beams, in Figure 6.6, it can be seen that the TSD and  $FE^2$  model achieves first and second order convergence, respectively. While the rate of convergence is the same for the  $FE^2$  method, the convergence rate in the TSD model appears to stagnate, for beam V-RVE.

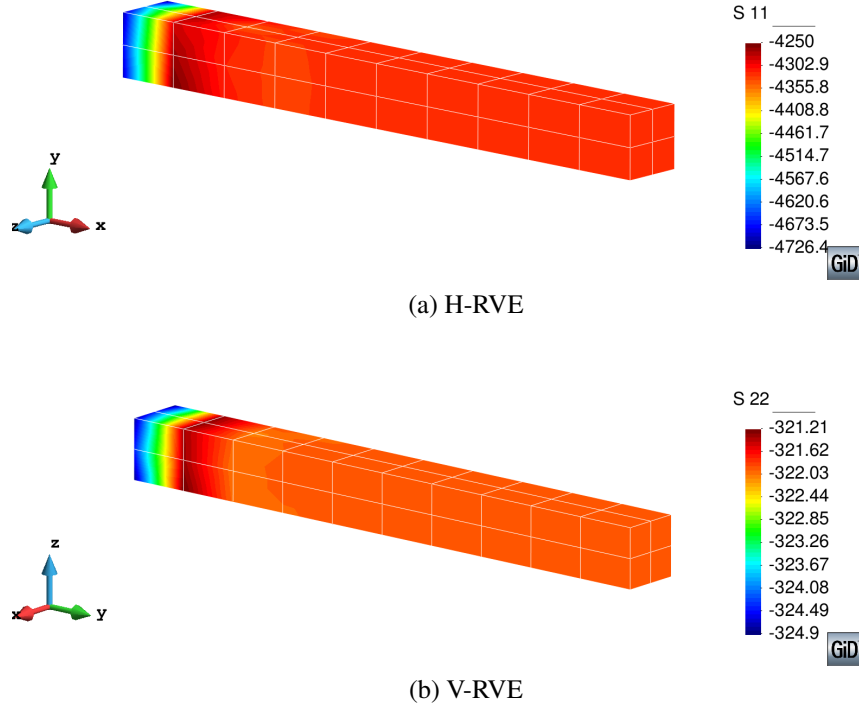
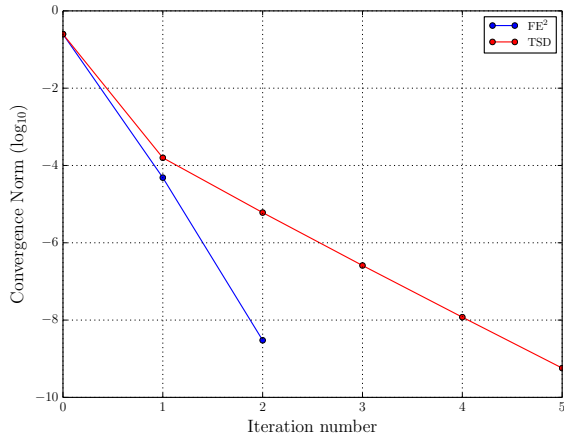
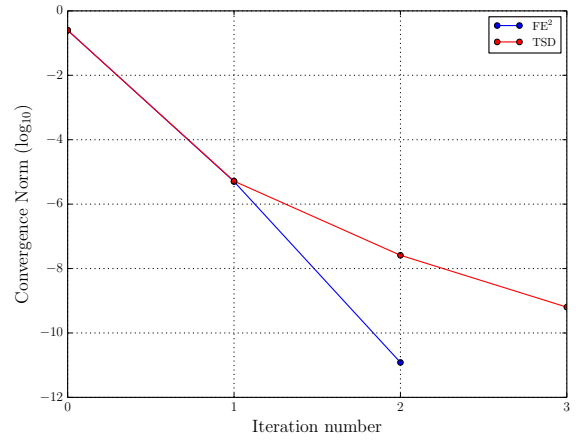


Figure 6.5: Contour plot of the normal macroscopic stresses  $\bar{S}_{11}$  and  $\bar{S}_{22}$ , for the compressive loading case, respectively.



(a) H-RVE



(b) V-RVE

Figure 6.6: Convergence results of a typical Newton iteration, for the compressive loading case, with  $\log_{10}$  scaling and a cut-off convergence norm of  $1 \times 10^{-8}$ .

## 6.4 Load Case 3: Bending

In the final loading case, we investigate the beams response to bending. Results for the prescribed vertical displacement are provided in Figure 6.7. While the previous loading cases showed stark differences in the reaction force, between the two beams, a similar magnitude is shown.

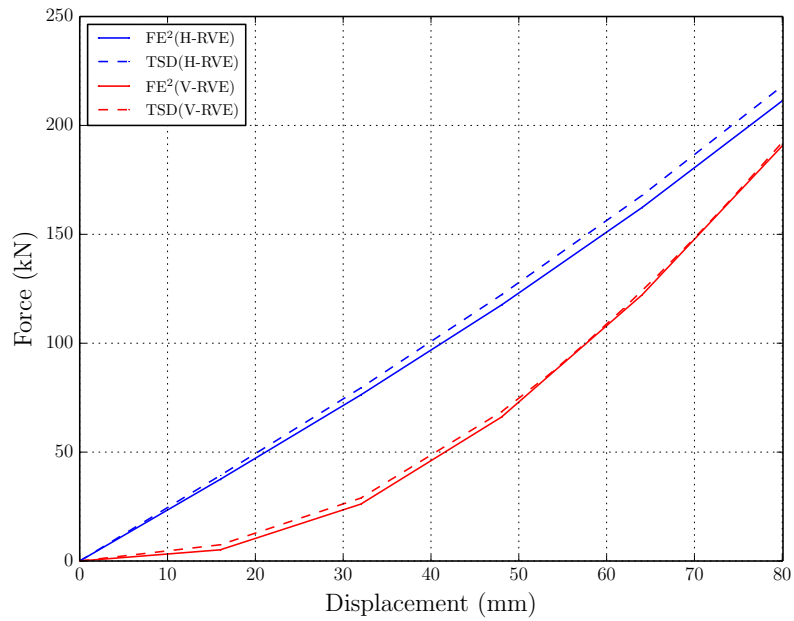


Figure 6.7: Response to bending

This phenomenon is explained when considering the changes in stress  $\overline{\mathbf{S}}$ , on the traction boundary  $\Gamma^t$ , in Equation (6.1), for the loading increments. Figure 6.8 shows this progression, as well as the strain  $\overline{\mathbf{E}}$ , at two points, whose locations are respectively given for each beam. Based on the directions of the surface normals in each beam, only the respective longitudinal components,  $S_{11}$  and  $S_{22}$ , and shear components,  $S_{31}$  and  $S_{23}$ , need be considered. We ignore  $S_{12}$ , in both beams, since the values were shown to be insignificant in comparison.

In Figure 6.8c, the normal stress values in beam H-RVE ( $S_{11}$ ) increase but stagnate as the loading increases. Conversely, beam V-RVE shows the normal stress values ( $S_{22}$ ) to rise exponentially. A similar observation is made for the shear stresses, except here, the stresses in H-RVE ( $S_{31}$ ) remain equivalent to zero. Again, a dependency is seen between the stresses and their respective strains, with V-RVE exhibiting larger increments in strain. The lower strains in H-RVE stem from the microstructural orientation and its stiffer response to these strain measures,  $E_{11}$  and  $E_{31}$ . Conversely, for beam V-RVE, the larger increase in  $E_{11}$  and  $E_{23}$ , with loading, is a consequence of the microstructures compliancy to these strains.

As per the compressive loading case, we see an overestimation of the TSD model solutions for beam H-RVE, while the solutions for beam V-RVE appear to be in good agreement. However, the  $L_2$ -norm relative error of the beams displacements, provided in Table 6.4, shows both beams to have similar results.

Table 6.4:  $L_2$ -norm relative error for the tensile loading case

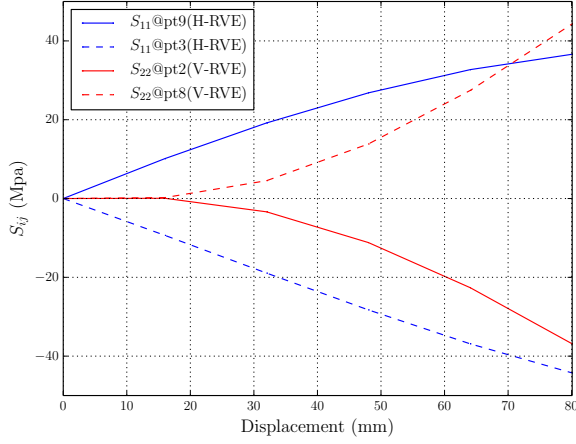
Beam	H-RVE	V-RVE
$L_2$ -norm error	$2.673 \times 10^{-03}$	$5.56 \times 10^{-03}$



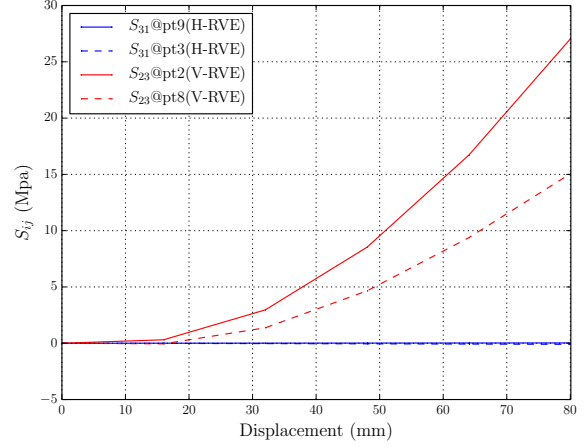
(a) Points 9 (top) and 3 (bottom) H-RVE



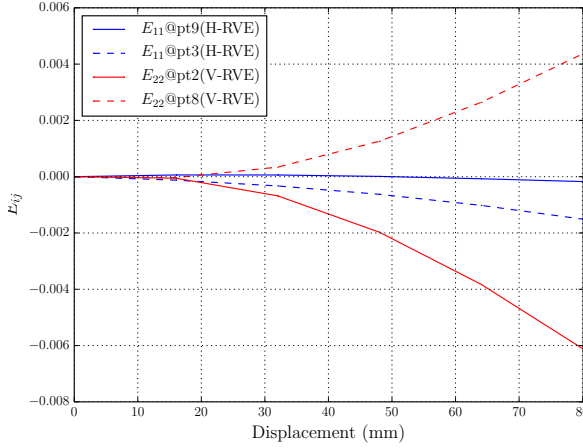
(b) Points 2 (top) and 8 (bottom) V-RVE



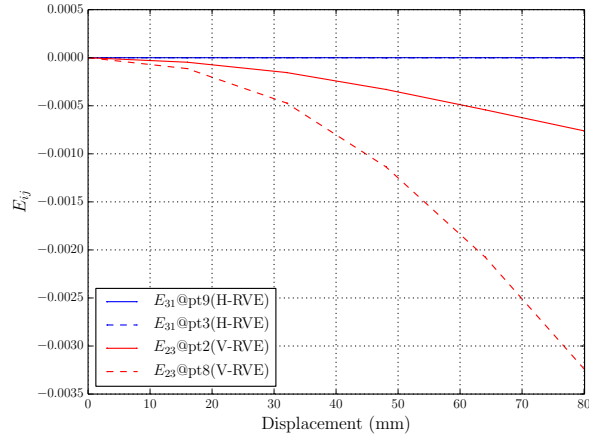
(c) Axial stresses



(d) Shear stresses



(e) Axial strains



(f) Shear strains

Figure 6.8: Evolution of the stress and strain at beam points for the bending loading case, with the values monitored at two points of each beam as shown, respectively.

A comparison between the convergence of the TSD and the  $FE^2$  model, for a typical Newton iteration, for both beams, is given in Figure 6.9. Once again, while the  $FE^2$  method exhibits second-order convergence, the TSD model shows only first-order convergence.

In this chapter, a macroscopic cantilever beam was analyzed, for different load cases, to assess the TSD models accuracy and its capability in solving macroscopic boundary value problems.

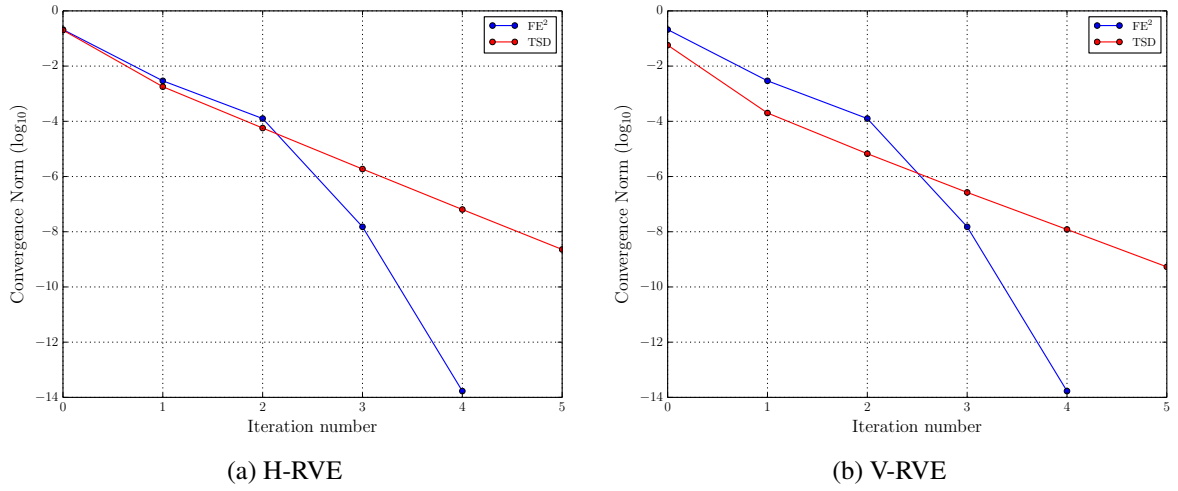


Figure 6.9: Convergence results of a typical Newton iteration, for the bending loading case, with log<sub>10</sub> scaling and a cut-off convergence norm of  $1 \times 10^{-8}$ .

It has been shown, for tension and compression, that when the material layers of the microstructure are parallel to the macroscopic longitudinal length, a stiffer response can be expected, than if the material layers are perpendicular. While this was also shown to be the case for bending, the response for the vertically aligned layers increased non-linearly.

With the exception to the bending case, the solutions of the TSD model were shown to yield better approximations for beam V-RVE than H-RVE. This came as a result of the axial strains and the accuracy of their approximations, with the strains acting parallel to the material layers yielding less accurate results, for their initial strain states.

In comparing the rate of convergence for the different load cases, in both beams, it was shown that the TSD model could only achieve first-order convergence. In the case of the FE<sup>2</sup> method, second-order convergence was shown for both beams, for all load cases. Similar to the discussion in the previous chapter, this is owed to the database density, resulting from the high limits of the chosen macroscopic strain domain, and the chosen polynomial basis of the MLS scheme. Should the range between the limits of the strain domain be reduced, the basis polynomial increased, or both, the rate of convergence would improve; however, further investigation into these effects would need to be undertaken.

# Chapter 7

## Summary, concluding remarks and future work

The primary objective of this research was to implement the conventional  $FE^2$  method, develop a two-scale database (TSD) model, and evaluate the TSD model against the  $FE^2$  method, in a 3-dimensional setting. In this chapter, we summarize the findings and present future works

### 7.1 The $FE^2$ method

The two-scale homogenization technique commonly known as the  $FE^2$  method has been implemented using the deformation driven approach, described by Schröder [89]. In defining this deformation driven two-scale model, periodic boundary conditions were prescribed on a RVE using a strongly coupled approach. Volumetric homogenization methods were adopted to determine the macroscopic variables, with the tangent operator computed as an additive decomposition of a Voigt-type bound term and a softening term. Both linear and non-linear isotropic elastic constitutive laws were developed at the micro scale.

Capable of capturing the microscopic effects at the macro scale, the developed model was able to successfully replicate qualitative results of a laminated composite beam with material degradation at the micro scale [76], see Section 3.4. Consisting of several layers of two materials, each constituent was characterised by an isotropic linear elastic micro constitutive law. The effects of material degradation were simulated by reducing the shear modulus in one of the materials. Issues relating to the computational demand of the  $FE^2$  method were also illustrated here, with the costs being highly dependent on the mesh size at both scales.

A numerical analysis was then conducted on a second RVE. The RVE was taken to be similar to the above, but instead of investigating material degradation, the materials were characterized by an isotropic non-linear Neo-Hookean micro constitutive law. Mechanical aspects of the RVE were investigated, for a set of prescribed macroscopic strain states, and revealed the RVEs response to be direction dependant. This response, which was also reflected in the homogenized macroscopic quantities, was owed to the RVEs material configuration, and its compliancy to strains acting in directions transverse to its material layers.

The effects of the analyzed RVE were then further examined via a macroscopic boundary value problem. In this regard, two cantilever beams, having the same geometry and RVE, were considered, with only their orientations to the macroscopic vector basis differing. This difference in vector basis effectively generated two beams of different microstructures, whose material layers at the micro scale were respectively positioned parallel (beam H-RVE) and perpendicular (beam V-RVE) to the beams longitudinal axis. The beams response was analysed for a series of displacement loads.

Computing the magnitude of the traction force, at the free cross-sectional end of the beam, reaffirmed the observations made in the RVEs analysis, with beam H-RVE having a stiffer response. Interestingly, beam V-RVEs response to bending revealed the traction force to increase exponential with the displacement loading. This non-linear relationship, exhibited only in beam V-RVE, was attributed to the exponential increase in stresses, resulting from the higher strain rates on the RVE. For all the load cases considered, a convergence rate of second-order was attained.

Based on the results seen from the  $FE^2$  method, it can be concluded that the multi-scale homogenization technique was successfully implemented. Furthermore, while the method has shown to be a useful tool in modelling microstructural effects at the macro scale, it is hindered by its computational demand.

## 7.2 The two-scale database model

A two-scale database model was developed to reduce the computational effort, associated with the  $FE^2$  method, while still maintaining a acceptable degree of accuracy. Utilising the Moving Least Squares method, macroscopic quantities were approximated from a set of precomputed RVEs. These RVEs are solved and homogenized, for a series of macroscopic strain states, in an off-line step and stored in a discretized macroscopic right *Cauchy-Green* strain space, or material database. The approach circumvents both the microscopic boundary value problem and homogenization process, thus reducing the computational costs.

Due to the RVE being assigned to each macroscopic integration point, and the macroscopic stress and tangent operator resulting from a macroscopic deformation, prescribed to the boundaries of the RVE, the macroscopic stress and tangent operator are said to be a function over the space of macroscopic deformations. Considering the macroscopic stress and tangent operator to be a discrete representation of the macroscopic deformation, one could obtain a good approximation for these macroscopic quantities, provided that these discrete representations have been computed for a sufficient number of points.

To generate the material database, each component of the defined macroscopic right *Cauchy-Green* strain domain was discretized into a finite number of particles. These discrete right *Cauchy-Green* strain deformations represent the boundary conditions at the micro level and characterize the material database. Attaching an RVE to each discrete strain state, the macroscopic stress and tangent operator is realized via solving and homogenizing a microscopic boundary value problem. Carrying this process out, for all the discrete strain states, a material database is realized.

The approximation of the stresses and tangent operator is done on the components of the



tensors. This is a common practice with tensor interpolation [49], with problems only being prevalent when its shape and directional information are of importance [39, 115]. The direct interpolation of the stress and tangent operator values has been done in previous works Terada and Kikuchi [105], and was thus considered permissible, in this instance, as the stress tensor has no physical interpretation [38]. The Moving Least Squares approximation method, described in Section 4.4.1, was used to approximate the macroscopic quantities and was chosen due to its usefulness in approximating highly dimensional problems [79].

The performance of the TSD model was assessed by approximating the macroscopic stress and tangent operator variables, for a series of macroscopic right *Cauchy-Green* strain states. In constructing the material database, the same RVE analyzed with the  $FE^2$  method, was considered. Following the assignment of the strain domain limits, the macroscopic strain space was discretized into one million right *Cauchy-Green* strain states. For the MLS approximation, a polynomial order of two was used. Solutions to the series of macroscopic right *Cauchy-Green* strain states were evaluated by computing its relative error, with those obtained using the  $FE^2$  method treated as the reference solution. Computational times were also compared to evaluate the TSD models computational performance.

Based on the results of the analysis, it was deduced that, in regions where the stress and tangent operator values are more non-linear, higher inaccuracies in the approximations can be anticipated. This issue was noted to be a common problem, for these model types, as the models fail to capture the highly non-linear geometries accurately [118]. Improvements to the TSD model could be attained by increasing the basis polynomial, in the MLS scheme, and strategically discretising the macroscopic strain space. An error sensitivity analysis would need to be undertaken in this regard though, as increasing the basis polynomial could increase the computational effort in the MLS approximation. Significant improvements in computational times were achieved, however, with the TSD model being 29 times faster than the  $FE^2$  method.

Two cantilever beams were then solved using the TSD model to assess its capability in solving macroscopic boundary value problems. In this instance, the same database, as that used in the previous evaluation, was considered. Once again, to assess its accuracy, solutions from the  $FE^2$  method were used. The results, for the tensile and compressive load cases, showed better approximations for beam V-RVE than H-RVE. This came as a result of the axial strains and the accuracy of their approximations, with the strains acting parallel to the material layers yielding less accurate results, for their initial strain states. While second-order convergence was shown for the  $FE^2$  method, the TSD model only exhibited first-order convergence. Similar to the previous analysis, the errors and first order convergence rate of the TSD model were owed to the database density, resulting from the high limits of the chosen macroscopic strain domain, and the chosen polynomial basis of the MLS scheme. Possible remedies to these issues is the reduction in the limits of the macroscopic strain domain and increasing the basis polynomial order of the MLS scheme.

In conclusion, the results showed that while the TSD model is computationally faster than the  $FE^2$  method, and capable of solving three-dimensional problems, the accuracies of the model are still left to be desired. Thus, a more detailed investigation into factors influencing its performance needs to be undertaken. Such factors include increasing the polynomial order in the MLS scheme and densification of the macroscopic strain space.

## 7.3 Future work

The  $FE^2$  database model utilised a database containing the homogenized stress and tangent operator values. Due to the number of parameters, a large sample of data points

Significant improvements to the method could be made if the database parameters are reduced. This would not only reduce the size of the database, and the number of simulations required, but also reduce the effort in reading the stored variables of the supporting particles in the MLS approximation. However, the difficulty in achieving this is establishing a relationship between the macroscopic deformation gradient, which drives the microscopic boundary value problem, and the parameters characterizing the database. A promising approach could be the use of eigenvalues to characterize the database. Such an approach has been adopted by Temizer and Zohdi [104], Guedes and Kikuchi [28] CONFIRM but is only applicable to isotropic materials. Despite this, the approach would still be worth investigating.

[116] introduced the use of numerically explicit potentials, which looks to store the strain energy potential of the RVE solution. The inclusion of this method should be investigated further as significant savings in hard-drive space, which is sometimes overlooked, can be achieved. Furthermore, the computational time required to read the stored values, for the MLS approximation, will be reduced.

In this work, the parameters of the database were evenly discretized, with the points in each **parameter domain** being evenly spaced. While it was shown in the MLS example that this type of discretization is beneficial, due to the even distribution of errors, this was not the case for the  $FE^2$  database model. To improve the accuracy of the model, the database would need to be refined. Three options may be considered to reduce

First option is rebuild the database with a reduced domain range. While this would no doubt improve the accuracies in the approximations, the scope on the type of boundary value problems reduce as the strain range may not cater for the problem. However, if one considers numerically explicit potentials, the extrapolation technique used by Yvonnet et al. [118] could be applied to address this issue. Alternatively, one may extend this technique to extrapolate the stored variables.

Second option is to add data points to the existing database. The appeal of this approach is that the current data points need not be computed. Adding a new point to the database however requires all combinations with the existing points, in the other parameters, to be computed.

Third option is to build the database more strategically. In order to achieve this, an analysis on the RVE must be undertaken to identify regions of high non-linearity

One of the biggest problems that may be faced later, is database refinement. Usually, two ways can be considered for uniform database refinement. In the first case, a new grid can be continuously generated with a slightly smaller spacing. In such a condition, the whole database has to be recomputed again. In the second scenario, new dataset parametric points could be placed specifically in the middle, between every other existing parametric point. In that case, the previous simulated parametric points do not need to be recomputed. However, adding a new point between existing points leads to an exponential rise in the number of points to be created. In both strategies, database refinement is very time-consuming and thus, increasing the accuracy of PODI can be a very expensive process. Many researchers across the literature have

devised different methods, which are commonly classified as sampling algorithms. One of them that looks favourable is the Latin

A severe limitation of the  $FE^2$  database model is the number of simulations and time required.

Investigation into improving its accurateness Method to rotate the basis vectors of a strain to that of the strain space. Following the effects influencing its accuracy, methods into extending the database could be explored. This includes the adaptive homogenization strategy, outlined by Temizer and Wriggers [101, 103], as well as extrapolating values from the database. Using multiple databases to investigate the influence of gap graded materials.

# Appendix A

## Prescribing periodic boundary conditions on the microscopic boundary value problem

We first, recall the periodic boundary condition, given in Equation (3.7)<sub>3</sub>,

$$\tilde{\mathbf{d}}^+ = \tilde{\mathbf{d}}^-,$$

where we shall refer to  $\tilde{\mathbf{d}}^+$  and  $\tilde{\mathbf{d}}^-$  as the fluctuating displacements of the dependent and independent node, respectively. As previously discussed, the strong coupling approach used in this work links the dependent node on the one side of the RVE to its corresponding independent node, on the opposite side. To kinematically constrain the RVE at the micro-level, we prescribe a zero fluctuation at the corner nodes, i.e.  $\tilde{\mathbf{d}}_{1,2,\dots,8} = \bar{\mathbf{0}}$ , as shown in Figure A.1.

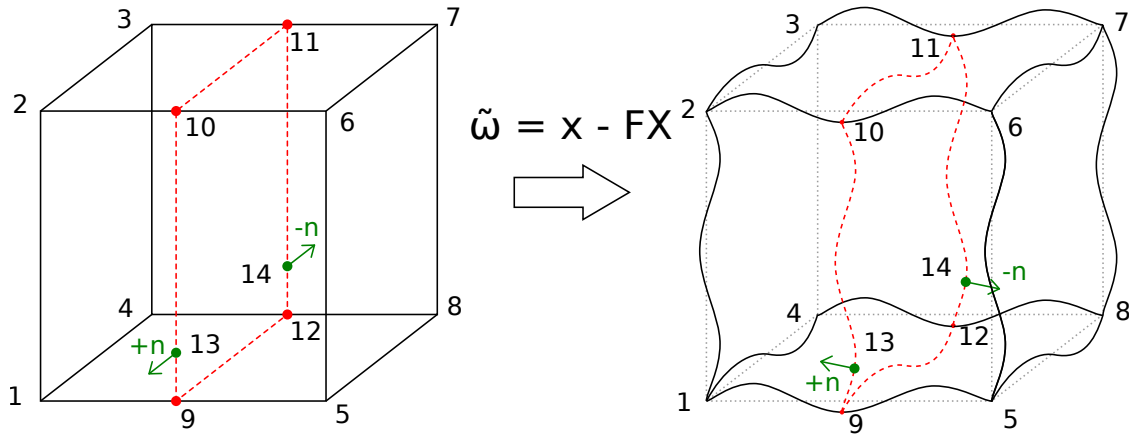


Figure A.1: 3-D schematic representation of the periodic boundary condition

The geometric constraint, required by the boundary condition, is maintained by these corner nodes. We treat node 1, with the reference coordinate vector  $\mathbf{X}^1$ , as the "master" reference node. We now select nodes 2, 3 and 5, such that these nodes, combined with node 1, form

a set of line vectors that are mutually orthogonal. A general expression for the fluctuating displacements, for any set of boundary nodes, is now given as:

$$\tilde{\mathbf{d}}^+ - \tilde{\mathbf{d}}^- - \tilde{\mathbf{d}}^n + \tilde{\mathbf{d}}^1 = 0, \quad (\text{A.1})$$

where  $n = 2, 3, 5$  is the corner node acting as a reference to the dependent node. Representing this in matrix form yields,

$$\begin{bmatrix} 1 & -1 & -1 & 1 \end{bmatrix} \begin{bmatrix} \tilde{\mathbf{d}}^+ \\ \tilde{\mathbf{d}}^- \\ \tilde{\mathbf{d}}^n \\ \tilde{\mathbf{d}}^1 \end{bmatrix} = 0. \quad (\text{A.2})$$

As shown in Figure A.1, the nodes located on the vertices (9,10,11,12) of the RVE fall onto two surfaces, respectively. In such cases, we take the node that falls on the two surfaces having independent nodes (i.e., node 9) to be independent and the other nodes to be dependent (i.e., nodes 10,11,12). Applying this condition across all boundary nodes yields a system of constraint equations,

$$C_{ab}\tilde{\mathbf{d}}_b = 0, \quad (\text{A.3})$$

where  $C_{ab}$  is a tensor of coefficients, consisting of 0, 1 and -1. An expression for the dependent nodes, in terms of those independent, can be obtained by partitioning the system of constraints,

$$\begin{aligned} \begin{bmatrix} C_{ad} & C_{ai} \end{bmatrix} \begin{bmatrix} \tilde{\mathbf{d}}_d \\ \tilde{\mathbf{d}}_i \end{bmatrix} &= 0 \\ C_{ad}\tilde{\mathbf{d}}_d + C_{ai}\tilde{\mathbf{d}}_i &= 0 \\ \tilde{\mathbf{d}}_d &= -C_{ad}^{-1}C_{ai}\tilde{\mathbf{d}}_i \\ \tilde{\mathbf{d}}_d &= C_{di}\tilde{\mathbf{d}}_i, \quad \text{where} \quad C_{di} = -C_{ad}^{-1}C_{ai}. \end{aligned} \quad (\text{A.4})$$

The tensor  $C_{ad}$  is a square singular matrix, due to the number of dependent degrees of freedom being equivalent to the number of constraint equations. Using this expression, we redefine the fluctuation vector, for all degrees of freedom,

$$\tilde{\mathbf{d}}_b = \begin{bmatrix} \tilde{\mathbf{d}}_i \\ \tilde{\mathbf{d}}_d \end{bmatrix} = T_{bm}\tilde{\mathbf{d}}'_m, \quad \text{with} \quad T_{bm} = \begin{bmatrix} \delta_{im} \\ C_{dm} \end{bmatrix}. \quad (\text{A.5})$$

The tensor  $T$  here is denoted as the transformation tensor. This tensor allows the microscopic linear equation system, Equation (3.4), to be transformed into a new linear system, containing only the independent degrees of freedom,

$$\begin{aligned}
K_{kb}\Delta\tilde{d}_b &= -r_k \\
T_{km}K_{kb}T_{bn}\Delta\tilde{d}'_n &= -T_{km}r_k \\
\begin{bmatrix} \delta_{im} & C_{dm} \end{bmatrix} \begin{bmatrix} K_{ii} & K_{id} \\ K_{di} & K_{dd} \end{bmatrix} \begin{bmatrix} \delta_{in} \\ C_{dn} \end{bmatrix} \Delta\tilde{d}'_n &= \begin{bmatrix} \delta_{im} & C_{dm} \end{bmatrix} \begin{bmatrix} r_i \\ r_d \end{bmatrix} \\
\begin{bmatrix} \delta_{im}K_{ii} + C_{dm}K_{di} & \delta_{im}K_{id} + C_{dm}K_{dd} \end{bmatrix} \begin{bmatrix} \delta_{in} \\ C_{dn} \end{bmatrix} \Delta\tilde{d}'_n &= \begin{bmatrix} \delta_{im}r_i + C_{dm}r_d \end{bmatrix} \\
(\delta_{im}K_{ii}\delta_{in} + C_{dm}K_{di}\delta_{in} + \delta_{im}K_{id}C_{dn} + C_{dm}K_{dd}C_{dn})\Delta\tilde{d}'_n &= r'_m \\
K'_{mn}\Delta\tilde{d}'_n &= r'_m.
\end{aligned}$$

The transformed equation system still contains the prescribed displacements on the corners of the RVE, as these are essentially independent. Solving for the incremental independent fluctuations, as before, we set the incremental fluctuation field using Equation (A.5), and update the fluctuation field using Equation (3.6).



# Appendix B

## Ethics Approval

Application for Approval of Ethics in Research (EIR) Projects  
Faculty of Engineering and the Built Environment, University of Cape Town

### APPLICATION FORM

**Please Note:**

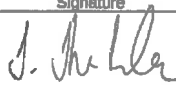

Any person planning to undertake research in the Faculty of Engineering and the Built Environment (EBE) at the University of Cape Town is required to complete this form before collecting or analysing data. The objective of submitting this application prior to embarking on research is to ensure that the highest ethical standards in research, conducted under the auspices of the EBE Faculty, are met. Please ensure that you have read, and understood the EBE Ethics in Research Handbook (available from the UCT EBE, Research Ethics website) prior to completing this application form: <http://www.ebe.uct.ac.za/ebe/research/ethics1>

APPLICANT'S DETAILS		
Name of principal researcher, student or external applicant		Nicholas Jarratt
Department		Department of Civil Engineering
Preferred email address of applicant:		JRRNIC001@myuct.ac.za
If Student	Your Degree: e.g., MSc, PhD, etc.	MSc
	Credit Value of Research: e.g., 60/120/180/360 etc.	180
	Name of Supervisor (if supervised):	A. Prof. Sebastian Skatulla
If this is a research contract, indicate the source of funding/sponsorship		
Project Title		An efficient three-dimensional database driven approach for multi scale homogenization

I hereby undertake to carry out my research in such a way that:

- there is no apparent legal objection to the nature or the method of research; and
- the research will not compromise staff or students or the other responsibilities of the University;
- the stated objective will be achieved, and the findings will have a high degree of validity;
- limitations and alternative interpretations will be considered;
- the findings could be subject to peer review and publicly available; and
- I will comply with the conventions of copyright and avoid any practice that would constitute plagiarism.

SIGNED BY	Full name	Signature	Date
Principal Researcher/ Student/External applicant	Nicholas Jarratt		24/01/2019

APPLICATION APPROVED BY	Full name	Signature	Date
Supervisor (where applicable)	A. Prof. Sebastian Skatulla		24/1/19
HOD (or delegated nominee) Final authority for all applicants who have answered NO to all questions in Section 1; and for all Undergraduate research (Including Honours).	DG Randall		29/01/2019
Chair : Faculty EIR Committee For applicants other than undergraduate students who have answered YES to any of the above questions.			



# Bibliography

- [1] D. Balzani, D. Brands, and J. Schröder. Construction of Statistically Similar Representative Volume Elements. In J. Schröder and K. Hackl, editors, *Plasticity and Beyond*, volume 550, pages 355–412. Springer Vienna, 2014. ISBN 978-3-7091-1624-1. doi: 10.1007/978-3-7091-1625-8\_6.
- [2] S. Bargmann, B. Klusemann, J. Markmann, J. E. Schnabel, K. Schneider, C. Soyarslan, and J. Wilmers. Generation of 3D representative volume elements for heterogeneous materials: A review. *Prog. Mater. Sci.*, 96:322–384, 2018. ISSN 00796425. doi: 10.1016/j.pmatsci.2018.02.003.
- [3] Bensoussan. *Asymptotic Analysis for Periodic Structures*. North-Holland, Amsterdam, 1978. ISBN 9780444851727. doi: 10.1016/S0168-2024(08)70198-X.
- [4] J. G. Berryman. Bounds and self-consistent estimates for elastic constants of polycrystals composed of orthorhombics or crystals with higher symmetries. *Phys. Rev. E - Stat. Nonlinear, Soft Matter Phys.*, 83(4):1–11, 2011. ISSN 15393755. doi: 10.1103/PhysRevE.83.046130.
- [5] R. G. M. Breuls, B. G. Sengers, C. W. J. Oomens, C. V. C. Bouten, and F. P. T. Baaijens. Predicting Local Cell Deformations in Engineered Tissue Constructs: A Multilevel Finite Element Approach. *Journal of Biomechanical Engineering*, 124(2):198, 2002. ISSN 01480731. doi: 10.1115/1.1449492.
- [6] B. Budiansky. On the elastic moduli of some heterogeneous materials. *Journal of the Mechanics and Physics of Solids*, 13(4):223–227, 1965. ISSN 00225096. doi: 10.1016/0022-5096(65)90011-6.
- [7] Y. Cai, L. Xu, and G. Cheng. Novel numerical implementation of asymptotic homogenization method for periodic plate structures. *International Journal of Solids and Structures*, 51(1):284–292, 2014. ISSN 00207683. doi: 10.1016/j.ijsolstr.2013.10.003.
- [8] P. P. Castañeda. Exact second-order estimates for the effective mechanical properties of nonlinear composite materials. *Journal of the Mechanics and Physics of Solids*, 44(6): 827–862, 1996. ISSN 00225096. doi: 10.1016/0022-5096(96)00015-4.
- [9] A. Clément, C. Soize, and J. Yvonnet. Computational nonlinear stochastic homogenization using a nonconcurrent multiscale approach for hyperelastic heterogeneous microstructures analysis. *International Journal for Numerical Methods in Engineering*, 91(8):799–824, 2012. ISSN 00295981. doi: 10.1002/nme.4293.

- [10] F. Covezzi, S. de Miranda, S. Marfia, and E. Sacco. Multiscale analysis of nonlinear composites via a mixed reduced order formulation. *Composite Structures*, 203(May): 810–825, 2018. ISSN 02638223. doi: 10.1016/j.compstruct.2018.05.073.
- [11] E. A. de Souza Neto and R. A. Feijóo. Variational Foundation of multi-scale constitutive models of solids: small and large strain kinematical formulation. *LNCC Res. Dev. Intern. Rep.*, (16):1–53, 2006.
- [12] E. A. de Souza Neto and R. A. Feijóo. On the equivalence between spatial and material volume averaging of stress in large strain multi-scale solid constitutive models. *Mechanics of Materials*, 40(10):803–811, 2008. ISSN 01676636. doi: 10.1016/j.mechmat.2008.04.006.
- [13] G. DeBotton, I. Hariton, and E. A. Socolsky. Neo-Hookean fiber-reinforced composites in finite elasticity. *Journal of the Mechanics and Physics of Solids*, 54(3):533–559, 2006. ISSN 00225096. doi: 10.1016/j.jmps.2005.10.001.
- [14] G. Dvorak. Transformation Field Analysis of Inelastic Composite Materials. *Proceedings of the Royal Society of London A: Mathematical, Physical and Engineering Sciences*, 437:311–327, 1992. ISSN 01787675. doi: 10.1007/BF00370073.
- [15] F. El Halabi, D. González, A. Chico, and M. Doblaré. FE2 multiscale in linear elasticity based on parametrized microscale models using proper generalized decomposition. *Computer Methods in Applied Mechanics and Engineering*, 257:183–202, 2013. ISSN 00457825. doi: 10.1016/j.cma.2013.01.011.
- [16] J. D. Eshelby. The determination of the elastic field of an ellipsoidal inclusion and related problems. *Proceedings of the Royal Society of London A: Mathematical, Physical and Engineering Sciences*, 241(1226):376–396, 1957. ISSN 1364-5021. doi: 10.1098/rspa.1957.0133.
- [17] F. Feyel and J.-L. Chaboche. FE2 multiscale approach for modelling the elastoviscoplastic behaviour of long fibre SiC/Ti composite materials. *Computer Methods in Applied Mechanics and Engineering*, 183(3-4):309–330, 2000. ISSN 00457825. doi: 10.1016/S0045-7825(99)00224-8.
- [18] J. Fish and V. Belsky. Multi-grid method for periodic heterogeneous media Part 2: Multiscale modeling and quality control in multidimensional case. *Computer Methods in Applied Mechanics and Engineering*, 1995. ISSN 00457825. doi: 10.1016/0045-7825(95)00812-F.
- [19] M. Găărău and P. Suquet. Effective properties of porous ideally plastic or viscoplastic materials containing rigid particles. *Journal of the Mechanics and Physics of Solids*, 45(6):873–902, 1997. ISSN 00225096. doi: 10.1016/S0022-5096(96)00128-7.
- [20] M. G. D. Geers. *Experimental analysis and computational modelling of damage and fracture*. PhD thesis, Eindhoven University of Technology, 1997.
- [21] M. G. D. Geers, V. G. Kouznetsova, and W. A. M. Brekelmans. Multi-scale computational homogenization: Trends and challenges. *Fourth Int. Conf. Adv. Comput.*

- Methods Eng. (ACOMEN 2008)*, 234(7):2175–2182, jan 2010. ISSN 0377-0427. doi: <http://dx.doi.org/10.1016/j.cam.2009.08.077>.
- [22] A. S. Gendy and A. F. Saleeb. Nonlinear material parameter estimation for characterizing hyper elastic large strain models. *Computational Mechanics*, 25(1):66–77, 2000. ISSN 0178-7675. doi: 10.1007/s004660050016.
  - [23] S. Ghosh, K. Lee, and S. Moorthy. Multiple scale analysis of heterogeneous elastic structures using homogenization theory and voronoi cell finite element method. *International Journal of Solids and Structures*, 32(1):27–62, 1995. ISSN 00207683. doi: 10.1016/0020-7683(94)00097-G.
  - [24] S. Ghosh, K. Lee, and S. Moorthy. Two scale analysis of heterogeneous elastic-plastic materials with asymptotic homogenization and Voronoi cell finite element model. *Computer Methods in Applied Mechanics and Engineering*, 132(95):63–116, 1996. ISSN 00457825. doi: 10.1016/0045-7825(95)00974-4.
  - [25] S. Ghosh, K. Lee, and P. Raghavan. *A multi-level computational model for multi-scale damage analysis in composite and porous materials*, volume 38. 2001. ISBN 1614292736. doi: 10.1016/S0020-7683(00)00167-0.
  - [26] I. M. Gitman, H. Askes, and L. J. Sluys. Representative volume: Existence and size determination. *Eng. Fract. Mech.*, 74(16):2518–2534, 2007. ISSN 00137944. doi: 10.1016/j.engfracmech.2006.12.021.
  - [27] T. Goda, K. Váradi, and K. Friedrich. Fe mirco-models to study contact states, stresses and failure mechanisms in a polymer composite subjected to a sliding steel asperity. *Wear*, 250-251:1584–1590, 2001. ISSN 00431648. doi: 10.1016/S0043-1648(01)00797-9.
  - [28] J. M. Guedes and N. Kikuchi. Preprocessing and postprocessing for materials based on the homogenization method with adaptive finite element methods. *Computer Methods in Applied Mechanics and Engineering*, 83(2):143–198, oct 1990. ISSN 00457825. doi: 10.1016/0045-7825(90)90148-F.
  - [29] Z. Gürdal, R. T. Haftka, and P. Hajela. *Design and Optimization of Laminated Composite Materials*. Wiley, 1999. ISBN 047125276X.
  - [30] Z. Hashin. Analysis of Composite Materials - A Survey. 50(3):481–505, 1983. ISSN 00218936. doi: 10.1115/1.3167081.
  - [31] Z. Hashin and S. Shtrikman. On some variational principles in anisotropic and nonhomogeneous elasticity. *Journal of the Mechanics and Physics of Solids*, 10(4):335–342, 1962. ISSN 00225096. doi: 10.1016/0022-5096(62)90004-2.
  - [32] S. Hazanov and C. Huet. Order relationships for boundary conditions effect in heterogeneous bodies smaller than the representative volume. *Journal of the Mechanics and Physics of Solids*, 42(12):1995–2011, 1994. ISSN 00225096. doi: 10.1016/0022-5096(94)90022-1.

- [33] J. A. Hernández, J. Oliver, A. E. Huespe, M. A. Caicedo, and J. C. Cante. High-performance model reduction techniques in computational multiscale homogenization. *Computer Methods in Applied Mechanics and Engineering*, 276:149–189, 2014. ISSN 00457825. doi: 10.1016/j.cma.2014.03.011.
- [34] R. Hill. Elastic properties of reinforced solids: Some theoretical principles. *Journal of the Mechanics and Physics of Solids*, 11(5):357–372, 1963. ISSN 00225096. doi: 10.1016/0022-5096(63)90036-X.
- [35] R. Hill. A SELF-CONSISTENT MECHANICS OF COMPOSITE MATERIALS. *J. Meh. Phys. Solids*, 13:213–222, 1965. ISSN 00225096. doi: 10.1016/0022-5096(65)90010-4.
- [36] R. Hill. On Constitutive Macro-Variables for Heterogeneous Solids at Finite Strain. *Proc. R. Soc. A Math. Phys. Eng. Sci.*, 326(1565):131–147, jan 1972. ISSN 1364-5021. doi: 10.1098/rspa.1972.0001.
- [37] R. Hill. On Macroscopic Effects Of Heterogeneity In Elastoplastic Media At Finite Strain. *Mathematical Proceedings of the Cambridge Philosophical Society*, 1984. ISSN 14698064. doi: 10.1017/S0305004100061818.
- [38] G. Holzapfel. *Nonlinear solid mechanics: a continuum approach for engineering*. Wiley, 2000, 2004. ISBN 9780471823049.
- [39] I. Hotz and J. Sreevalsan-Nair. Tensor field reconstruction based on eigenvector and eigenvalue interpolation. *Scientific Visualization: Advanced Concepts*, pages 110–123, 2010. doi: 10.4230/DFU.SciViz.2010.110.
- [40] H. Huang and R. Talreja. Numerical simulation of matrix micro-cracking in short fiber reinforced polymer composites: Initiation and propagation. *Compos. Sci. Technol.*, 66(15):2743–2757, 2006. ISSN 02663538. doi: 10.1016/j.compscitech.2006.03.013.
- [41] C. Huet. Application of variational concepts to size effects in elastic heterogeneous bodies. *Journal of the Mechanics and Physics of Solids*, 38(6):813–841, 1990. ISSN 00225096. doi: 10.1016/0022-5096(90)90041-2.
- [42] C. Huet. Coupled size and boundary-condition effects in viscoelastic heterogeneous and composite bodies. *Mechanics of Materials*, 31(12):787–829, dec 1999. ISSN 01676636. doi: 10.1016/S0167-6636(99)00038-1.
- [43] A. L. Kalamkarov, I. V. Andrianov, and V. V. Danishevs'kyi. Asymptotic Homogenization of Composite Materials and Structures. *Appl. Mech. Rev.*, 62(3): 030802, 2009. ISSN 00036900. doi: 10.1115/1.3090830.
- [44] T. Kanit, S. Forest, I. Galliet, V. Mounoury, and D. Jeulin. Determination of the size of the representative volume element for random composites: Statistical and numerical approach. *International Journal of Solids and Structures*, 40(13-14):3647–3679, 2003. ISSN 00207683. doi: 10.1016/S0020-7683(03)00143-4.

- [45] B. Klusemann and M. Ortiz. Acceleration of material-dominated calculations via phase-space simplicial subdivision and interpolation. *International Journal for Numerical Methods in Engineering*, 103(4):256–274, jul 2015. ISSN 00295981. doi: 10.1002/nme.4887.
- [46] V. Kouznetsova. *Computational homogenization for the multi-scale analysis of multi-phase materials*. PhD thesis, Eindhoven University of Technology, 2002.
- [47] V. Kouznetsova, W. a. M. Brekelmans, and F. P. T. Baaijens. Approach to micro-macro modeling of heterogeneous materials. *Computational Mechanics*, 27(1):37–48, 2001. ISSN 01787675. doi: 10.1007/s004660000212.
- [48] V. Kouznetsova, M. Geers, and W. Brekelmans. Computational homogenisation for non-linear heterogeneous solids. In *Multiscale modeling in solid mechanics: computational approaches*, pages 1–42. World Scientific, 2010.
- [49] A. Kratz, C. Auer, M. Stommel, and I. Hotz. Visualization and analysis of second-order tensors: Moving beyond the symmetric positive-definite case. *Comput. Graph. Forum*, 32(1):49–74, 2013. ISSN 14678659. doi: 10.1111/j.1467-8659.2012.03231.x.
- [50] E. Kröner. Elastic moduli of perfectly disordered composite materials. *Journal of the Mechanics and Physics of Solids*, 15(5):319–329, 1967. ISSN 00225096. doi: 10.1016/0022-5096(67)90026-9.
- [51] W. M. Lai, D. Rubin, and E. Krempl. *Introduction to Continuum Mechanics*. Elsevier, 4<sup>th</sup> edition, 2010. ISBN 9780521875622. doi: 10.1016/B978-0-7506-8560-3.X0001-1.
- [52] P. Lancaster and K. Salkauskas. Surfaces generated by moving least squares methods. *Mathematics of Computation*, 37(155):141–141, 1981. ISSN 0025-5718. doi: 10.1090/S0025-5718-1981-0616367-1.
- [53] F. Larsson, K. Runesson, S. Saroukhani, and R. Vafadari. Computational homogenization based on a weak format of micro-periodicity for RVE-problems. *Computer Methods in Applied Mechanics and Engineering*, 200(1-4):11–26, jan 2011. ISSN 00457825. doi: 10.1016/j.cma.2010.06.023.
- [54] R. Larsson and S. Diebels. A second-order homogenization procedure for multi-scale analysis based on micropolar kinematics. *International Journal for Numerical Methods in Engineering*, 69(12):2485–2512, 2007. ISSN 00295981. doi: 10.1002/nme.1854.
- [55] C. Y. Lee and W. Yu. Homogenization and dimensional reduction of composite plates with in-plane heterogeneity. *International Journal of Solids and Structures*, 48(10):1474–1484, 2011. ISSN 00207683. doi: 10.1016/j.ijsolstr.2011.01.032.
- [56] K. Lee and S. Ghosh. A microstructure based numerical method for constitutive modeling of composite and porous materials. *Materials Science and Engineering: A*, 272(1):120–133, 1999. ISSN 09215093. doi: 10.1016/S0921-5093(99)00475-X.
- [57] C. Liu and C. Reina. Discrete averaging relations for micro to macro transition. *Journal of Applied Mechanics*, pages 1–22, 2015. ISSN 0021-8936. doi: 10.1115/1.4033552.

- [58] J. Mandel. *Plasticité classique et viscoplasticité: course held at the Department of Mechanics of Solids, September-October, 1971*. Courses and lectures - International Centre for Mechanical Sciences. Springer-Verlag, 1972. ISBN 9780387811970.
- [59] S. Marfia and E. Sacco. Computational homogenization of composites experiencing plasticity, cracking and debonding phenomena. *Computer Methods in Applied Mechanics and Engineering*, 2016. ISSN 00457825. doi: 10.1016/j.cma.2016.02.007.
- [60] G. T. Mase, R. E. Smelser, and G. E. Mase. *Continuum Mechanics for Engineers*. CRC Press, 3<sup>rd</sup> edition, 2009. ISBN 9781420085389.
- [61] K. Matouš, M. G. Geers, V. G. Kouznetsova, and A. Gillman. A review of predictive nonlinear theories for multiscale modeling of heterogeneous materials. *Journal of Computational Physics*, 330:192–220, 2017. ISSN 10902716. doi: 10.1016/j.jcp.2016.10.070.
- [62] M. Meuwissen. *An inverse Method for the mechanical characterisation of metals*. PhD thesis, Eindhoven University of Technology, 1998.
- [63] J. C. Michel, H. Moulinec, and P. Suquet. Effective properties of composite materials with periodic microstructure: a computational approach. *Computer Methods in Applied Mechanics and Engineering*, 172(1–4):109–143, 1999. ISSN 0045-7825. doi: 10.1016/S0045-7825(98)00227-8.
- [64] C. Miehe and C. G. Bayreuther. On multiscale FE analyses of heterogeneous structures: from homogenization to multigrid solvers. *International Journal for Numerical Methods in Engineering*, 71(10):1135–1180, sep 2007. ISSN 00295981. doi: 10.1002/nme.1972.
- [65] C. Miehe and A. Koch. Computational micro-to-macro transitions of discretized microstructures undergoing small strains. *Archive of Applied Mechanics*, 72(4-5):300–317, 2002. ISSN 09391533. doi: 10.1007/s00419-002-0212-2.
- [66] C. Miehe, J. Schotte, and J. Schröder. Computational micro–macro transitions and overall moduli in the analysis of polycrystals at large strains. *Computational Materials Science*, 16(1-4):372–382, 1999. ISSN 09270256. doi: 10.1016/S0927-0256(99)00080-4.
- [67] C. Miehe, J. Schröder, and J. Schotte. Computational homogenization analysis in finite plasticity Simulation of texture development in polycrystalline materials. *Computer Methods in Applied Mechanics and Engineering*, 171(3–4):387–418, sep 1999. ISSN 0045-7825. doi: [http://dx.doi.org/10.1016/S0045-7825\(98\)00218-7](http://dx.doi.org/10.1016/S0045-7825(98)00218-7).
- [68] J. Miranda Guedes. *Nonlinear computational models for composite materials using homogenization*. PhD thesis, University of Michigan, 1990.
- [69] H. Moulinec and P. Suquet. A numerical method for computing the overall response of nonlinear composites with complex microstructure. *Computer Methods in Applied Mechanics and Engineering*, 157(1-2):69–94, apr 1998. ISSN 00457825. doi: 10.1016/S0045-7825(97)00218-1.

- [70] S. Nemat-Nasser. Averaging theorems in finite deformation plasticity. *Mechanics of Materials*, 31(8):493–523, 1999. ISSN 01676636. doi: 10.1016/S0167-6636(98)00073-8.
- [71] S. Nemat-Nasser and M. Hori. *Micromechanics: Overall Properties of Heterogeneous Materials*, volume 37. Elsevier, Amsterdam, 1993. ISBN 9780444898814.
- [72] R. W. Ogden, G. Saccomandi, and I. Sgura. Fitting hyperelastic models to experimental data. *Computational Mechanics*, 34(6):484–502, 2004. ISSN 01787675. doi: 10.1007/s00466-004-0593-y.
- [73] T. Okabe, T. Sasayama, and J. Koyanagi. Micromechanical simulation of tensile failure of discontinuous fiber-reinforced polymer matrix composites using Spring Element Model. *Composites Part A: Applied Science and Manufacturing*, 56:64–71, 2014. ISSN 1359835X. doi: 10.1016/j.compositesa.2013.09.012.
- [74] J. I. Okada, T. Washio, and T. Hisada. Study of efficient homogenization algorithms for nonlinear problems: Approximation of a homogenized tangent stiffness to reduce computational cost. *Computational Mechanics*, 46(2):247–258, 2010. ISSN 01787675. doi: 10.1007/s00466-009-0432-1.
- [75] M. Ostoja-Starzewski. Material spatial randomness: From statistical to representative volume element. *Probabilistic Eng. Mech.*, 21(2):112–132, 2006. ISSN 02668920. doi: 10.1016/j.probengmech.2005.07.007.
- [76] F. Otero, S. Oller, X. Martinez, and O. Salomón. Numerical homogenization for composite materials analysis. Comparison with other micro mechanical formulations. *Composite Structures*, 122:405–416, 2015. ISSN 02638223. doi: 10.1016/j.compstruct.2014.11.041.
- [77] I. Özdemir, W. A. M. Brekelmans, and M. G. D. Geers. computational homogenization for the thermo-mechanical analysis of heterogeneous solids. *Computer Methods in Applied Mechanics and Engineering*, 198(3–4):602–613, 2008. ISSN 0045-7825. doi: <http://dx.doi.org/10.1016/j.cma.2008.09.008>.
- [78] I. Özdemir, W. A. M. Brekelmans, and M. G. D. Geers. Computational homogenization for heat conduction in heterogeneous solids. *International Journal for Numerical Methods in Engineering*, 73(2):185–204, jan 2008. ISSN 00295981. doi: 10.1002/nme.2068.
- [79] R. R. Rama, S. Skatulla, and C. Sansour. Real-time modelling of diastolic filling of the heart using the Proper Orthogonal Decomposition with Interpolation. *International Journal of Solids and Structures*, 0:1–14, 2016. ISSN 0020-7683. doi: 10.1016/j.ijsolstr.2016.04.003.
- [80] F. J. Reis and F. M. Andrade Pires. An adaptive sub-incremental strategy for the solution of homogenization-based multi-scale problems. *Computer Methods in Applied Mechanics and Engineering*, 257:164–182, apr 2013. ISSN 00457825. doi: 10.1016/j.cma.2013.01.003.

- [81] F. J. P. Reis and F. M. Andrade Pires. A mortar based approach for the enforcement of periodic boundary conditions on arbitrarily generated meshes. *Computer Methods in Applied Mechanics and Engineering*, 274(June 2014):168–191, jun 2014. ISSN 00457825. doi: 10.1016/j.cma.2014.01.029.
- [82] E. Rohan. Sensitivity strategies in modelling heterogeneous media undergoing finite deformation. *Mathematics and Computers in Simulation*, 61(3-6):261–270, 2003. ISSN 03784754. doi: 10.1016/S0378-4754(02)00082-4.
- [83] P. Romero and E. Masad. Relationship between the representative volume element and mechanical properties of asphalt concrete. *J. Mater. Civ. Eng.*, 2001. ISSN 0899-1561. doi: 10.1061/(ASCE)0899-1561(2001)13:1(77).
- [84] K. Sab. On the homogenization and the simulation of random materials. *Eur. J. Mech. A. Solids*, 1992. ISSN 09977538.
- [85] I. Saiki, K. Terada, K. Ikeda, and M. Hori. Appropriate number of unit cells in a representative volume element for micro-structural bifurcation encountered in a multi-scale modeling. *Computer Methods in Applied Mechanics and Engineering*, 191(23-24): 2561–2585, 2002. ISSN 00457825. doi: 10.1016/S0045-7825(01)00413-3.
- [86] P. J. Sánchez, P. J. Blanco, A. E. Huespe, and R. A. Feijóo. Failure-Oriented Multi-scale Variational Formulation: Micro-structures with nucleation and evolution of softening bands. *Computer Methods in Applied Mechanics and Engineering*, 257:221–247, 2013. ISSN 00457825. doi: 10.1016/j.cma.2012.11.016.
- [87] E. Sanchez-palencia. *Non-Homogeneous Media and Vibration Theory*, volume 127 of *Lecture Notes in Physics*. Springer Berlin Heidelberg, Berlin, Heidelberg, 1980. ISBN 978-3-540-10000-3. doi: 10.1007/3-540-10000-8.
- [88] L. Scheunemann, D. Balzani, D. Brands, and J. Schröder. Design of 3D statistically similar Representative Volume Elements based on Minkowski functionals. *Mechanics of Materials*, m, 2015. ISSN 01676636. doi: 10.1016/j.mechmat.2015.03.005.
- [89] J. Schröder. Derivation of the localization and homogenization conditions for electro-mechanically coupled problems. *Computational Materials Science*, 46(3):595–599, 2009. ISSN 09270256. doi: 10.1016/j.commatsci.2009.03.035.
- [90] J. Schröder. A numerical two-scale homogenization scheme: the FE2-method. In J. Schröder and K. Hackl, editors, *Plasticity and Beyond*, volume 550, pages 1–64. Springer Vienna, 2014. ISBN 978-3-7091-1624-1. doi: 10.1007/978-3-7091-1625-8\_1.
- [91] J. Schröder and M. A. Keip. Two-scale homogenization of electromechanically coupled boundary value problems: Consistent linearization and applications. *Computational Mechanics*, 50(2):229–244, 2012. ISSN 01787675. doi: 10.1007/s00466-012-0715-9.
- [92] J. Schröder, D. Balzani, and D. Brands. Approximation of random microstructures by periodic statistically similar representative volume elements based on lineal-path functions. *Archive of Applied Mechanics*, 81(7):975–997, 2011. ISSN 09391533. doi: 10.1007/s00419-010-0462-3.



- [93] O. V. D. Sluis, P. H. Vosbeek, P. J. Schreurs, and H. E. Jer. Homogenization of heterogeneous polymers. *International Journal of Solids and Structures*, 36(21):3193–3214, 1999. ISSN 00207683. doi: 10.1016/S0020-7683(98)00144-9.
- [94] R. J. Smit, W. A. Brekelmans, and H. E. Meijer. Prediction of the large-strain mechanical response of heterogeneous polymer systems: Local and global deformation behaviour of a representative volume element of voided polycarbonate. *Journal of the Mechanics and Physics of Solids*, 47(2):201–221, 1999. ISSN 00225096. doi: 10.1016/S0022-5096(98)00089-1.
- [95] R. J. M. Smit, W. Brekelmans, and H. E. H. Meijer. Prediction of the mechanical behavior of nonlinear heterogeneous systems by multi-level finite element modeling. *Computer Methods in Applied Mechanics and Engineering*, 155(97):181–192, 1998. ISSN 00457825. doi: 10.1016/S0045-7825(97)00139-4.
- [96] G. H. Staab. *Laminar Composites*. Elsevier, 2 edition, jan 2015. ISBN 978-0-12-802400-3. doi: 10.1016/C2014-0-02568-3.
- [97] P. Suquet. Elements of homogenization for inelastic solid mechanics. 01 1985.
- [98] P. M. Suquet. Local and global aspects in the mathematical theory of plasticity. *Plast. Today*, pages 279–310, 1985.
- [99] N. Takano, M. Zako, and Y. Ohnishi. Macro-micro uncoupled homogenization procedure for microscopic nonlinear behavior analysis of composites. *Materials Science Research International*, 2(2):81–86, 1996. ISSN 13411683.
- [100] N. Takano, Y. Ohnishi, M. Zako, and K. Nishiyabu. Microstructure-based deep-drawing simulation of knitted fabric reinforced thermoplastic by homogenization theory. *International Journal of Solids and Structures*, 38(36-37):6333–6356, 2001. ISSN 00207683. doi: 10.1016/S0020-7683(00)00418-2.
- [101] I. Temizer and P. Wriggers. An adaptive method for homogenization in orthotropic nonlinear elasticity. *Computer Methods in Applied Mechanics and Engineering*, 196(35-36):3409–3423, 2007. ISSN 00457825. doi: 10.1016/j.cma.2007.03.017.
- [102] I. Temizer and P. Wriggers. On the computation of the macroscopic tangent for multiscale volumetric homogenization problems. *Computer Methods in Applied Mechanics and Engineering*, 198(3-4):495–510, dec 2008. ISSN 00457825. doi: 10.1016/j.cma.2008.08.018.
- [103] I. Temizer and P. Wriggers. An adaptive multiscale resolution strategy for the finite deformation analysis of microheterogeneous structures. *Computer Methods in Applied Mechanics and Engineering*, 200(37-40):2639–2661, 2011. ISSN 00457825. doi: 10.1016/j.cma.2010.06.013.
- [104] I. Temizer and T. I. Zohdi. A numerical method for homogenization in non-linear elasticity. *Computational Mechanics*, 40(2):281–298, 2007. ISSN 01787675. doi: 10.1007/s00466-006-0097-y.

- [105] K. Terada and N. Kikuchi. Nonlinear homogenization method for practical applications. *Computational Methods in Micromechanics*, 62(617):1–16, 1995. ISSN 01608835.
- [106] K. Terada and N. Kikuchi. A class of general algorithms for multi-scale analyses of heterogeneous media. *Computer Methods in Applied Mechanics and Engineering*, 190(40-41):5427–5464, 2001. ISSN 00457825. doi: 10.1016/S0045-7825(01)00179-7.
- [107] K. Terada, M. Hori, T. Kyoya, and N. Kikuchi. Simulation of the multi-scale convergence in computational homogenization approaches. *International Journal of Solids and Structures*, 37(16):2285–2311, 2000. ISSN 00207683. doi: 10.1016/S0020-7683(98)00341-2.
- [108] S. Toro, P. J. Sánchez, P. J. Blanco, E. A. De Souza Neto, A. E. Huespe, and R. A. Feijóo. Multiscale formulation for material failure accounting for cohesive cracks at the macro and micro scales. *Int. J. Plast.*, 76:75–110, 2016. ISSN 07496419. doi: 10.1016/j.ijplas.2015.07.001.
- [109] A. B. Tran, J. Yvonnet, Q.-C. He, C. Toulemonde, and J. Sanahuja. A simple computational homogenization method for structures made of heterogeneous linear viscoelastic materials. *Computer Methods in Applied Mechanics and Engineering*, 200(45-46):2956–2970, 2011.
- [110] O. van der Sluis, P. J. Schreurs, and H. E. Meijer. Effective properties of a viscoplastic constitutive model obtained by homogenization. *Mech. Mater.*, 31(11):743–759, 1999. ISSN 01676636. doi: 10.1016/S0167-6636(99)00028-9.
- [111] O. Van Der Sluis, P. J. G. Schreurs, W. A. M. Brekelmans, and H. E. H. Meijer. Overall behaviour of heterogeneous elastoviscoplastic materials: Effect of microstructural modelling. *Mechanics of Materials*, 32(8):449–462, 2000. ISSN 01676636. doi: 10.1016/S0167-6636(00)00019-3.
- [112] K. Váradi, Z. Néder, and K. Friedrich. FE contact and thermal analysis of composite surfaces with different fibre orientations subjected to a sliding steel asperity. *Finite Elements In Analysis And Design Journal*, 40(11):1475–1497, jul 2004. ISSN 0168874X. doi: 10.1016/j.finel.2003.09.002.
- [113] P. Vosbeek. *A micromechanical approach to deformation and failure of discrete media*. PhD thesis, Eindhoven University of Technology, 1994.
- [114] J. R. Willis. Bounds and self-consistent estimates for the overall properties of nonlinear composites. *Journal of the Mechanics and Physics of Solids*, 25(3):185–202, 1977. ISSN 02724960. doi: 10.1093/imamat/39.3.215.
- [115] I. Yassine and T. McGraw. 4th order diffusion tensor interpolation with divergence and curl constrained b?? zier patches. In *Proc. - 2009 IEEE Int. Symp. Biomed. Imaging From Nano to Macro, ISBI 2009*, volume 1, pages 634–637, 2009. ISBN 9781424439324. doi: 10.1109/ISBI.2009.5193127.
- [116] J. Yvonnet and Q. C. He. The reduced model multiscale method (R3M) for the non-linear homogenization of hyperelastic media at finite strains. *Journal of Computational Physics*, 223(1):341–368, 2007. ISSN 00219991. doi: 10.1016/j.jcp.2006.09.019.

- [117] J. Yvonnet, D. Gonzalez, and Q. C. He. Numerically explicit potentials for the homogenization of nonlinear elastic heterogeneous materials. *Computer Methods in Applied Mechanics and Engineering*, 198(33-36):2723–2737, 2009. ISSN 00457825. doi: 10.1016/j.cma.2009.03.017.
- [118] J. Yvonnet, E. Monteiro, and Q. C. He. Computational homogenization method and reduced database model for hyperelastic heterogeneous structures. *International Journal for Multiscale Computational Engineering*, 11(3):201–225, 2013. ISSN 15431649. doi: 10.1615/IntJMultCompEng.2013005374.
- [119] J. Zhao, H. Li, G. Cheng, and Y. Cai. On predicting the effective elastic properties of polymer nanocomposites by novel numerical implementation of asymptotic homogenization method. *Composite Structures*, 135:297–305, 2016. ISSN 02638223. doi: 10.1016/j.compstruct.2015.09.039.